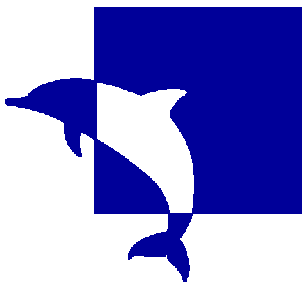

University of Southampton

A thesis entitled

Characterization and fabrication of nanoporous materials by template directed sol-gel methods

By

Steven Michael Hant

In candidature for the degree of

Doctor of Philosophy

As a result of work undertaken in the school of chemistry

2002-2006

Abstract

Characterization and fabrication of nanoporous materials by template directed sol-gel methods

By Steven Hant

This research project focussed on developing synthetic strategies to fabricate a variety of nanoporous materials ranging the full range of pore sizes from micro to macro using template assisted sol-gel routes. Both colloidal crystals and surfactant self assemblies were employed as templates.

Initial studies focussed on the fabrication of macroporous titano/alumino and tinsilicate materials by dip infiltrating colloidal crystal templates with sol-gel mixtures. The sols were prehydrolysed in order to ensure atomic scale homogeneity of the final material. These materials were subsequently characterised using SEM to observe the macrostructure whilst XRD, EDX, NMR and iR were used to characterise the thermal stability and chemical homogeneity. The work reports materials with metal:silicon atomic ratios for macroporous titanosilicates and aluminosilicates that are far in excess of those previously reported in the literature.

Following this research was focused on the production of hierarchically ordered meso/macro silica materials by dip coating a preformed colloidal crystal into a sol-gel solution which contained surfactants. This technique combines principles of colloidal crystal templating and liquid crystal templating and by varying the surfactant it was possible to obtain mesoporous pore walls with both ordered and wormhole pore morphologies. The materials were characterised with both SEM, TEM and Nitrogen sorption and exhibited surface areas in excess of 500 m^2 g^{-1}. It was further shown that the mesopore size could be tuned by choosing different surfactants and mesopore sizes ranging from 2-7 nm were produced.

Finally, the synthetic procedures developed to produce meso/macro silica were used to produce meso/macro titania and zirconia by extending the method to incorporate different metal alkoxides precursors. These materials were once again characterised by

SEM, TEM and nitrogen sorption and it was shown meso/macro titania and zirconia could be easily fabricated using this simple approach. It was also shown that the ordering in these materials was more sensitive to the chosen surfactant with only larger tri-block copolymer surfactants yielding stable mesostructures.

Contents page

Acknowledgements

I would like to thank first and foremost Professor George Attard and Dr Kevin Ryan for the many hours spent in scientific discussions, guidance regarding the direction of the work undertaken and for encouragement throughout the PhD.

I would also like to thank Matthew Cheetham, Marcus Diamond, Douglas Offin, Nefeli Tsaloglue, Jason Beard, Chris Vian, Ken Ryman for help with various aspects of my work and also for the good time.

Finally, I want to thank Suz.

Chapter 1

Contents page

INTRODUCTION TO NANOPOROUS MATERIALS

CHAPTER 1 – INTRODUCTION TO NANOPOROUS MATERIALS

Ordered nanoporous materials have been the subject of a great deal of attention within the scientific community for many years now[1-4]. As chemically functional materials their applications are vast and varied ranging from catalyst to optical waveguide.

Conventionally nanoporous materials break down into three broad categories depending upon the materials pore diameter. The size ranges were prescribed by IUPAC[5] and serve as a good guideline with which to subcategorise the various porous materials.

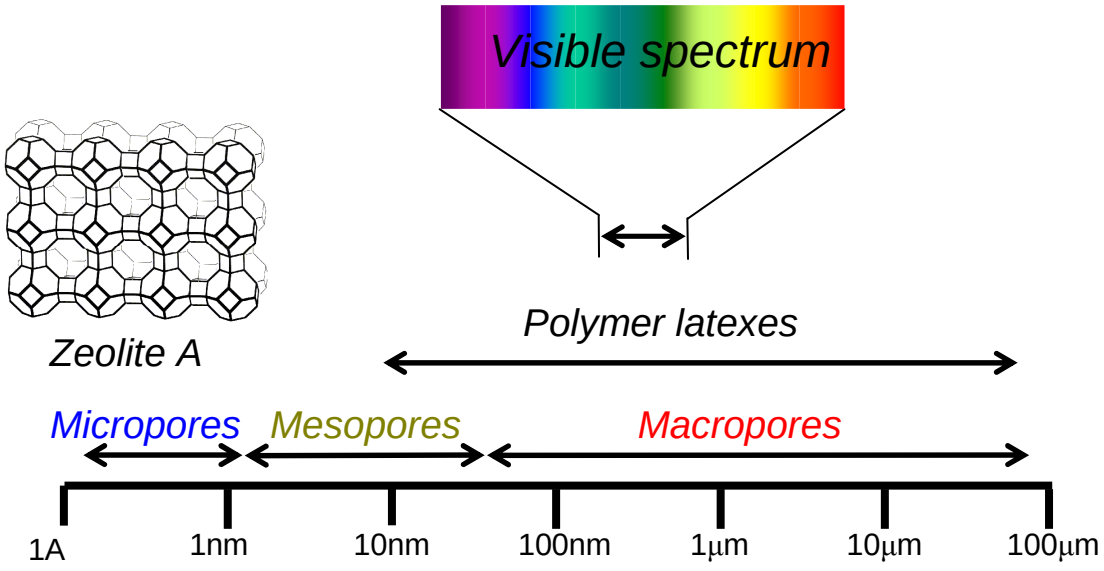

Figure 1.1: Representation of the size scales used to classify nanoporous materials.

At the far end of the spectrum are microporous materials characterised by pore sizes smaller than 2 nm. A large subclass of microporous materials are the zeolites which are aluminosilicates consisting of periodic three dimensional framework structures containing voids.

The second category is the mesoporous materials as categorized by pore sizes within the range 2 – 50 nm. These materials are commonly prepared by surfactant or liquid crystal templating and have shown great potential not only in catalytic applications but also for battery, sensor and fuel cell technologies.

Finally at the top end, materials with pore diameters that are greater than 50 nm are classified as macroporous materials. These materials are usually fabricated by colloidal crystal templating or lithography and have shown potential as possible optical storage media on account of the periodicity of the material being within the size range of visible light.

In the context of this thesis, the term 'nanoporous' is used for materials with pore sizes up to several hundred nanometers in diameter. What follows is a review of nanoporous materials, focusing mainly on meso and macroporous materials, microporous materials are also mentioned briefly for completion

1.1 Microporous materials

Microporous materials are a very important class of compounds that have an annual worldwide usage of around 1.6 Mton per year. Research in this area of materials science is growing rapidly with many new materials, modifications, properties and applications being discovered and developed[6-8].

Microporous solids are crystalline materials that contain internal connected cages/cavities or channels with pores of molecular dimensions, typically 2.5 - 20 Å. The interconnected cages form one-, two- or three-dimensional pore systems within the material and these materials typically have a very large surface area (typically > 300 $m^2 g^{-1}$) and void volume (> 0.1 $cm^3 g^{-1}$). The size and uniformity of the micropores enables them to separate different materials by their respective geometries and because of this property microporous materials are often utilised as molecular sieves. Furthermore, on account of the large surface area, microporous materials are particularly useful in the field of catalysis and ion exchange.

The largest and most important subclass of microporous materials are zeolites. Zeolites are microporous aluminosilicates and occur extensively as natural minerals. The microporous framework of zeolites is composed of edge sharing SiO_4 and AlO_4 tetrahedra; related compounds (e.g. aluminophosphates) possess similar structures but differ in the chemical composition of the framework.

1.1.1 Synthesis

Microporous materials are typically synthesised under solvothermal conditions using temperatures between 100 – 250 °C, autogenous pressures (30 – 910 bar)[9, 10] and either strongly basic conditions (for zeolites) or weakly acidic or neutral conditions (for metal phosphates or derivatives). The solvothermal technique is extremely versatile on account of the effective solvating ability of the solvent under these conditions which allows the dissolution and mixing of all the starting materials to form a homogenous gel in the initial stages of the reaction. The reaction proceeds by the formation of nucleation centres which subsequently grow to form the final product. A typical starting mixture is composed of:

- **Sources of framework atoms** – These are generally introduced in the reaction mixture as oxides, hydroxides or alkoxides e.g. fumed silica, alumina sols etc.
- **The solvent** - Water is usually used as a solvent to dissolve the mixture or gel of framework elements.
- **Sources of mineraliser** - Fluoride or hydroxide ions are used in the dissolution of the starting gel and are recovered on crystallisation of the product. Careful control of the pH and fluoride ion concentration can determine the stoichiometry of the final microporous material.
- **Sources of inorganic cations and organic species** - Inorganic cations are added as hydroxides (e.g. LiOH, NaOH, KOH) or salts (e.g. NaCl, $CaCl_2$, $BaCl_2$). Organic species include quaternary ammonium ions.

There are numerous variables in the reaction each of which can be altered to create different products. Reaction variables include: time, temperature, starting materials, pH, pressure, the presence of any mineralising agent and so on. Whilst this lends versatility to the process it is also potentially problematic when attempting to design a material with specific properties, as the large number of variables leads to a large parameter space, and finding the region in this space that gives the desired properties can be very time consuming. However the subject is sufficiently mature that there are several guidelines for the effect certain variables have on solvothermal syntheses. For example raising the temperature of synthesis tends to lead to species with a lower intercrystalline void space and lower water content[10].

One of the most significant structure-directing influences on zeolite synthesis is the effect of alkali metal ions on the final material. In the synthesis of zeolite A, sodium cations are added to the starting gel in the form of sodium hydroxide. In 1961 Barrer and Denny used tetramethylammonium (TMA) hydroxide in place of sodium hydroxide in the synthesis of zeolite A[11]. It was found that using a TMA cation reduced the percentage of aluminium in the framework. This was explained in terms of the requirement for fewer cations in the void spaces to balance the negatively charged aluminium in the framework; the TMA cation being much larger than the sodium cation.

Recently there has been considerable interest in the use of cationic or uncharged organic additives in the synthesis of novel zeolites. The functions of these so-called organic templates during zeolite synthesis are not well understood. In a review in 1992 Davis and

Lobo[4] suggested that organic species could adopt any of three roles in zeolite synthesis, these roles being: space-filling agents, structure directing agents, or templates.
Space filling refers to a situation in which the role of the organic is simply to exclude water from the voids in the zeolite framework. If on the other hand the organic is used as a template the resulting product will reflect the initial templates geometrical structure and as such each unique template will result in a unique product. Finally structure direction describes a more subtle effect where the presence of a particular organic moiety leads to the preference for the synthesis of a particular structure.

One of the best examples of organic templating is the use of a triquaternary ammonium species in the synthesis of ZSM-18 (MEI). The structure consists of a one-dimensional 12-ring channel in which the large organic species fits exactly (figure 1.2).

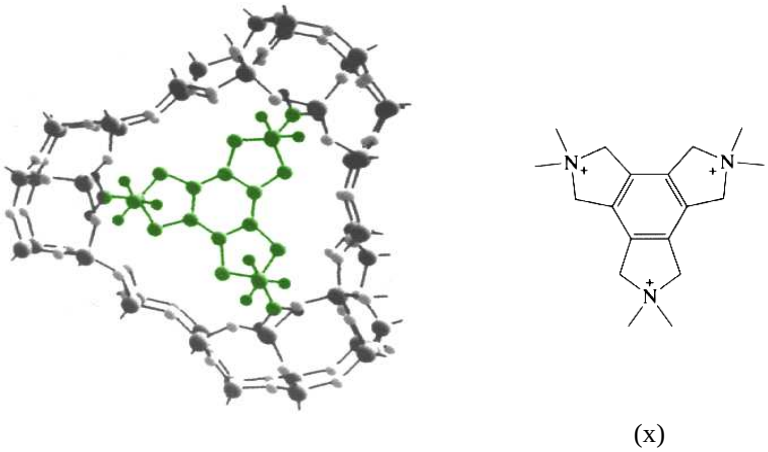

(x)

Figure 1.2: Molecular simulation of the position of the triquaternary ammonium species (x) in the void space of ZSM-18[4].

1.1.2 Applications

The main applications of microporous materials fall into three categories, namely ion-exchange, separation and catalysis. Zeolites are the class of microporous material that are almost exclusively used for these applications and the importance of zeolites in commercial applications is evidenced by the fact that the annual production of synthetic zeolites has reached approximately 1.3 Mton. Further details of these three applications is given below:

a. Ion-exchange

Ion exchange as the name suggests is the process by which the hydrated extra framework cations in the microporous material are replaced by other type's of cations present in the solution in which the microporous material is immersed[12]. One of the most common ion-exchange applications is water-softening whereby Ca^{2+} and Mg^{2+} cations are replaced with a different ion (usually Na^{+}). Sodium coated zeolites are most commonly used for this application and after softening a large quantity of water the sodium ions adsorbed on the zeolites are depleted and as such the zeolite requires replenishing, which is achieved by passing a highly concentrated solution of sodium ions (brine) over the zeolite.

b. Separation

The molecular dimensions of voids in zeolite materials result in the potential for chemical separation. A major industrial use of zeolite molecular sieves is in the separation of straight chain from branched hydrocarbons and aromatics[13]. Subtle control over the pore size can often be achieved by exchanging the cation present for one of a different size. The separation of smaller molecules such as oxygen and nitrogen can also be achieved using lithium exchanged zeolite-X[14]. This separation occurs because the affinity of the under-coordinated Li^{+} cations in the zeolite is greater for N_2 molecules than O_2 molecules. So when air is passed over the zeolites the nitrogen is adsorbed preferentially to the oxygen molecules.

c. Catalysis

The largest area for zeolites in catalysis is in the oil refining and petrochemical industries where zeolites are used for catalytic cracking[15-17]. This application accounts for 95 % of the world's consumption of zeolites for catalysis. The catalyst used in this process is zeolite-y, shown below in figure 1.3. Zeolite-y is used in its acidic form in petroleum refinery catalytic cracking units where the steric constraints of the pores and the well defined acid sites of the zeolite lead to the highly selective cracking of heavy paraffin's into gasoline grade naphtha's.

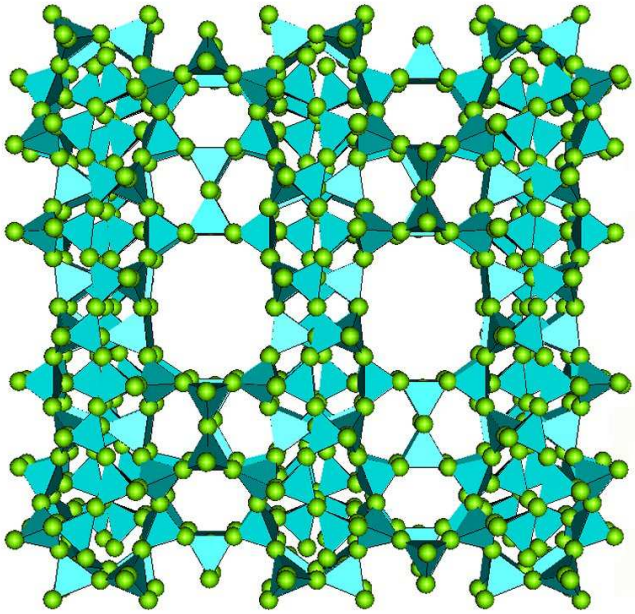

Figure 1.3: Zeolite Y.

1.2 Mesoporous materials

Mesoporous materials are defined by pore sizes within the range of 2 – 50 nm and are a relatively new field of materials. Research on mesoporous materials was originally motivated by the desire for ordered alumina/silica materials with pores larger than those found in zeolitic materials for use in petrochemical catalysis.

The first successful synthesis of mesoporous materials was in 1992 when Beck and co-workers reported a range of mesoporous amorphous silicate materials known as M41S[18, 19]. The M41S family of materials consists of three structure types, each of which has a highly ordered channel systems with narrow pore size distributions (pore diameters > 2 nm).

Figure 1.4a-c shows TEM images highlighting the pore morphologies observed for the M41S family. The first material which is known as MCM-41 (Mobil Corporation Material 41) contains a hexagonal arrangement of channels. Figure 1.4a shows a cross section through this channel system, clearly highlighting the highly ordered hexagonal arrangement of the channels. The second material, MCM-48, has a complex three dimensional channel system (Fig. 1.4b) whilst the third material, MCM-50, consists of stacked silica sheets (Fig. 1.4c).

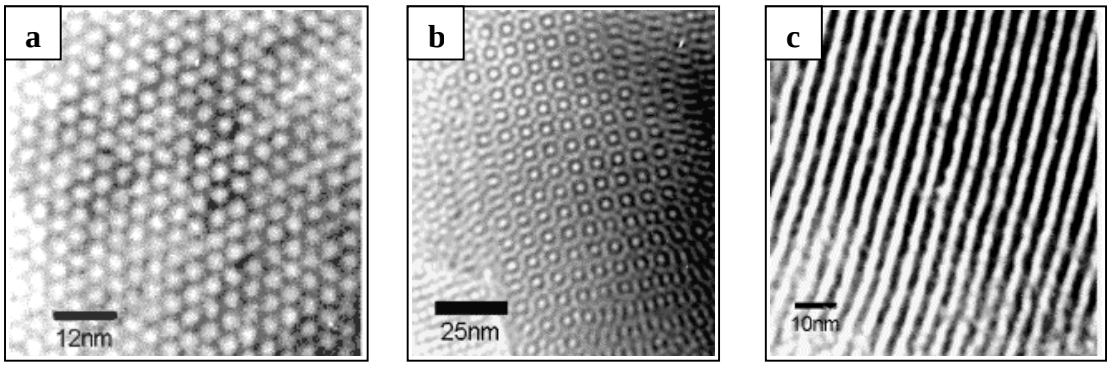

Figure 1.4: TEM images of mesoporous silica's prepared by the Mobil method. a) Hexagonal pore morphology (hexagonal array of cylindrical holes), b) Cubic pore morphology (complex interconnecting channel system with the Ia3d space group), c) Stacked silica sheets[20].

The preparation of these materials centres on using self-assembled surfactant aggregates as structure directing agents and these materials were labelled according to the liquid crystal phase from which they were formed (hexagonal (HI), cubic (V1) and lamellar (Lα)).

The high surface area and tightly controlled pore sizes were among the many desirable properties that made these materials the focus of a great deal of research over the following years. The mobile workers also reported that partial exchange of silica for alumina, in M41S materials, resulted in mesoporous aluminosilicate materials. This initial effort was soon followed by the synthesis of other mixed oxides, such as titanosilicates and borosilicates[21-24], which in turn led to the development of a variety of other non silica inorganic oxides[25-28]. It has also been shown that mesoporous metals can be prepared using similar principles[29-32].

1.2.1 Surfactants and liquid crystal phases

As already stated the materials described above were synthesised using surfactant aggregates as structure directing agents in a sol-gel process. This is known as a liquid crystal templating approach and is the predominant approach for the production of mesoporous materials. In order to better understand how these ordered structures are formed it is necessary to have an understanding of how surfactants behave in aqueous solutions. Figure 1.5 shows a schematic representation of a surfactant molecule. The molecule consists of a water soluble hydrophilic headgroup and a water insoluble hydrophobic tailgroup.

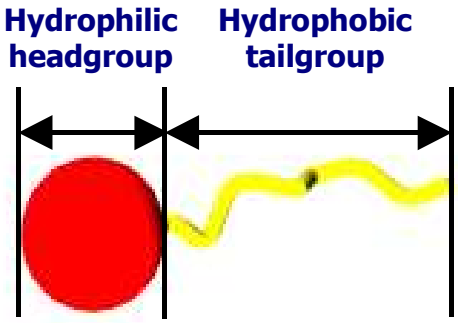

Figure 1.5: Schematic representation of a typical surfactant molecule.

Due to the amphilic nature of surfactant molecules when they are added to water they aggregate together to form micelles (Figure 1.6) with the polar head groups on the outside and the hydrocarbon tails towards the centre. This aggregation only occurs after a certain concentration is reached (called the critical micelle concentration or cmc) which is typically about 1 wt % of surfactant. It is easy to see why micelles are stable structures because the hydrophobic components of the molecules are shielded from the water by the hydrophilic headgroups.

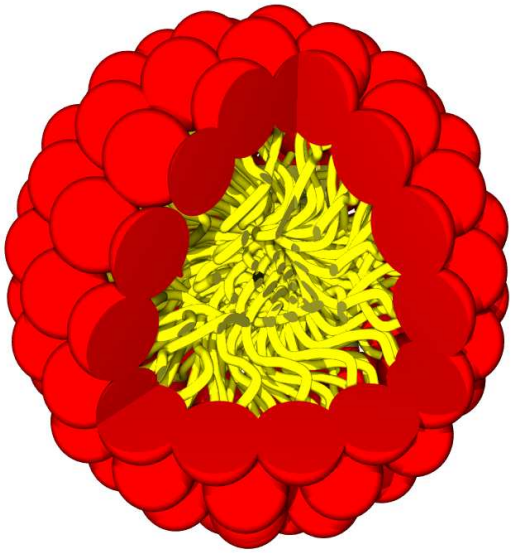

Figure 1.6: Schematic representation of a spherical micelle.

Further increases in the surfactant concentration result in the formation of more micelles, until eventually a point is reached when the micelles reorganise to form larger structures (Figure 1.7). One such structure is the hexagonal phase which consists of a hexagonal arrangement of micellar rods. Once again this structure forms so that the hydrophillic headgroups are in contact with the water whilst the hydrophobic tailgroups are tucked away inside the columns. Another common structure is known as the lamellar structure. This forms at even higher concentrations than the hexagonal structure and consists of bilayers separated from each other by water. At the extremes where the surfactant concentration is very high inverse phases are formed such as the inverse hexagonal and inverse micellar phase. As with the micellar phase the inverse micellar also consists of spherical micelles however in this case we have the hydrophobic tailgroups projected outwards whilst the hydrophilic headgroups surround small pockets of water.

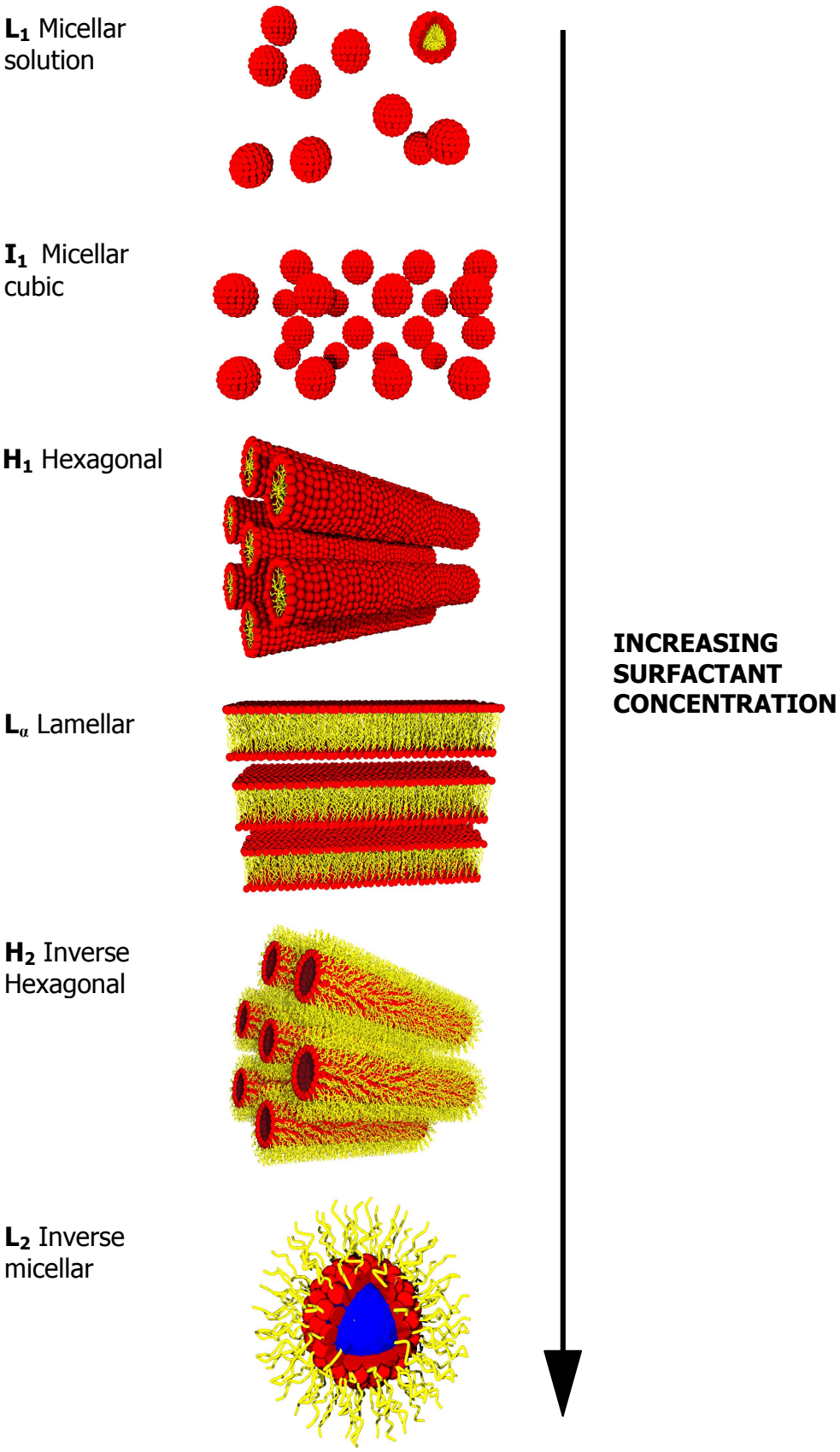

Figure 1.7: Examples of surfactant aggregate structures formed in lyotropic systems.

Amphilic molecules can form a diverse range of mesostructures and those shown in figure 1.7 represent only a small number of the possibilities.

The larger structures, formed beyond the concentrations of surfactant required for micelles, are said to be liquid crystalline. This is because the molecules are oriented on average along some preferred direction, producing fluid but structurally anisotropic phases. The molecules in a liquid crystal phase do not have the positional and orientational order of a solid nor do they have the total disorder associated with a liquid but tend to lie somewhere between the two extremes. The liquid crystal phases formed by mixtures of surfactant and water are termed lyotropic phases. As with thermotropic liquid crystals altering the temperature can alter the phase. However, in lyotropic systems, altering the water content can also change the structure of the phase.

a. Phase diagrams:

The specific phase that is formed in a surfactant/water system is dependant on both the concentration of surfactant and the temperature. These variables are commonly used to plot binary phase diagrams for amphiphilic molecules. Phase diagrams are constructed, from observations made by polarised light microscopy, X-ray diffraction and NMR.

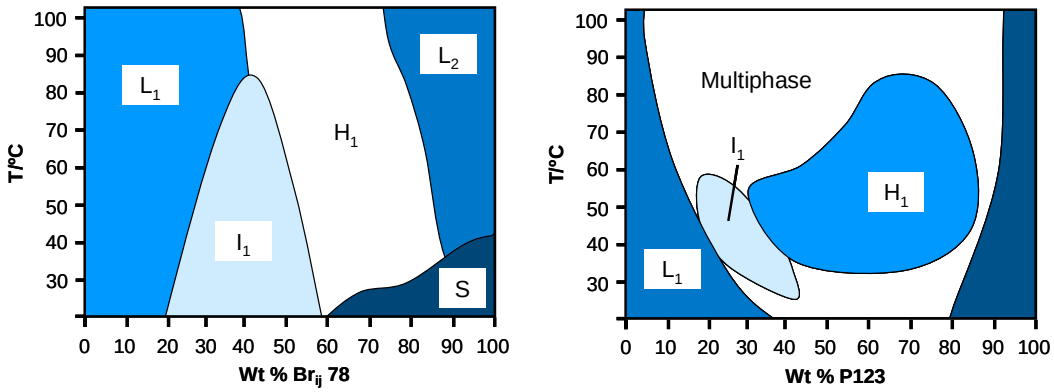

L_1 – Micellar solution

H_1 – Hexagonal phase

L_2 – Inverse micellar solution

I_1 – Micellar cubic phase

S – Solid

Figure 1.8: Liquid crystal phase diagrams for two surfactants in water, a) Br_{ij} 78[77] and b) P123[33].

The phase diagrams for both Brij 78 and P123 are shown above and it is clear that the liquid crystalline behaviour of both of these materials is diverse, with large regions over which the H_I and I_1 phases are stable (figure 1.8). It is also apparent that phase behaviour in lyotropic systems is not purely a function of composition-temperature space but is also strongly influenced by the molecular structure of the surfactant. A complete analysis of how phase behaviour is affected by molecular structure is a complex subject. However, at a basic level, headgroup interactions, tail interactions and interfacial forces determine the shapes of aggregate structures (figure 1.9)

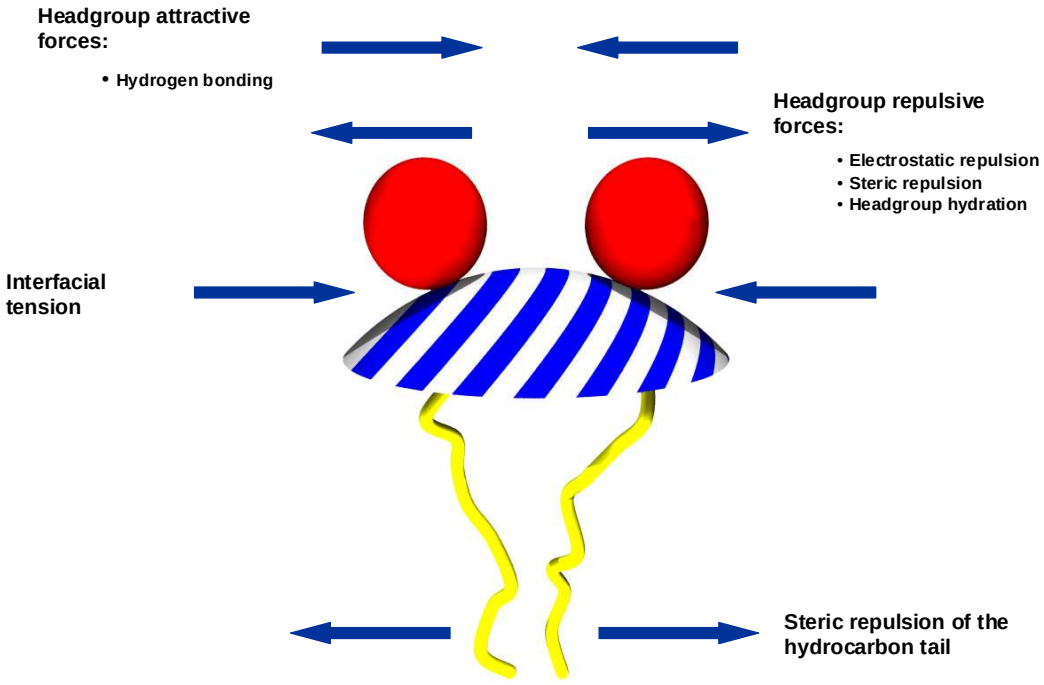

Figure 1.9: Interactions between surfactant molecules in aqueous systems

For ionic surfactants electrostatic repulsion between the charged ionic headgroups usually dominates causing structures with a high positive mean curvature, where the headgroups are well spaced in comparison to the hydrocarbon tails, to be favoured.
If however the balance between the headgroup and tail interactions is more delicate then steric factors become more important in determining the phase behaviour. For example by increasing the size of the headgroup, steric repulsion's between headgroups increases and the space required by the headgroup increases relative to the hydrocarbon tail. This would result in a preference for more curved structures such as spherical micelles. Similarly decreasing the length of the hydrocarbon tail has a similar effect on the phase behaviour. In contrast surfactants with smaller headgroups tend to prefer structures with lower mean curvature such as the lamellar phase (L_α).

1.2.2 Mechanisms of self-assembly

The similarities between liquid crystal mesophases and the M41S family of materials led researchers at Mobil to suggest a liquid crystal templating (LCT) mechanism of formation. This suggests that the structure of the channel system in these mesoporous materials is determined by the surfactant aggregation behaviour. The Mobil researchers suggested two alternative mechanisms by which the surfactants might self-assemble into the appropriate mesophases. These two mechanisms are discussed below along with the evaporation induced self assembly mechanism which has been extensively used to fabricate mesoporous films.

a. Direct Liquid crystal templating:

The first mechanism postulated that there was a hexagonally ordered surfactant phase already formed prior to the addition of silicate source. Upon addition of this silica source the anions diffuse into the water regions of the mesophase, subsequent condensation in the interstitial voids results in the mesostructured silica.

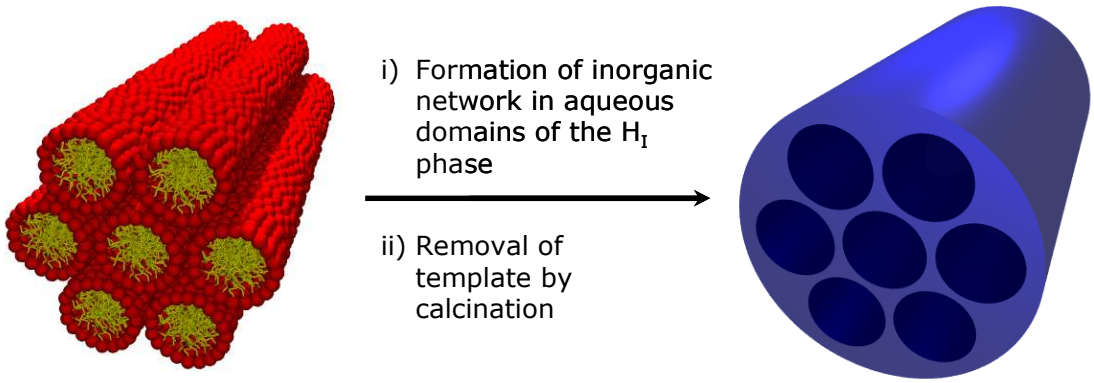

Figure 1.10: Schematic representation of the direct liquid crystal templating approach.

This mechanistic pathway received little support in the literature because it was noted that the Mobil method utilised surfactant concentrations of between 1-10 wt % which is far lower that required to form surfactant mesophases[34] (typically greater than 20 wt %, see figure 1.8). Further research suggested that, provided the concentration of surfactant was greater than the CMC, MCM-41 could be successfully synthesised, which further suggests problems with the direct liquid crystal model.

Direct liquid crystal templating of mesoporous materials was demonstrated in 1995 by the use of high surfactant concentrations[20]. The characteristic phase of the surfactant-water system can be used as a direct mould for the forming oxide, ceramic or metal.

The preparation of a mesoporous silica directly from a liquid crystal phase involves addition of a silicon alkoxide (typically TEOS or TMOS) to a surfactant (> 50 wt%), water and acid mixture. Initially, a large amount of methanol is produced which destroys the liquid crystal phase, but removing the methanol under a gentle vacuum can regenerate the phase. After leaving the mixture to gel, the surfactant is removed by calcination. The aqueous domains of the surfactant phases determine the regions in which condensation of the silica network occurs. Consequently, the structure of the calcined silica is a cast of the supramolecular architecture of the liquid crystal phase.

b. Co-operative self-assembly

The second mechanism proposed by the Mobil researchers suggested that the addition of silica resulted in the ordering of silicate encased surfactant micelles. In this case prior to the addition of silica micelles are present in solution but no hexagonal phase is observed. Upon addition of the silica source to the system silicate anions coat the surface of the micellar rods. These silica encased micelles then self-assemble themselves before condensation of the silicate occurs resulting in the observed mesostructured silica (Figure 1.11).

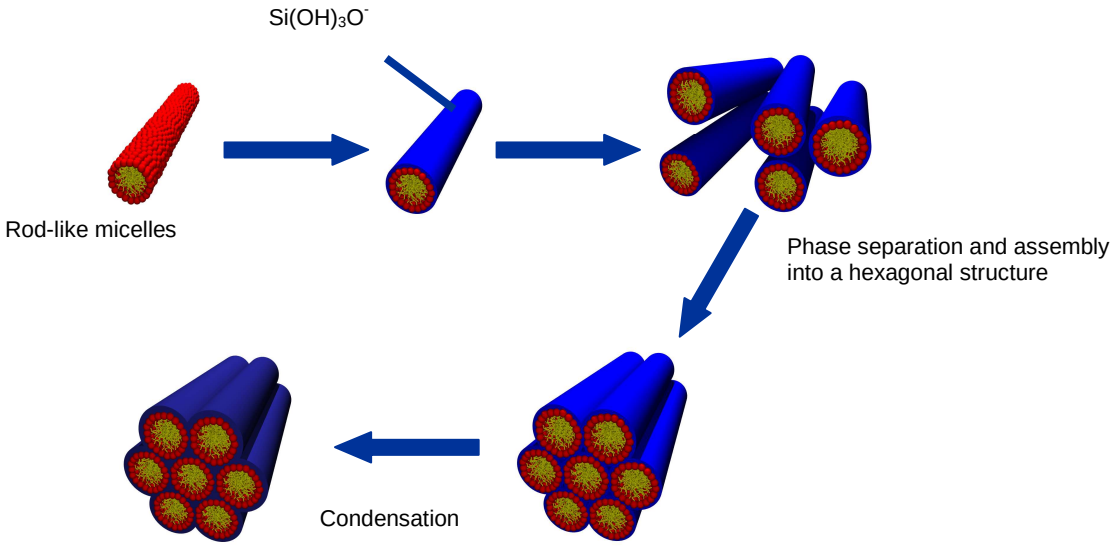

Figure 1.11: Schematic representation of the cooperative self assembly mechanism.

It has been well established that no preformed liquid crystal phase is required for the formation of MCM-41 however there is still some debate over the precise details with various models being suggested[35-39]. All these models share one fundamental principle however, which is that silicate species promotes the formation of a liquid crystal phase at low surfactant concentrations. This observation is consistent with the effect of polyvalent ionic species on the phase behaviour of ionic surfactant solutions. In particular, addition of salt to micellar solutions of cationic surfactants leads to the so-called L_1+w two-phase system. This consists of macroscopic aggregates of micelles dispersed in water. Structural transitions in the micelle-rich regions, driven by the incipient polyvalent inorganic network lead to micron-sized domains of liquid crystalline phases.

c. Evaporation induced self assembly (EISA)

The methods discussed so far generally result in the production of mesoporous powders; however there are a variety of applications for which a mesoporous thin film would be desirable. If a substrate is coated (coating can be achieved by dip-coating, spin-coating etc) with a homogenous solution of silicon alkoxide, surfactant and water diluted with excess ethanol where the concentration of amphiphile, c_0, is much less that the cmc, preferential evaporation of ethanol will occur. This progressively increases the surfactant concentration driving the self-assembly of the surfactants into micelles and their further organization into liquid crystalline mesophases.

Pre-formed silica-surfactant mesophases then serve to nucleate the liquid crystalline phase. These nucleating sites form at solid liquid and liquid vapour interfaces. The net result of this process is the rapid formation of thin film mesophases which are highly ordered with respect to the substrate surface. This process has been coined evaporation induced self assembly[40] and has been shown to allow tight control over morphology and pore size's for a variety of thin films.

Careful variation of the sol's composition allows different mesophases to be formed as it alters the trajectory of the reaction through compositional phase space. It has also been demonstrated that a variety of surfactants can be employed as structure directing agents allowing the fabrication of a wide range of mesoporous materials.

1.2.3 Applications

a. Catalysis

Mesoporous materials have many properties that make them extremely promising for catalytic applications[41]. The extremely high specific surface areas are conducive to high catalytic activity and the large pore size (relative to microporous zeolites) reduces diffusional restriction of reactants and allows for fixation of larger active complexes or bulky molecules.

Initial catalytic studies on mesoporous materials focused on metal substituted MCM-41 materials. In this case the active species is incorporated into the silica matrix and these materials were mainly tested on oxidation and acid catalysis reactions[23, 42, 43]. The next stage of development involved utilising mesoporous silica's as a host material for anchoring stereo- and enantioselective species.

Although extensive research efforts have been undertaken to explore the catalytic activities of mesoporous materials industrial use has so far been limited. Only a longer time frame will tell if mesoporous materials with narrow pore size distribution may in future reveal commercial applications.

b. Other

Aside from catalysis and separation another application for mesoporous materials is as adsorbents. Both the large pore volume and compositional flexibility of mesoporous materials can be exploited for the selective adsorption of gases and liquids and the binding of metals. Mesoporous materials have been shown to have excellent storage capacities for a variety of gases including methane, nitrogen and argon and have also been used commercially for a volatile organic compound (VOC) recovery process where the high surface area of a mesoporous aluminosilicate was utilized to adsorb various VOC's at room temperature. The saturated sorbent can then be reactivated with hot air at 120-150 °C.

Other applications that have been suggested for mesoporous materials include as novel electrode materials [29, 44-46] and as sensors [47-50].

1.3 Macroporous materials

The largest pore diameter that can be achieved through liquid crystal templating is about 30 nm, and it wasn't until 1997 that a successful preparative method for ordered porous materials with larger pore sizes was first reported[51]. The technique involved utilising colloidal crystals, consisting of close packed arrays of polymer or silica microspheres[52], with sub micron to micron size diameters, as templates and opened up a simple method with which to produce ordered macroporous materials. Materials fabricated by the colloidal crystal templating method consist of a large 3D array of close packed 'air spheres'. They are sometimes termed inverse opals on account of the similarity the colloidal crystal template bares to that of the opal structure. The process has received a large amount of attention[53] on account of the wealth of potential applications for this new class of nanoporous material, ranging from such diverse applications as optical waveguide, catalysis or special effect pigments.

1.3.1 Colloidal crystal templating

The general concept of colloidal crystal templating is simple and involves three steps. Initially a close packed array of ordered monodisperse spheres is assembled (Figure 1.12a), secondly the interstitial voids of the colloidal crystal are infiltrated with a suitable chemical precursor (b) which solidifies prior to template removal via either by calcination or dissolution of the template with a suitable solvent (c).

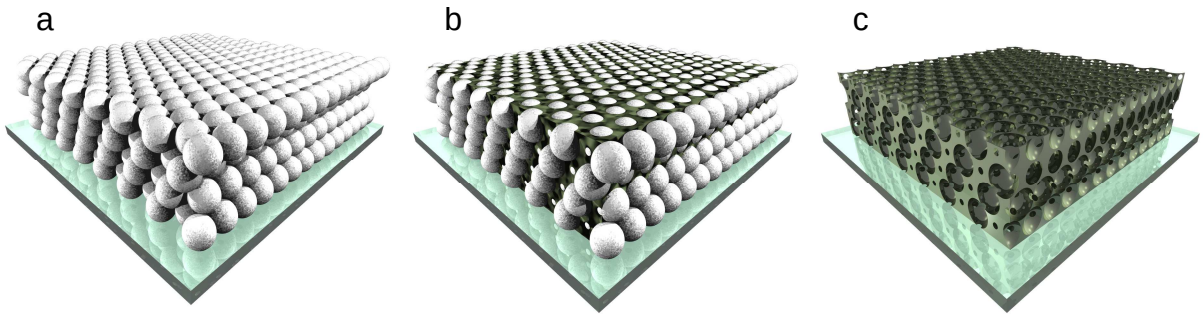

Figure 1.12: The three steps involved in colloidal crystal templating.

a. Assembling the template

The microspheres are usually composed of silica, polystyrene (PS) or polymethyl methacrylate (PMMA) and can be cheaply and easily fabricated with diameters ranging from tens of nanometres up to several microns and with very tight size distributions. Microspheres can also be obtained commercially with a wide range of sizes and functionalities however PS and PMMA spheres are generally favoured in the formation of macroporous materials on account of the ease with which they can be removed after the colloidal crystal architecture has been used as a template.

There are numerous techniques that can be exploited to order the colloidal particles into colloidal crystals, some of which are described below:

- **Sedimentation in a force field** – Sedimentation in a gravitational field seems to be the simplest approach in the formation of 3D crystalline arrays of colloidal spheres. Typically the preparation would involve allowing a suspension of colloidal particles to sediment before either evaporating or removing the solvent to yield an ordered close packed array of spheres (Figure 1.13).

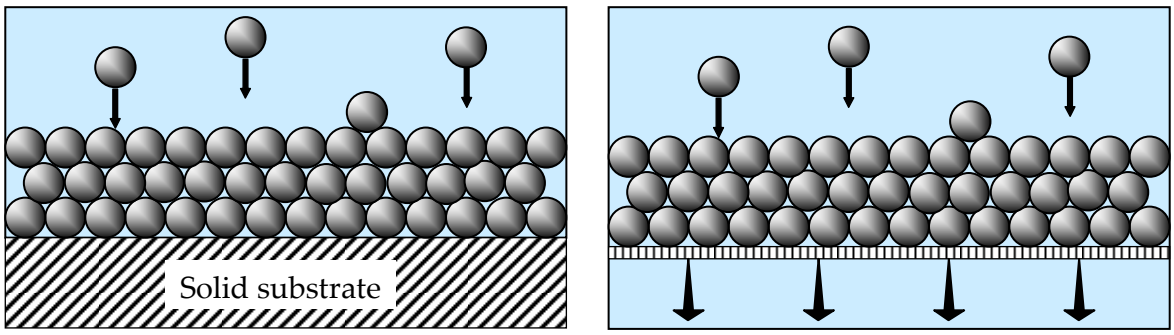

Figure 1.13: Two schematic representations of sedimentation techniques to produce close packed arrays of microspheres.

Despite the apparent simplicity of the approach this method is governed by a host of complex processes such as gravitational settling, Brownian motion and crystallization and for the method to be successful several parameters must be tightly controlled in particular those pertaining to the microspheres such as their density, size and monodispersity. Silica spheres are most commonly employed in this technique on account of the high density of amorphous silica aiding the sedimentation of the spheres. One of the drawbacks of this method is the lack of

control over surface morphology and the number of layers which comprise the crystalline array.

- **Crystallization via repulsive electrostatic interactions** – Under appropriate conditions, highly charged microspheres can spontaneously organise into a variety of crystalline structures. The driving force for this phenomenon is the minimization of electrostatic repulsive interactions.

- **Self-Assembly by physical confinement** – When subjected to physical confinement monodisperse microspheres will often organise themselves into highly ordered 3D structures regardless of their size, bulk properties and surface properties. This method is relatively fast when compared to other techniques and also offers tight control over both the surface morphology and the number of layers of the crystalline assemblies.

b. Methods of infiltration

In order to successfully template around a colloidal crystal it is necessary to find a method with which to fill the voids of a colloidal crystal with material and over the past decade a large number of synthetic strategies have been developed to achieve this. The various methods of infiltrating a colloidal crystal have made the technique extremely versatile in the production of a wide range of macroporous materials and the most common techniques are discussed below;

Sol-gel

One of the foremost techniques to prepare macroporous materials is the sol-gel process (discussed in greater detail in chapter 2, pg 38) where a metal alkoxide dissolved in alcohol is impregnated into the voids of a colloidal crystal. Subsequent hydrolysis and condensation of the metal alkoxide occurs in the voids resulting in the evolution of a metal oxide network. Infiltration of the voids can be allowed to occur naturally by capillary forces or aided by the application of a vacuum.
This is one of the most common techniques used to produce macroporous materials and has been exploited to make macroporous oxides out of a variety of different materials including Si[51, 54], Ti[54-58] and Al[54, 59], and mixed oxides such as Si/Ti [60]. The final

macroporous material is subject to 15-30 % volume shrinkage upon calcination, which is due to the large volume loss during the sol-gel process as the alcohol is evaporated. This shrinkage often results in severe cracking of the final macroporous material. In spite of this, the shrinkage is generally uniform resulting in materials with nearly monodisperse pore sizes.

Salt precipitation and chemical conversion

An alternative method to produce macroporous metal oxides involves the use of metal salt precursors such as acetates and oxalates. In this method a metal salt is deposited into the voids of the colloidal crystal by precipitation from a saturated solution before chemical conversion into a metal oxide[61].

In a typical preparation a colloidal crystal is soaked in a solution of metal salt in alcohol for a few minutes after which it is removed and dried. Evaporation of the solvent leads to precipitation of the metal salt in the voids of the colloidal crystal. Subsequent heat treatment serves to convert the metal salt into its metal oxide and remove the polymer template. This process is also accompanied by shrinkage comparable to that observed for the sol-gel process however it does enable the production of materials that cannot be synthesised by sol-gel routes.

Nanoparticle assembly

Another method with which to prepare ordered macroporous materials involves filling the colloidal crystal voids with nanoparticles. This method offers the significant advantage of being able to incorporate specific nanoparticles of desirable crystal phases directly into the walls of a macroporous material, a further advantage is that as these nanoparticles are already in their final chemical form shrinkage and cracking is kept to a minimum (Typically ca. 5-10 %). There are a number of ways to incorporate nanoparticles into a colloidal crystal, for example a suspension of nanoparticles can infiltrate the colloidal crystal via capillary forces before evaporation of the solvent allows the nanoparticles to settle into the voids of the crystal. In an alternative method the nanoparticles can be introduced prior to ordering of the microspheres, co-operative self assembly of the two components from a mutual suspension followed by evaporation of the solvent leading to the formation of a colloidal crystal with nanoparticles in the voids.

Electrochemical deposition

A variety of macroporous metals, chalcogenides, metal oxides and conducting polymers have all been prepared by an electrochemical templating technique[62-65]. The process involves growing a colloidal crystal onto a conductive substrate prior to immersion in a coating bath where the desired material is electrodeposited around the template. Once again the template is removed by dissolution or calcination to yield the final material. This technique has many advantages over the chemical techniques discussed above in that the process enables almost complete filling of the interstitial voids and as such there is little shrinkage upon template removal. Because of this electrodeposited macroporous materials typically encompass less defects than their chemically prepared counterparts.

Electrochemical deposition enables a greater degree of control over the structural features of the final material such as wall thickness and the degree of filling however the process is limited to production of very small quantities of material and is very difficult to scale up for any bulk scale application.

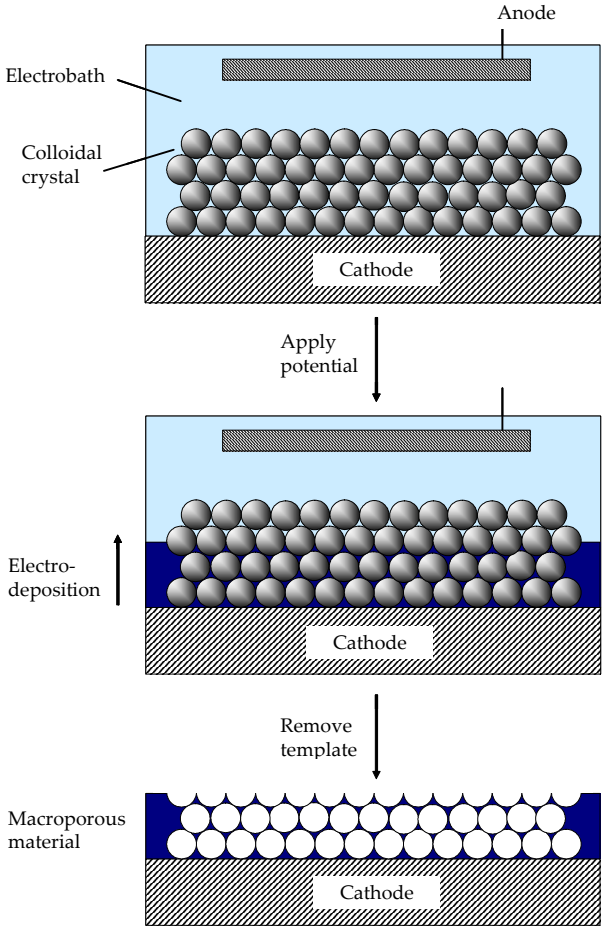

Figure 1.14: Schematic representation of a macroporous material fabricated by electro deposition around a colloidal crystal template.

Organic polymerization

Polymerization of organic precursors around a colloidal crystal array is also a commonly used method for the production of a large variety of macroporous polymers. In this method the colloidal crystals are filled with a liquid monomer which is subsequently polymerized by heat treatment, UV irradiation, and catalysis or even by a chemical oxidation polymerization. Finally extraction is achieved via dissolution. A critical factor in this method is the choice of material for the microspheres as it is essential that the final material will not dissolve in the extracting fluid. Various macroporous polymeric materials have been synthesised in this manner including polyurethane, polystyrene, PMMA and epoxy.

1.3.2 Applications

The study of macroporous materials from colloidal crystal templating is still a very new field of research and applications still need to be demonstrated. Much of the work so far has focussed on advancing the material chemist's tool kit in order to develop reproducible synthetic techniques to obtain macroporous materials with a whole range of different framework compositions and the minimisation of defects and shrinkage. Several promising applications have however already been suggested for these new structures some of which are discussed in further detail below.

a. Photonic crystals

The main feature that separates macroporous materials from their meso and microporous counterparts is their ability to act as a photonic crystal. The underlying concept behind photonic crystal materials stems from ideas presented in 1987 by Yablonovitch[66] and John[67] who suggested that a material with a periodical modulation of refractive index would be able to affect the photonic modes in a material giving rise to a photonic band gap (PBG). The PBG is analogous to a band gap in a semiconductor in that a certain range of energies of light cannot propagate through the photonic crystal.
This property leads to several exciting prospects for PBG materials; traditionally manipulation of light has relied upon internal reflections whilst the development of photonic crystal waveguides would enable light to be controlled in a manner analogous to the control of electrons by the electronic band gap of semi conductors.

The realisation of a complete PBG material is by no means trivial however as several requirements must be met. These requirements include a low solid fraction (~20-30 % solid by volume), for materials with a structure of close packed spheres the minimum refractive index contrast must be 2.8 and the periodicity must be uniform and with a lattice spacing comparable to the desired PBG wavelengths, furthermore any unwanted defects will serve to destroy the photonic band gap. These factors make it difficult to produce a complete photonic band gap material via colloidal crystal templating however there have been several examples in the literature of inverse opals exhibiting partial stop bands which are manifested as colourful reflections[68, 69]. The spectral position of these stop bands can be predictably altered over the entire visible spectrum by tailoring the pore sizes and the refractive index of the pore walls. The presence of a partial stop band means these materials remain potentially useful as special effect pigments, optical filters or chemical sensors.

b. Catalysis and separation

Any nanoporous material has applications in catalysis and separation on account of the large surface area inherent with these materials. Macroporous materials however typically have far lower surface areas than their mesoporous counterparts, typically in the region of 100 m^2 g^{-1}. Because of the comparatively low surface area the most promising catalytic materials are those which combine the large macroporous structure with the selectivity and catalytic benefits of micro- or mesoporous materials in a bimodal pore structure.

c. Lithium insertion electrode material

Lithium ion batteries first became commercially available in the early 1970's and have since become popularly used as power sources for portable electronic equipment. It has also been suggested that Lithium ion batteries would be suitable for applications in electric vehicles however for this to be realised it is necessary that the power density of lithium ion batteries is increased. The low power density is largely a result of polarization at high charging rate, which is due to the slow diffusion in the electrodes, resistance of the electrolyte and electrical resistance of active materials. A possible improvement to lithium ion batteries is the inclusion of porous electrode materials which reduces the polarization in a number of ways, namely the large surface area serves to decrease the current density per unit surface area of the electrode, the large pores facilitate mass

transport of electrolyte throughout the electrode and the thin pore walls minimize the solid phase diffusion length of the electrode material.

As yet only a few studies have been made with ordered macroporous electrodes. Most notably Sakamoto and Dunn[70] showed that the polarization was reduced by using macroporous electrodes and Yamada et al[71] further demonstrated a dependency upon the size of the macropores.

1.4 Hierarchically porous materials

One of the more recent areas of interest in nanoporous materials has been the development of synthesis and processing procedures for the production of porous materials with a hierarchy of pores with different length scales. The current interest is fuelled by a variety of potential applications for materials with multiscale porosity, particularly in the field of catalysis, where a meso/macro material would combine the very high surface area inherent in mesoporous materials with the large open pore framework, and consequent accessibility, of macroporous materials. This yields a material where the reactant species will have ready access to the interior pore structure and the surface area will also be maximised. Furthermore this structure would limit problems such as reactant pore blocking.

Multimodal materials are commonly found in nature but present a significant challenge to the materials chemist with synthetic challenges arising in controlling both the size and morphology at each pore length scale. The bulk of the preparative methods reported in this area favour a synthetic technique involving either the introduction of macro templates (e.g. latex spheres, bacteria etc) directly into reaction media or the combination of macro templates with usual mesoscale templates such as surfactant mesophases.

1.4.1 Synthesis

A variety of methods have been reported to produce hierarchically porous materials, the vast majority of these methods result in materials which have at best one well defined pore system with the second pore system being highly disorganised, some of these methods are touched upon in the following section but the main focus and the method most pertinent to the work presented in this thesis is the dual templating method described below.

Dual templating

Dual templating combines the synthetic ideas discussed in the previous two sections to produce materials with porosity in both the meso and macro size regimes.
The process involves utilising both latex spheres and surfactant aggregates simultaneously as structure directing agents. The latex spheres are packed into a colloidal crystal and templating around surfactant aggregates occurs in the voids within the colloidal crystal leading to a macroporous material with mesoporous pore walls.
This technique was first reported in 1998 by various authors but most notably Yang et al[72] who reported a range of hierarchically porous metal oxides (Niobia, silica, titania) which were patterned onto a substrate by micromoulding[73]. The synthetic procedure is highlighted below, (Figure 1.14):

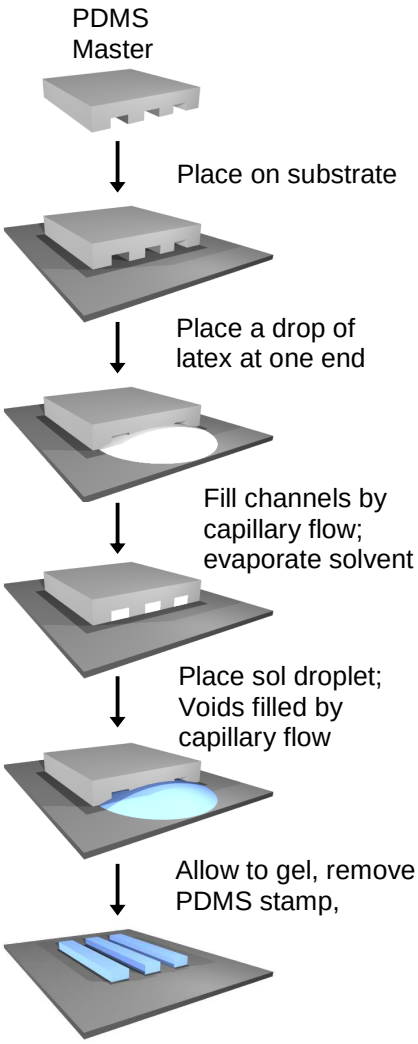

Figure 1.15: Schematic diagram of the moulding methods used to fabricate hierarchically ordered structures onto a substrate. Redrawn from [72].

Initially a polydimethylsiloxane (PDMS) micromoulded elastomeric stamp is fixed to the substrate before being filled by capillary force with a suspension of latex spheres. Upon evaporation of the solvent the latex spheres pack into a colloidal crystal within the confines of the micromould. Next a sol-gel solution containing a block copolymer is introduced into the voids of the colloidal crystal once again by capillary forces. After sol gelation both the surfactant and latex spheres are extracted by calcination and the PDMS micromould is removed yielding a patterned hierarchically ordered material (Figure 1.16).

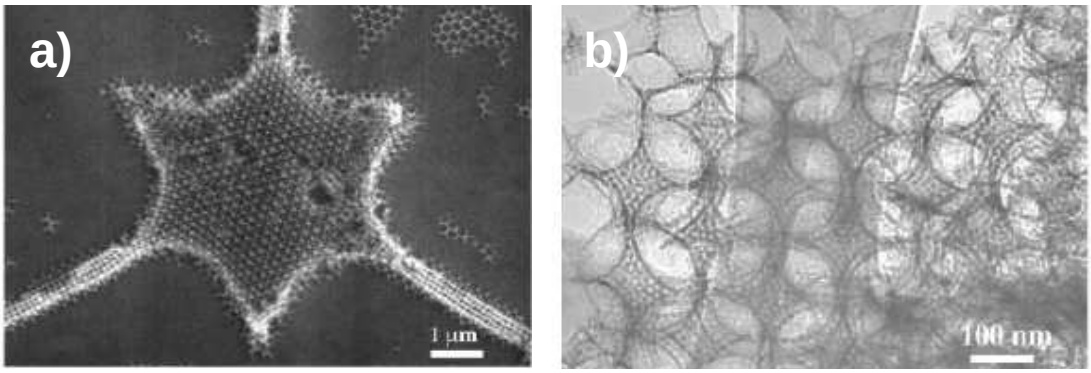

Figure 1.16: SEM image showing the moulded macrostructure of a silica material and b) TEM image showing the mesoporous pore walls of the same silica material. From [72]

The synthetic procedure outlined above is both long winded and limited to the production of very thin films. Recently Tiddy et al reported a simple one pot synthesis for the bulk scale production of meso/macroporous silica[74, 75]. The method involved adding a colloidal crystal monolith to a sol-gel solution containing both surfactant and co-surfactant. The formation mechanism suggested by the author centred on the idea that the silicate-micellar solution diffuses into the voids of the colloidal crystal monolith prior to precipitation around the PS spheres.

Further work by Kuang et al[76] reported the formation of a trimodal pore system with ordered macroporoes and both large and small mesopores (3 and 11 nm). In this case PS spheres, block copolymer and an ionic liquid (C_{16}mimCl) were used as templates in a simple one pot reaction.

1.4.2 Applications

As with the macroporous materials bimodal porous materials are still very new and as such applications are yet to be demonstrated, however there has been a lot of interest in these materials and many applications have been touted as ways to utilise these extraordinary structures. As already stated Meso/macro materials have considerable potential in the field of catalysis.

These structures also have great potential as adsorbents on account of the extremely large pore volume. Meso/macro materials have also been suggested as suitable materials for the study of fundamental studies of sorption theory such as diffusion and hysterisis[76].

1.5 References

(1) de Soler-Illia, G. J.; Sanchez, C.; Lebeau, B.; Patarin, J., Chemical Strategies To Design Textured Materials: from Microporous and Mesoporous Oxides to Nanonetworks and Hierarchical Structures. *Chemical Reviews (Washington, DC, United States)* **2002,** 102, (11), 4093-4138.

(2) Tanev, P. T.; Butruille, J.-R.; Pinnavaia, T. J., Nanoporous materials. *Chemistry of Advanced Materials* **1998**, 329-388.

(3) Schueth, F., Engineered porous catalytic materials. *Annual Review of Materials Research* **2005,** 35, 209-238, 3 plates.

(4) Davis, M. E.; Lobo, R. F., Zeolite and molecular sieve synthesis. *Chemistry of Materials* **1992,** 4, (4), 756-68.

(5) Sing, K. S. W.; Everett, D. H.; Haul, R. A. W.; Moscou, L.; Pierotti, R. A.; Rouquerol, J.; Siemieniewska, T., Reporting physisorption data for gas/solid systems with special reference to the determination of surface area and porosity (Recommendations 1984). *Pure and Applied Chemistry* **1985,** 57, (4), 603-19.

(6) Xiao, F.-S.; Qiu, S. L.; Pang, W. Q.; Xu, R. R., New developments in microporous materials. *Advanced Materials (Weinheim, Germany)* **1999,** 11, (13), 1091-1099.

(7) Attfield, M. P., Microporous materials. *Science Progress (St. Albans, United Kingdom)* **2002,** 85, (4), 319-345.

(8) Bu, X.; Feng, P., Crystalline microporous and open framework materials. *Chemistry of Nanostructured Materials* **2003**, 1-37.

(9) Cundy, C. S.; Cox, P. A., The hydrothermal synthesis of zeolites: Precursors, intermediates and reaction mechanism. *Microporous and Mesoporous Materials* **2005,** 82, (1-2), 1-78.

(10) Francis, R. J.; O'Hare, D., The kinetics and mechanisms of the crystallization of microporous materials. *Journal of the Chemical Society, Dalton Transactions: Inorganic Chemistry* **1998**, (19), 3133-3148.

(11) Barrer, R. M.; Denny, P. J., Hydrothermal chemistry of the silicates. IX. Nitrogenous aluminosilicates. *Journal of the Chemical Society, Abstracts* **1961**, 971-82.

(12) Schmidt, W., Application of microporous materials as ion-exchangers. *Handbook of Porous Solids* **2002,** 2, 1058-1097.

(13) Huddersman, K.; Klimczyk, M., Separation of branched hexane isomers using zeolite molecular sieves. *AIChE Journal* **1996,** 42, (2), 405-8.

(14) Fitch, F. R.; Bulow, M.; Ojo, A. F. X Zeolites for separation of gaseous mixtures with nitrogen. 95-300870
667183, 19950213., 1995.

(15) Maxwell, I. E.; Stork, W. H. J., Hydrocarbon processing with zeolites. *Studies in Surface Science and Catalysis* **2001,** 137, (Introduction to Zeolite Science and Practice (2nd Edition)), 747-819.

(16) Chen, N. Y.; Degnan, T. F., Industrial catalytic applications of zeolites. *Chemical Engineering Progress* **1988,** 84, (2), 32-41.

(17) Degnan, T. F., Jr., Applications of zeolites in petroleum refining. *Topics in Catalysis* **2000,** 13, (4), 349-356.

(18) Kresge, C. T.; Leonowicz, M. E.; Roth, W. J.; Vartuli, J. C.; Beck, J. S., Ordered mesoporous molecular sieves synthesized by a liquid-crystal template mechanism. *Nature (London, United Kingdom)* **1992,** 359, (6397), 710-12.

(19) Beck, J. S.; Vartuli, J. C.; Roth, W. J.; Leonowicz, M. E.; Kresge, C. T.; Schmitt, K. D.; Chu, C. T. W.; Olson, D. H.; Sheppard, E. W.; et al., A new family of mesoporous molecular sieves prepared with liquid crystal templates. *Journal of the American Chemical Society* **1992,** 114, (27), 10834-43.

(20) Attard, G. S.; Glyde, J. C.; Goltner, C. G., Liquid-crystalline phases as templates for the synthesis of mesoporous silica. *Nature (London)* **1995,** 378, (6555), 366-8.

(21) Das, T. K.; Chaudhari, K.; Chandwadkar, A. J.; Sivasanker, S., Synthesis and catalytic properties of mesoporous tin silicate molecular sieves. *Journal of the Chemical Society, Chemical Communications* **1995**, (24), 2495-6.

(22) Gontier, S.; Tuel, A., Synthesis and characterization of Ti-containing mesoporous silicas. *Zeolites* **1995,** 15, (7), 601-10.

(23) Reddy, K. M.; Moudrakovski, I.; Sayari, A., Synthesis of mesoporous vanadium silicate molecular sieves. *Journal of the Chemical Society, Chemical Communications* **1994**, (9), 1059-60.

(24) Sayari, A.; Reddy, K. M.; Moudrakovski, I., Synthesis of V and Ti modified MCM-41 mesoporous molecular sieves. *Studies in Surface Science and Catalysis* **1995,** 98, (Zeolite Science 1994: Recent Progress and Discussions), 19-21.

(25) Ciesla, U.; Demuth, D.; Leon, R.; Petroff, P.; Stucky, G.; Unger, K.; Schueth, F., Surfactant controlled preparation of mesostructured transition-metal oxide compounds. *Journal of the Chemical Society, Chemical Communications* **1994**, (11), 1387-8.

(26) Huo, Q.; Margolese, D. I.; Ciesla, U.; Demuth, D. G.; Feng, P.; Gier, T. E.; Sieger, P.; Firouzi, A.; Chmelka, B. F.; et al., Organization of Organic Molecules with Inorganic Molecular Species into Nanocomposite Biphase Arrays. *Chemistry of Materials* **1994,** 6, (8), 1176-91.

(27) Huo, Q.; Margolese, D. I.; Ciesla, U.; Feng, P.; Gier, T. E.; Sieger, P.; Leon, R.; Petroff, P. M.; Schueth, F.; Stucky, G. D., Generalized synthesis of periodic surfactant/inorganic composite materials. *Nature (London, United Kingdom)* **1994,** 368, (6469), 317-21.

(28) Yang, P.; Zhao, D.; Margolese, D. I.; Chmelka, B. F.; Stucky, G. D., Generalized syntheses of large-pore mesoporous metal oxides with semicrystalline frameworks. *Nature (London)* **1998,** 396, (6707), 152-155.

(29) Attard, G. S.; Bartlett, P. N.; Coleman, N. R. B.; Elliott, J. M.; Owen, J. R.; Wang, J. H., Mesoporous platinum films from lyotropic liquid crystalline phases. *Science (Washington, D. C.)* **1997,** 278, (5339), 838-840.

(30) Gabriel, T.; Nandhakumar, I. S.; Attard, G. S., Electrochemical synthesis of nanostructured tellurium films. *Electrochemistry Communications* **2002,** 4, (8), 610-612.

(31) Nandhakumar, I.; Elliott, J. M.; Attard, G. S., Electrodeposition of nanostructured mesoporous selenium films (HI-eSe). *Chemistry of Materials* **2001,** 13, (11), 3840-3842.

(32) Nelson, P. A.; Elliott, J. M.; Attard, G. S.; Owen, J. R., Mesoporous Nickel/Nickel Oxide-a Nanoarchitectured Electrode. *Chemistry of Materials* **2002,** 14, (2), 524-529.

(33) Wanka, G.; Hoffmann, H.; Ulbricht, W., Phase Diagrams and Aggregation Behavior of Poly(oxyethylene)-Poly(oxypropylene)-Poly(oxyethylene) Triblock Copolymers in Aqueous Solutions. *Macromolecules* **1994,** 27, (15), 4145-9.

(34) Vartuli, J. C.; Kresge, C. T.; Roth, W. J.; McCullen, S. B.; Beck, J. S.; Schmitt, K. D.; Leonowicz, M. E.; Lutner, J. D.; Sheppard, E. W., Designed synthesis of mesoporous molecular sieve systems using surfactant-directing agents. *Advanced Catalysts and Nanostructured Materials* **1996**, 1-19.

(35) Chen, C. Y.; Burkett, S. L.; Li, H. X.; Davis, M. E., Studies on mesoporous materials. II. Synthesis mechanism of MCM-41. *Microporous Materials* **1993,** 2, (1), 27-34.

(36) Monnier, A.; Schuth, F.; Huo, Q.; Kumar, D.; Margolese, D.; Maxwell, R. S.; Stucky, G. D.; Krishnamurty, M.; Petroff, P.; et al., Cooperative formation of inorganic-organic interfaces in the synthesis of silicate mesostructures. *Science (Washington, DC, United States)* **1993,** 261, (5126), 1299-303.

(37) Stucky, G. D.; Monnier, A.; Schueth, F.; Huo, Q.; Margolese, D.; Kumar, D.; Krishnamurty, M.; Petroff, P.; Firouzi, A.; et al., Molecular and atomic arrays in nano- and mesoporous materials synthesis. *Molecular Crystals and Liquid Crystals Science and Technology, Section A: Molecular Crystals and Liquid Crystals* **1994,** 240, 187-200.

(38) Steel, A.; Carr, S. W.; Anderson, M. W., 14N NMR study of surfactant mesophases in the synthesis of mesoporous silicates. *Journal of the Chemical Society, Chemical Communications* **1994**, (13), 1571-2.

(39) Firouzi, A.; Kumar, D.; Bull, L. M.; Besier, T.; Sieger, P.; Huo, Q.; Walker, S. A.; Zasadzinski, J. A.; Glinka, C.; Nicol, J., Cooperative organization of inorganic-surfactant and biomimetic assemblies. *Science* **1995,** 267, (5201), 1138-43.

(40) Brinker, C. J., Evaporation-induced self-assembly. Functional nanostructures made easy. *MRS Bulletin* **2004,** 29, (9), 631-640.

(41) Viswanathan, B.; Jacob, B., Alkylation, hydrogenation and oxidation catalyzed by mesoporous materials. *Catalysis Reviews - Science and Engineering* **2005,** 47, (1), 1-82.

(42) Corma, A.; Navarro, M. T.; Perez Pariente, J., Synthesis of an ultralarge pore titanium silicate isomorphous to MCM-41 and its application as a catalyst for selective oxidation of hydrocarbons. *Journal of the Chemical Society, Chemical Communications* **1994**, (2), 147-8.

(43) Tanev, P. T.; Chibwe, M.; Pinnavaia, T. J., Titanium-containing mesoporous molecular sieves for catalytic oxidation of aromatic compounds. *Nature (London, United Kingdom)* **1994,** 368, (6469), 321-3.

(44) Whitehead, A. H.; Elliott, J. M.; Coleman, N. R. B.; Bartlett, P. N.; Attard, G. S.; Owen, J. R., The formation and characterization of mesoporous tin for use in Li-ion batteries. *Proceedings - Electrochemical Society* **1999,** 98-16, (Lithium Batteries), 128-133.

(45) Nelson, P. A.; Elliott, J. M.; Attard, G. S.; Owen, J. R., Mesoporous nickel/nickel oxide electrodes for high power applications. *Journal of New Materials for Electrochemical Systems* **2002,** 5, (1), 63-65.

(46) Liu, P.; Lee, S.-H.; Tracy, C. E.; Turner, J. A., Mesoporous vanadium oxide as cathodes for lithium batteries. *Proceedings - Electrochemical Society* **2003,** 2001-21, (Batteries and Supercapacitors), 183-187.

(47) Ganguli, R.; Lu, Y.; Anderson, M. T.; Drewien, C. A.; Brinker, C. J.; Soyez, H.; Dunn, B.; Huang, M. H.; Zink, J. I., Rapid continuous formation of supported mesoporous films from homogeneous sols by a surfactant-templated mechanism. *Book of Abstracts, 213th ACS National Meeting, San Francisco, April 13-17* **1997**, COLL-350.

(48) Lu, Y.; Ganguli, R.; Drewien, C. A.; Anderson, M. T.; Brinker, C. J.; Gong, W.; Guo, Y.; Soyez, H.; Dunn, B.; Huang, M. H.; Zink, J. I., Continuous formation of supported cubic and hexagonal mesoporous films by sol-gel dip-coating. *Nature (London)* **1997,** 389, (6649), 364-368.

(49) Zhao, D.; Yang, P.; Huo, Q.; Chmelka, B. F.; Stucky, G. D., Topological construction of mesoporous materials. *Current Opinion in Solid State & Materials Science* **1998,** 3, (1), 111-121.

(50) Hyodo, T., Sensitivity enhancement of chemical sensors induced by control of their mesoporous and macroporous structures. *Chemical Sensors* **2005,** 21, (1), 8-12.

(51) Velev, O. D.; Jede, T. A.; Lobo, R. F.; Lenhoff, A. M., Porous silica via colloidal crystallization. *Nature (London)* **1997,** 389, (6650), 447-448.

(52) Xia, Y.; Gates, B.; Yin, Y.; Lu, Y., Monodispersed colloidal spheres: Old materials with new applications. *Advanced Materials (Weinheim, Germany)* **2000,** 12, (10), 693-713.

(53) Stein, A.; Schroden, R. C., Colloidal crystal templating of three-dimensionally ordered macroporous solids: materials for photonics and beyond. *Current Opinion in Solid State & Materials Science* **2001,** 5, (6), 553-564.

(54) Subramaniam, G.; Pine, D. J., Macroporous ceramics by colloidal templating. *Proceedings of SPIE-The International Society for Optical Engineering* **2000,** 3937, (Micro- and Nano-photonic Materials and Devices), 28-35.

(55) Kuang, D.-B.; Wu, Y.; Ou, H.-D.; Fang, Y.-P.; Xu, A.-W.; Liu, H.-Q., Preparation of ordered macroporous titania. *Yingyong Huaxue* **2003,** 20, (1), 92-94.

(56) Kuai, S.; Badilescu, S.; Bader, G.; Bruning, R.; Hu, X.; Truong, V.-V., Preparation of large-area 3D ordered macroporous titania films by silica colloidal templating. *Advanced Materials (Weinheim, Germany)* **2003,** 15, (1), 73-75.

(57) Zhou, Z.; Ong, W. C.; Zhao, G. X. S., Ordered macroporous materials structurally templated by colloidal microspheres. *Adsorption Science and Technology, Proceedings of the Pacific Basin Conference, 3rd, Kyongju, Republic of Korea, May 25-29, 2003* **2003**, 329-333.

(58) Kuai, S.-L.; Bader, G.; Hache, A.; Truong, V.-V.; Hu, X.-F., High quality ordered macroporous titania films with large filling fraction. *Thin Solid Films* **2005,** 483, (1-2), 136-139.

(59) Sokolov, S.; Bell, D.; Stein, A., Preparation and characterization of macroporous a-alumina. *Journal of the American Ceramic Society* **2003,** 86, (9), 1481-1486.

(60) Shen, Y.; Wu, Q.-Z.; Liao, J.-F.; Li, Y.-G., Synthesis and characterization of three-dimensionally ordered macroporous (3DOM) titania-silica mixed oxides. *Wuji Cailiao Xuebao* **2003,** 18, (2), 401-406.

(61) Yan, H.; Blanford, C. F.; Holland, B. T.; Smyrl, W. H.; Stein, A., General Synthesis of Periodic Macroporous Solids by Templated Salt Precipitation and Chemical Conversion. *Chemistry of Materials* **2000,** 12, (4), 1134-1141.

(62) Bartlett, P. N.; Birkin, P. R.; Ghanem, M. A., Electrochemical deposition of macroporous platinum, palladium and cobalt films using polystyrene latex sphere templates. *Chemical Communications (Cambridge)* **2000**, (17), 1671-1672.

(63) Bartlett, P. N.; Dunford, T.; Ghanem, M. A., Templated electrochemical deposition of nanostructured macroporous PbO2. *Journal of Materials Chemistry* **2002,** 12, (10), 3130-3135.

(64) Bartlett, P. N.; Baumberg, J. J.; Birkin, P. R.; Ghanem, M. A.; Netti, M. C., Highly Ordered Macroporous Gold and Platinum Films Formed by Electrochemical Deposition through Templates Assembled from Submicron Diameter Monodisperse Polystyrene Spheres. *Chemistry of Materials* **2002,** 14, (5), 2199-2208.

(65) Bartlett, P. N.; Ghanem, M. A.; El Hallag, I. S.; De Groot, P.; Zhukov, A., Electrochemical deposition of macroporous magnetic networks using colloidal templates. *Journal of Materials Chemistry* **2003,** 13, (10), 2596-2602.

(66) Yablonovitch, E., Inhibited spontaneous emission in solid-state physics and electronics. *Physical Review Letters* **1987,** 58, (20), 2059-62.

(67) John, S., Strong localization of photons in certain disordered dielectric superlattices. *Physical Review Letters* **1987,** 58, (23), 2486-9.

(68) Schroden, R. C.; Al-Daous, M.; Stein, A., Self-Modification of Spontaneous Emission by Inverse Opal Silica Photonic Crystals. *Chemistry of Materials* **2001,** 13, (9), 2945-2950.

(69) Schroden, R. C.; Al-Daous, M.; Blanford, C. F.; Stein, A., Optical Properties of Inverse Opal Photonic Crystals. *Chemistry of Materials* **2002,** 14, (8), 3305-3315.

(70) Sakamoto, J. S.; Dunn, B., Hierarchical battery electrodes based on inverted opal structures. *Journal of Materials Chemistry* **2002,** 12, (10), 2859-2861.

(71) Yamada, H.; Yamato, T.; Moriguchi, I.; Kudo, T., Interconnected macroporous TiO2 (anatase) as a lithium insertion electrode material. *Solid State Ionics* **2004,** 175, (1-4), 195-198.

(72) Yang, P.; Deng, T.; Zhao, D.; Feng, P.; Pine, D.; Chmelka, B. F.; Whitesides, G. M.; Stucky, G. D., Hierarchically ordered oxides. *Science (Washington, D. C.)* **1998,** 282, (5397), 2244-2247.

(73) Trau, M.; Yao, N.; Kim, E.; Xia, Y.; Whitesides, G. M.; Aksay, I. A., Microscopic patterning of oriented mesoscopic silica through guided growth. *Nature (London)* **1997,** 390, (6661), 674-676.

(74) Sen, T.; Tiddy Gordon, J. T.; Casci John, L.; Anderson Michael, W., One-pot synthesis of hierarchically ordered porous-silica materials with three orders of length scale. *Angewandte Chemie (International ed. in English)* **2003,** 42, (38), 4649-53.

(75) Sen, T.; Tiddy, G. J. T.; Casci, J. L.; Anderson, M. W., Synthesis and Characterization of Hierarchically Ordered Porous Silica Materials. *Chemistry of Materials* **2004,** 16, (11), 2044-2054.

(76) Kuang, D.; Brezesinski, T.; Smarsly, B., Hierarchical Porous Silica Materials with a Trimodal Pore System Using Surfactant Templates. *Journal of the American Chemical Society* **2004,** 126, (34), 10534-10535.

(77) Coleman, N., Direct liquid crystal templating of mesoporous silica and platinum. *PhD Thesis. University of Southampton*, **2001.**

Chapter 2

Contents page

EXPERIMENTAL

CHAPTER 2 – EXPERIMENTAL

The present chapter provides details about the experimental aspects developed in this thesis as well as the instrumentation employed. The fundamental principles of the dip-coating technique are an important principle of the work presented in this thesis and the key points will be discussed in this section. Furthermore the principles of sol-gel chemistry will be described in detail, as this too is pertinent to the work presented here.

2.1 Sol-gel technique

The sol-gel process is the principal chemical technique employed in this work in the production of a variety of nanoporous materials through templating around various nanoscale architectures. It is a versatile method used to produce a variety of inorganic networks, most commonly, from silicon or metal alkoxide precursors. The name sol-gel gives an insight into the process, which involves the evolution of an inorganic network through the formation of a colloidal suspension (the sol) followed by gelation of this suspension to form a network within a liquid phase.

The sol-gel process has received a great deal of attention due to its versatility in producing a variety of different products (Figure 2.1) for example if the liquid in a wet gel is removed under a supercritical condition, a highly porous and extremely low density material called an aerogel is obtained. Ultra-fine and uniform ceramic powders can also be formed by precipitation, spray pyrolysis, or emulsion techniques.

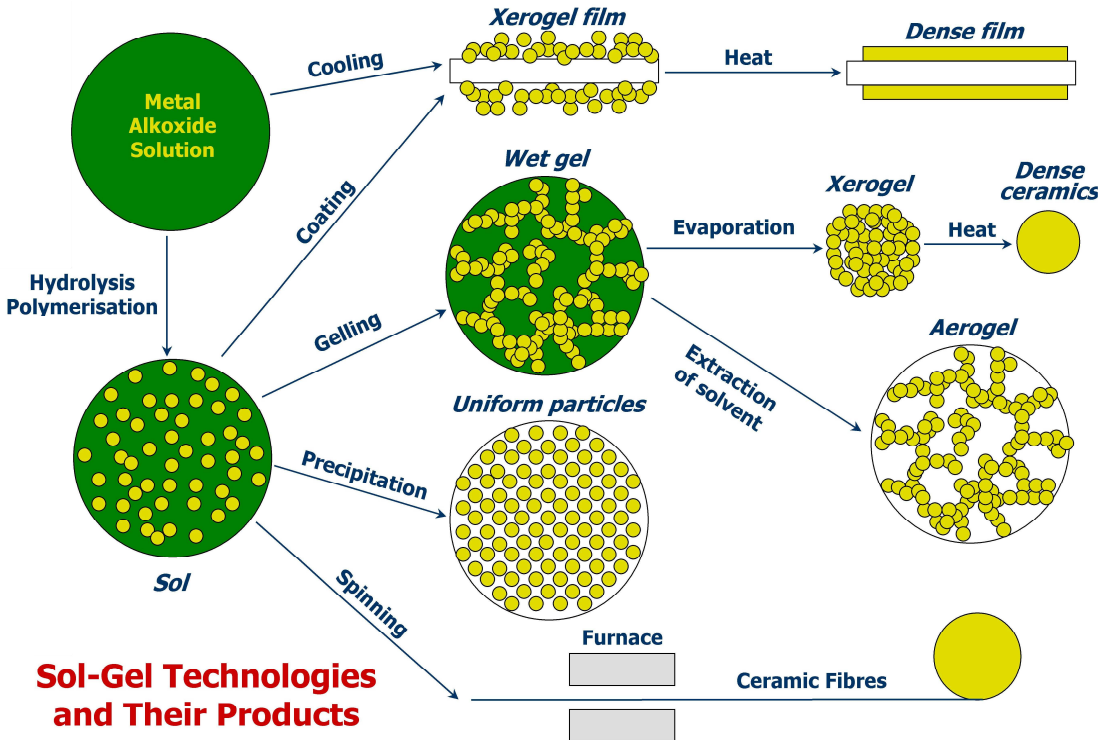

Figure 2.1: Schematic representation highlighting the versatility of the sol-gel process[Redrawn from: ttp://www.chemat.com/html/solgel.html]

At a functional level the process can be described by three reactions (Highlighted below in Figure 2.2 for a silicon alkoxide), namely hydrolysis followed by condensation.

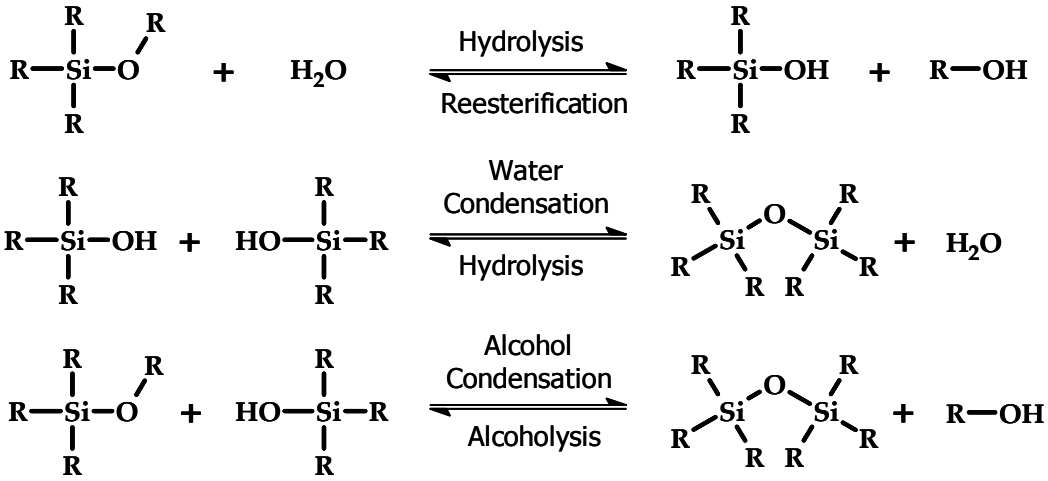

Figure 2.2: The three reactions used to describe the sol-gel process.

In the case of silicon alkoxides the reactions lead to the production of a siloxane bond plus the by product, water or alcohol. The properties of the final silica framework are dependant on the relative rates at which the hydrolysis and condensation reactions occur which in turn are dependent on a large number of factors, in particular pH, temperature and H_2O/Si molar ratio. If the hydrolysis step is fast with respect to the condensation step the final product will be highly branched and, as such, a very dense network. In contrast if the condensation step is fast with respect to the condensation step the final network will be less dense and contain less branching.

2.2 Sol-gel Dip Coating

All the materials fabricated for this thesis were prepared using some variation on a sol gel dip coating technique and as such it is prudent to discuss the theoretical aspects of this technique. The sol gel dip coating process as the name suggests involves withdrawing a substrate vertically from a sol gel solution at a constant speed (U_0). The moving substrate entrains the liquid in a boundary layer that splits into two (Figure 2.3b) returning the outer layer into the bath. Figure 2.3a gives a schematic representation of the sequential stages of film formation that occur during a sol-gel dip coating process.

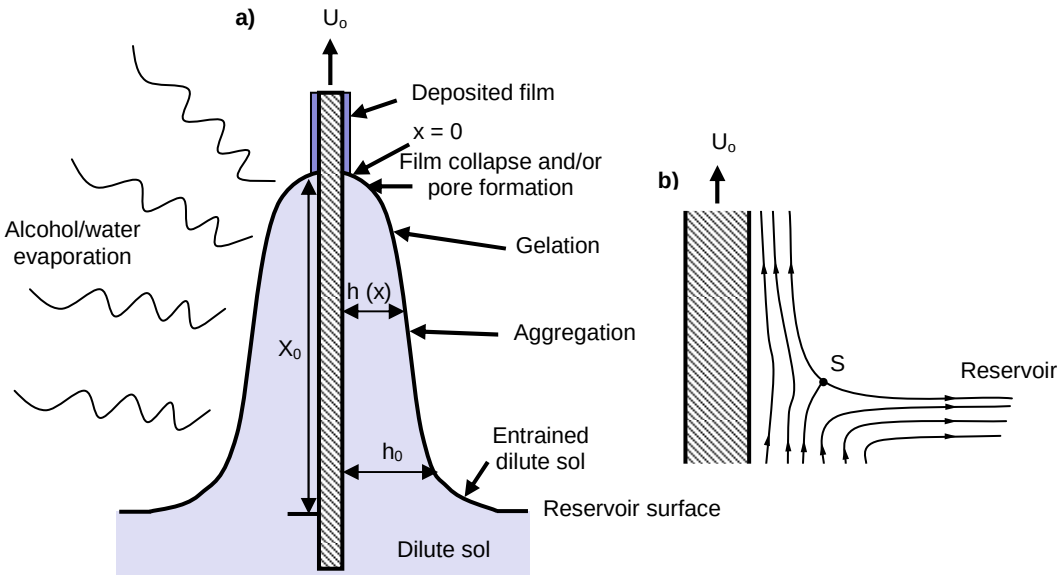

Figure 2.3: a) Schematic representation of the sol gel dip coating process, b)Details of flow patterns during dip coating. Redrawn from[1]

Initially the solvent evaporates and drains causing the fluid film to acquire an approximate wedge like shape terminating in a well defined drying line (x = 0, in figure 2.3a). Once the withdrawal speed equals that of the receding drying line the process is steady state with respect to the reservoir surface. For alcohol rich fluids, common to sol-gel processes, steady state conditions are typically obtained in a couple of seconds. Under steady-state flow, the evolution of the thickness of a liquid film upon a substrate is related to the position of the streamline dividing the upward and downward moving layers (S in Figure 2.3b) which is governed by competition between as many as these six different forces:

1) Viscous drag by the moving substrate
2) Gravity
3) Surface tension in the concavely shaped meniscus
4) Inertial force of the boundary layer liquid arriving at the deposition region
5) Surface tension gradient
6) The disjoining or conjoining layer

When the withdrawal speed and liquid viscocity (η) is low as is normally the case in sol-gel dip coating systems, the entrained thickness is dependant upon the viscous drag ($\eta U_0 / h$), gravity force ($\rho g h$) and liquid vapour surface tension (γ_{LV}) as derived by Landau and Levich [2]:

$$h_0 = \frac{0.94(\eta U_0)^{2/3}}{\gamma_{LV}^{1/6}(\rho g)^{1/2}} \qquad \text{Equation 2.1}$$

where ρ is the liquid density and g is the acceleration by gravity.

This equation shows that the thickness of any film deposited by a dip coating process will be largely dependant on the withdrawal speed and the solution viscosity.

2.3 Electron microscopy

Electron microscopy was used throughout this research to study both the morphology and chemistry of the nanoporous materials presented in this work. The three techniques employed were Scanning Electron Microscopy (SEM), Transmission Electron Microscopy (TEM) and Energy Dispersive X-ray analysis (EDX). What follows is an introduction to electron microscopy with particular emphasis on these three techniques.

2.3.1 Introduction

In general, radiation of a given wavelength cannot be used to probe structural details much smaller than its own wavelength, which represents a fundamental limitation of both light and electron microscopes. The ultimate limit of resolution of a light microscope is, therefore, set by the wavelength of visible light, which ranges from about 400 to 700 nm. A beam of electrons on the other hand can be considered as a beam of radiation with a wavelength ranging from 0.01 to 0.001 nm. In reality however the ultimate resolution of an electron microscope is significantly lower than this because the aberrations of an electron lens are considerably harder to correct than those of a glass lens. In practise the maximum resolving power of most modern electron microscopes is about 0.2 nm, which is approximately the separation of atoms in a crystalline solid.

In order to understand the techniques afforded by electron microscopy it is important to understand the ways in which an electron beam can interact with the atoms of a specimen and these interactions can be categorised as follows:

Elastic scattering

Elastic scattering defines a process which although it may change the direction of the primary electron it does not change its energy. The process is a result of Coulombic interactions between the primary electrons and both the nucleus and the surrounding electrons in the sample. The strength of scattering by any particular atom is therefore heavily dependent on its atomic number.

Inelastic scattering

Inelastic scattering is a very general term relating to any process which causes primary electrons to lose a detectable amount of energy. There are several processes that may cause the primary electrons to lose energy when interacting with a sample but the four most common are phonon scattering, plasmon scattering, single valence electron excitation and inner shell excitation. Inelastic scattering processes are eventually responsible for the stopping of an electron by a solid. The majority of the kinetic energy carried by the electron will end up as heat in the specimen whilst a small portion may escape as X-rays, light or secondary electrons.

Secondary effects

A secondary effect can loosely be defined as an effect caused by the primary beam which can be detected outside the specimen and these effects are extremely useful for both imaging and analysis. The secondary effects are summarised below in figure 2.4.

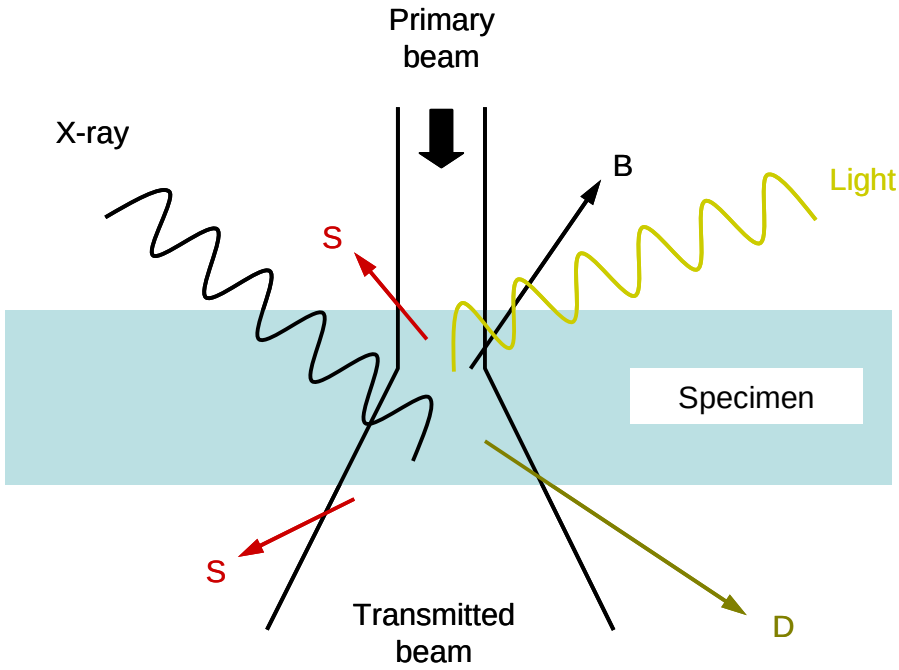

Figure 2.4: Schematic representation of the secondary effects utilised in electron microscopy. S = secondary electrons, B = backscattered electrons and D = diffracted electrons.

For electron microscopy it is convenient to categorise these secondary effects into 5 categories:

I Secondary electrons

This is a very broad term used to describe electrons which escape from the sample with their energies below 50 eV. These could be primary electrons which have undergone several inelastic collisions before escaping from the sample with reduced energy but are more commonly electrons that were originally in the specimen within a short distance of the surface to which a small amount of energy has been transferred allowing them to escape the sample.

II Backscattered electrons

These are the primary electrons that leave the specimen without giving up all their energy. Backscattered electrons are not as numerous as secondary electrons and most of them carry very high energies.

III-V Relaxation of excited atoms

If an electron is knocked out of an atom that atom is in an excited state, subsequent relaxation of the atom to a ground state will be accompanied by some energy emission. There are essentially three ways this relaxation can occur:

i. Cathodoluminescence – Emission of a photon in the visible range.
ii. X-ray emission
iii. Auger emission – this is when an outer electron, which carries the excess energy as kinetic energy, is emitted and forms the basis of auger electron spectroscopy.

2.3.2 Transmission Electron Microscopy

Transmission electron microscopy is widely used to examine mesoporous materials. The technique involves passing a parallel beam of electrons through a thin slice of specimen to form an image from the transmitted electrons. The technique is analogous to a standard upright or inverted light microscope. Dense areas of the sample absorb or scatter the beam, producing dark spots; whereas less dense regions such as pores do not adsorb or scatter the beam as strongly and as such appear lighter.

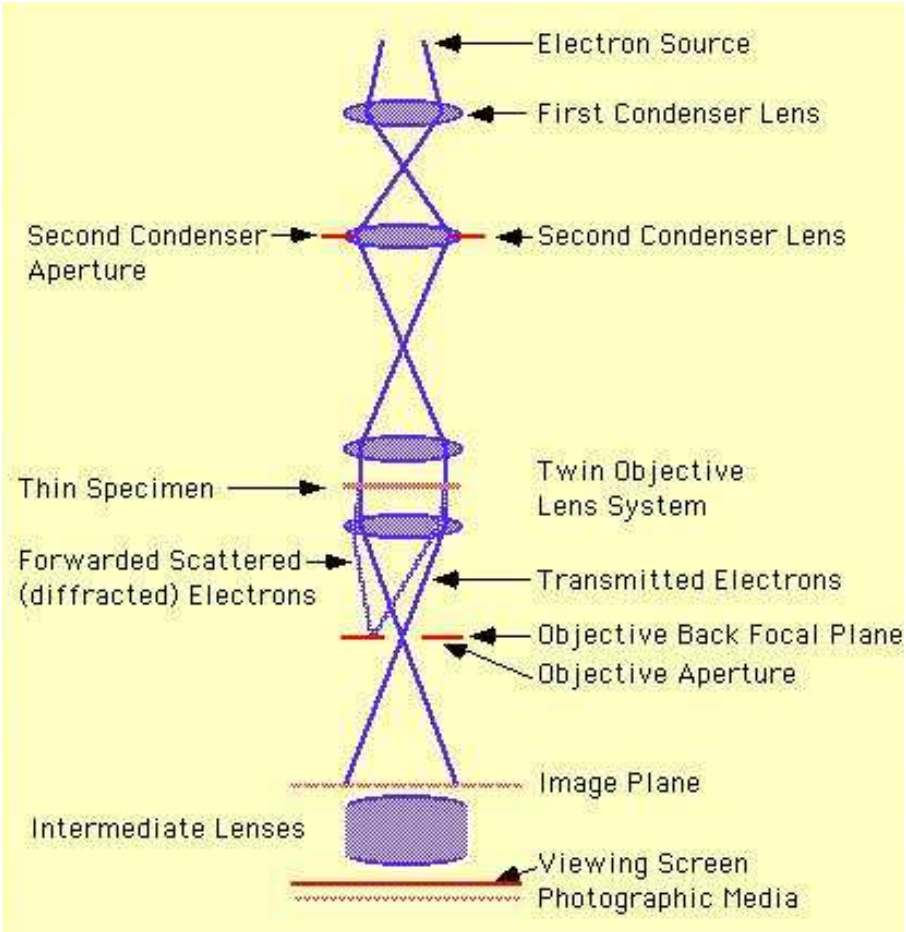

Figure 2.5: Schematic representation of a transmission electron microscope. John Mansfield, University of Michigan.

The electrons are emitted by an electron gun which accelerates the electrons produced from a filament. The accelerating voltage is typically between 100 and 300 kV allowing the beam to penetrate the specimen. Below the electron gun are two or more condenser lenses, which both demagnify the beam emitted by the gun and control the beam diameter as it hits the specimen. Next the objective lens serves to focuses the electron beam onto the surface of the specimen. Beneath the specimen chamber a series of

lenses serve to magnify and focus the transmitted image before the image is projected onto a fluorescent screen[8].

Instrumentation

All the TEM images presented in this thesis were obtained on a Jeol 3010 high resolution transmission electron microscope (Figure 2.6) working with an accelerating voltage of 300 keV. The maximum resolution of the TEM is 0.21 nm and as such the microscope is appropriate for the observation of mesostructures within materials.

Figure 2.6: Photograph of the Jeol 3010 transmission electron microscope.

Sample preparation

All samples were prepared for the TEM in precisely the same way. Initially ca. 1 mg of material was ground with a mortar and pestle for 3 minutes before adding ~ 1 ml of distilled water. This suspension was then sonicated for 15 minutes, using a Branson 1210

sonicator, to further reduce the particle size after which one droplet was placed onto a 3.05 mm dia. copper TEM grid (supplied by Agar scientific). The copper grid was then placed into an oven at 60 °C for 30 minutes allowing the water to evaporate.

2.3.3 Scanning Electron Microscopy and Energy Dispersive X-ray Analysis

The SEM is similar to the TEM in that they both employ a beam of electrons to illuminate the sample. Hence both instruments contain similar components, such as the electron gun and condenser lenses. However, whereas the TEM provides information about the internal structure of thin specimens the SEM primarily provides information about the surface morphology of a specimen. The technique involves rastering a focussed beam of electrons over a sample and creating an image by detecting the backscattered or secondary electrons. Detection of backscattered electrons provides contrast relating to the composition of the sample whilst detection of secondary electrons provides an image related to the surface morphology of the sample.

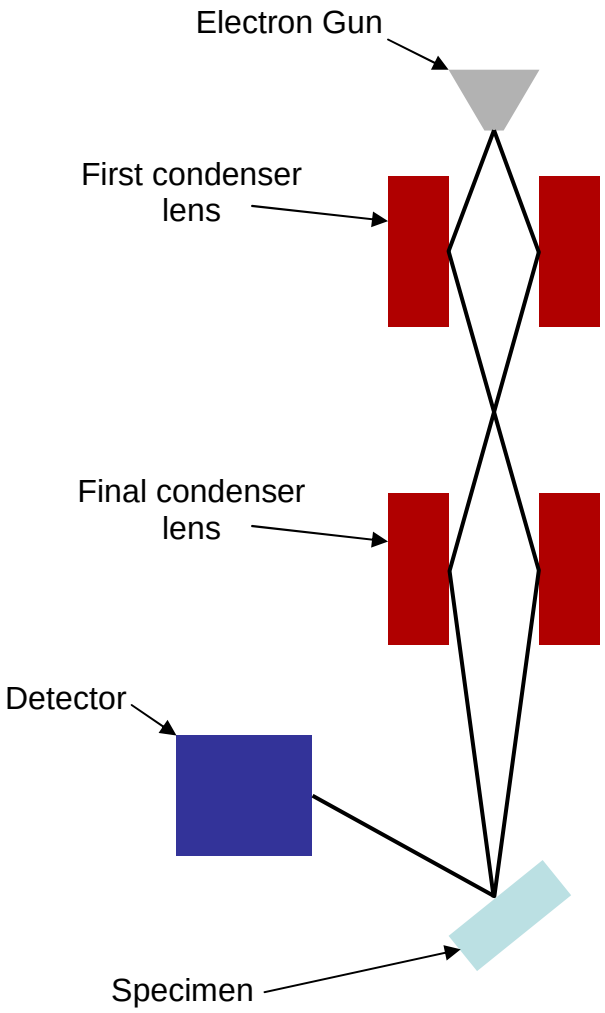

Figure 2.7: Schematic representation of a scanning electron microscope.

As with the TEM the electrons are formed by an electron gun which accelerates the electrons produced from a filament. The accelerating voltage is much lower than that used in the TEM and is typically in the region of 1 - 30 keV. Next two or three condenser lenses demagnify the beam so it has a diameter of only 2-10 nm when it hits the specimen and detectors in the specimen chamber detect the secondary or backscattered electrons. Most modern SEM's have facilities to detect both secondary and backscattered electrons however the most widely used signal in the SEM is that from the secondary electrons which are detected by a scintillator-photomultiplier system.

Modern SEM's often come equipped with X-ray detectors, enabling chemical analysis of the material under observation by energy dispersive X-ray analysis. The principle of EDX is quite simple suffice to say that all elements emit characteristic X-ray radiation when excited by an electron beam and as such detection of the energies of the emitted X-rays allows the atoms present in the sample to be identified. Whilst the peak positions can

qualitatively determine the elements present in a sample measuring the peak intensities allows quantitative data about the composition of a sample to be derived.

Instrumentation

Over the course of the thesis two different instruments were used. The first was a JSM 5910 scanning electron microscope. The instrument has a maximum resolution of 3 nm at 30 keV and comes equipped with an Oxford IncaEnergy 350 EDX microanalysis system. This microscope was used to collect all the EDX data presented in this work.

The second instrument was a JSM 6500F thermal field emission scanning electron microscope (Figure 2.9) which has a maximum resolution of 1.5 nm at 30 keV. This was the primary resource used to obtain the images presented in the thesis.

Figure 2.8: Photograph of the JSM 6500F thermal field emission scanning electron microscope.

Sample preparation

Samples were adhered to an aluminium stub using a double sided carbon pad. With the exception of the work done on platinum none of the samples were conductive and as such it was necessary to coat the samples with a thin layer of gold (ca 20 nm) using a Hummer® sputtering system prior to observation in the SEM.

2.4 Nitrogen adsorption/desorption experiments

High surface area and narrow pore size distribution are important attributes of nanoporous materials. Hence the ability to quantify these values is essential when characterising any nanoporous material. The most common method of evaluating the surface area and pore size distribution of nanoporous materials involves studying the adsorption and desorption of an inert gas such as nitrogen onto the surface of the material at liquid nitrogen temperature and relative pressures (P/P_0, where P_0 = 1 atm) ranging from 0.05 – 1. Nitrogen adsorption studies are widely reported in the literature for a range of nanoporous materials[3, 4].

2.4.1 Instrumentation

All the nitrogen adsorption/desorption isotherms presented in this thesis were collected on a Micromeritics Gemini 2375 Surface Area Analyser (Figure 2.9). The machine uses a flowing gas technique in which the analysis gas flows into a tube containing the sample and a balance tube at the same time. The internal volume and temperature surrounding both tubes are maintained at identical conditions with the presence of the sample being the only difference.

The sample and balance tubes are immersed into a liquid nitrogen bath prior to delivery of the analysis gas. A pressure transducer then measures the pressure imbalance between the sample and balance tube which is caused by the adsorption of analysis gas onto the sample. As the sample adsorbs more analysis gas the pressure drops in the sample tube and more gas is admitted to restore the pressure balance between the two tubes. The net result is that a constant pressure in both tubes is maintained whilst varying the analysis gas delivery to exactly match the rate at which the sample can adsorb or desorb. Figure 2.9 shows both a schematic and a plumbing diagram of the Gemini 2375.

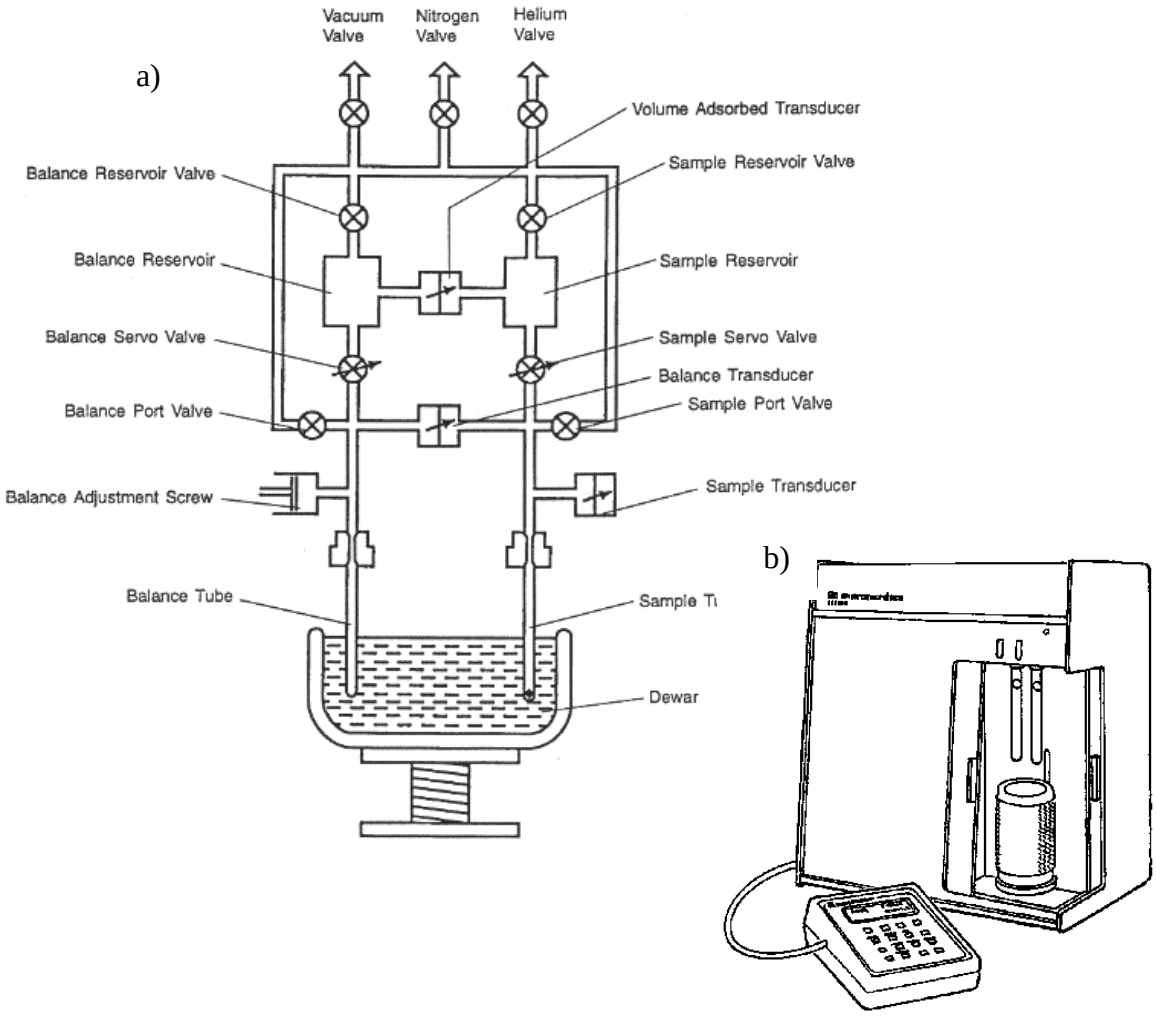

Figure 2.9: a) Plumbing diagram and b) General overview of the Gemini 2375.

2.4.2 Sample Preparation

For all the nitrogen adsorption/desorption isotherms presented in this thesis the samples were prepared as follows:

1. Samples were dried at 60 °C for 24 hours prior to analysis.
2. Sample tubes were cleaned by sonicating in deionised water for 15 minutes before rinsing with deionised water and drying in an oven at 60 °C for 24 hours.

3. Samples were weighed out accurately into the analysis tubes (Typically ca ~ 60 mg)
4. The instrument was set up with the following parameters:
   a. 20 adsorption points and 20 desorption points between P/P_0 0.04 and 0.98
   b. Saturation pressure 760 mm Hg
   c. Evacuation rate 300 mmHg min^{-1}
   d. Evacuation time 20 minutes

e) The BET machine was directed to carry out BET analysis on relative pressures (P/P_0) between 0.08 and 0.35. A BJH pore size distribution report on the desorption data was also collected and the pore volumes were obtained at a relative pressure of 0.98.

2.4.3 Analysis of results

The quantity of nitrogen adsorbed by a solid is proportional to the mass of the solid, the pressure and the nature of the solid at a given temperature. For a given temperature and solid, the relationship between the amount of nitrogen adsorbed and the relative pressure can be expressed as:

$$V = f(P/P_o)_{T,gas,solid} \qquad \text{Equation 2.1}$$

V is the amount or volume of nitrogen adsorbed by the solid, P is the vapour pressure and P_o is the saturated vapour pressure. Adsorption isotherms, such as those in figure 7 were constructed by plotting the volume of nitrogen adsorbed (V) against the relative pressure (P/P_o).

a. Sorption Isotherms

Nitrogen adsorption isotherms are extremely useful to determine structural details of nanoporous materials. Initially at very low relative pressures, a monolayer of nitrogen molecules forms on the surface of the solid. As the limit of monolayer coverage is reached, nitrogen begins to condense and fill in the very smallest pores of the sample. Further increases in the relative pressure result in the filling of steadily larger pores IUPAC distinguished six types of adsorption isotherms accounting for the majority of isotherms and these are shown below in figure 2.10.

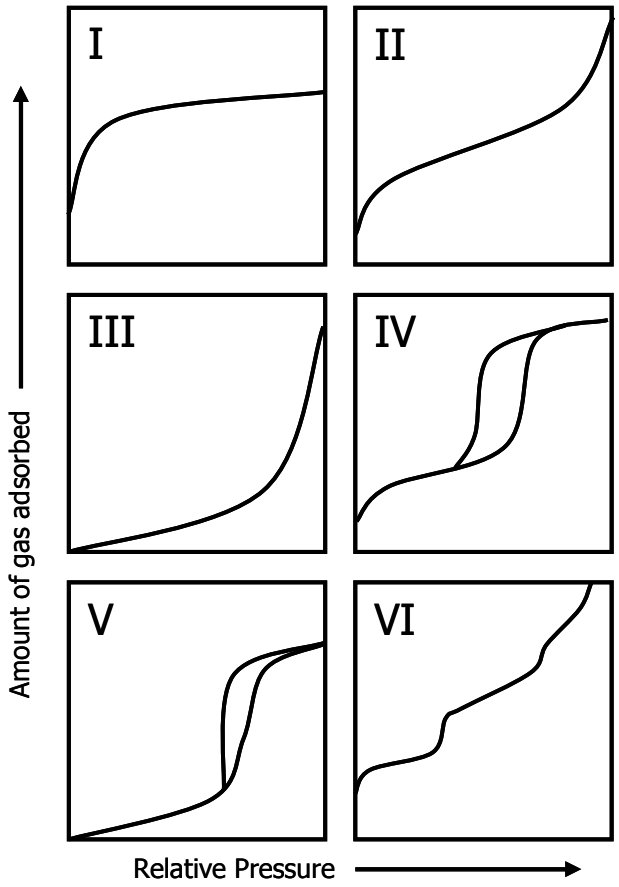

Figure 2.10: The six types of sorption isotherm as defined by Brunauer at al[5].

The reversible Type I isotherms are given by microporous solids having relatively small external surface areas, the initial rise in adsorption corresponds to nitrogen filling the micropores after-which multilayer growth gives a steady increase in adsorption. The reversible Type II isotherm is characteristic of a non-porous or macroporous adsorbent. It represents unrestricted monolayer-multilayer adsorption. The reversible Type III isotherms are not uncommon, but there are a number of systems (e.g. nitrogen on

polyethylene) which give isotherms with gradual curvature. Type IV isotherms are characteristic of mesoporous materials the sharp jump in adsorption corresponding to the pressure at which nitrogen condenses into the mesopores. Another characteristic feature of the Type IV isotherm is the hysteresis loop, which is associated with capillary condensation taking place in the mesopores. The Type V isotherm is related to the Type III isotherm in that the adsorbent-adsorbent interaction is weak, but is obtained with certain porous adsorbents. Finally the Type VI isotherm, in which the sharpness of the steps depends on the system and the temperature, represents stepwise multiplayer adsorption on a uniform non-porous surface.

b. Hysterisis loop

Isotherms of type IV and V above both have what is known as a hysteresis loop. This occurs when the isotherm is irreversible (i.e. The desorption isotherm does not retrace the adsorption isotherm but rather lies above it over a range of relative pressure before eventually rejoining the adsorption isotherms).
Hysterisis loops can take different shapes according to the properties of the adsorbate and IUPAC has distinguished four main categories (H1-H4) as outlined below in figure 2.11.

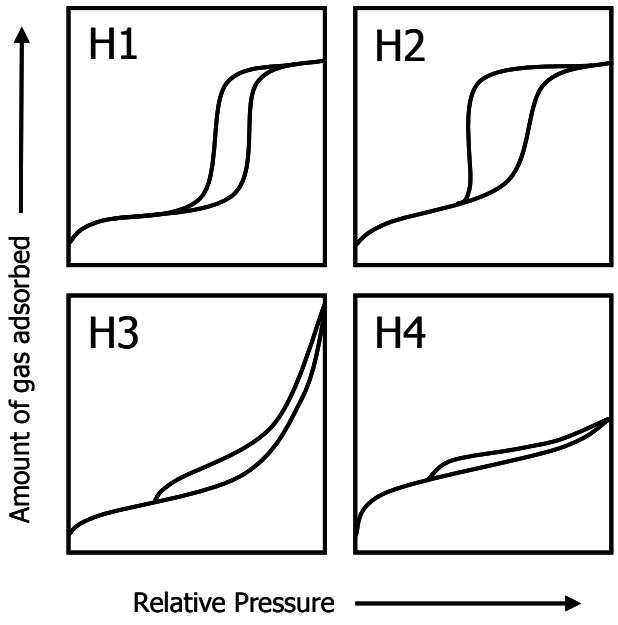

Figure 2.11: The different types of hysteresis loop. Type H1 is often associated with porous materials with narrow pore size distributions; Type H2 is attributed to a difference between condensation and evaporation processes occurring in pores with narrow necks and wide bodies; H3 is observed with aggregates of plate-like particles giving rise to slit-shaped pores; Type H4 loop is often associated with narrow slit-like pores.

Hysteresis appearing in the multilayer range of physisorption isotherms and is usually associated with capillary condensation in mesoporous structures. The observed hysteresis may be the result of two basic mechanisms, namely, "the single pore mechanism" and "the network mechanism".

In "the single pore mechanism", a metastable phase may persist beyond the vapour liquid coexistence pressure during the adsorption and desorption processes where a vapour phase may be present at pressure above the condensation pressure, and a liquid phase below the condensation pressure.

The second mechanism is related to the topology of the pore network. During the adsorption process, the vapours needed to fill the pore can be transported either through the liquid or through the vapour phases. However, during the desorption process, the desorbed vapours must be transported to outside only through the vapour phase. Vaporization therefore occurs only in pores connected to the bulk vapour phase, not in pores surrounded by other liquid filled pores. Once vaporization has occurred in some of the pores near the external surface, the adjacent pores now have contact with the vapour phases, and will vaporize when it is thermodynamically favourable. As a result, clusters of vapor-filled pores grow from the surface until enough pores are opened.

c. Surface area and pore size analysis

All the surface areas presented in this work were calculated using the technique developed by Brunauer, Emmett and Teller (BET) [6]. Using this technique the BET isotherm (Equation 2.1) is applied to the adsorption data as follows.

$$\frac{V}{V_m} = \frac{cz}{(1-z)\{1-(1-c)z\}} \qquad \text{Equation 2.1}$$

Where z is the relative pressure (P/P_0,), V is the volume of gas adsorbed, V_m is the volume of gas absorbed corresponding to monolayer coverage and c is a constant.

This can then be rearranged to give the linear relationship:

$$\frac{P}{V(P_0 - P)} = \frac{1}{V_m c} + \frac{(c-1)P}{V_m C P_0} \qquad \text{Equation 2.2}$$

From this linear relationship it is possible to calculate the volume of gas required for monolayer coverage by plotting the left-hand side of equation 2.2 as a function such that:

$$\text{Intercept} = \frac{1}{V_m c}$$

$$\text{Slope} = \frac{(c-1)}{V_m c}$$

Hence the surface area of the solid can be calculated from the volume of gas required for monolayer coverage and the molecular area of the molecule:

$$SurfaceArea = \frac{V_m L a_m}{22.4 \times 10^{-3}} \qquad \text{Equation 2.3}$$

The BET model of adsorption assumes that all surface sites are equivalent and can accommodate only one atom, the ability of a molecule to adsorb at a given site is independent of the occupation of neighbouring sites, the rate of adsorption is equal to the desorption rate and that the initial adsorbed layer can act as a substrate for further adsorption. Because of these assumptions the BET isotherm is not accurate for very low or high pressures (where coverage is assumed to continue to infinity) and as such surface area results calculated from this method are commonly obtained for values of P/P_0 between 0.08 and 0.35.

It is also possible to obtain pore size distributions from adsorption data and the method favoured in this thesis was based on the technique first developed by (Barrett, Joyner and Halenda) BJH [7]. To understand this method first we must consider a system of open ended, cylindrical pores such that all pores of equal radius can be considered to respond in the same manner to changes in relative pressure of the adsorbate. If we assume that when the relative pressure (P/P_0) equals 1 all the pores will be filled with liquid. The largest pore will have a radius of r_{p1}. On the pore walls there will be an absorbed layer of molecules with a statistical thickness of t_1 and within this adsorbed layer is the inner capillary which has a radius of r_c from which evaporation will occur as the relative pressure is lowered.

Under these conditions the relationship between the pore volume V_{p1} and capillary volume V_{c1} can be specified as:

$$V_{p1} = V_{c1}\frac{r_{c1}^2}{r_{c1}^2} \qquad \text{Equation 2.4}$$

This relationship has no practical use however as V_{c1} is unknown. In order to obtain useful values from this principle we must consider lowering $(P/P_0)_1$ to some lower value $(P/P_0)_2$. This lowering of the relative pressure will result in a reduction in the volume of gas adsorbed which will correspond to the evaporation of the inner capillary from the largest pores and also some reduction in the statistical thickness of the adsorbed layer by the amount, Δt_1. Thus equation 2.1 to be rewritten as:

$$V_{p1} = R_1 \Delta V_1 \qquad \text{Equation 2.5}$$

Where ΔV_1 is the observed volume of gas desorbed and $R_1 = \dfrac{r_{p1}^2}{(r_{c1} + \Delta t_1)^2}$

This calculation becomes further complicated when trying to evaluate the volume of the second pore by a further reduction in the relative pressure from $(P/P_o)_2$ to $(P/P_o)_3$. The corresponding volume of liquid desorbed will now not only include the capillary condensate of the second pore and the thinning of the statistical thickness of this pore but also a further reduction in the statistical thickness of the first pore. If we designate this volume desorbed by the thinning as $V_{\Delta t_2}$ then:

$$V_{p2} = R_2(\Delta V_2 - V_{\Delta t_2}) \qquad \text{Equation 2.6}$$

Where $R_2 = \dfrac{r_{p2}^2}{(r_{c2} + \Delta t_2)^2}$

$V_{\Delta t_2}$ can then be calculated by the expression:

$$V_{\Delta t_2} = \Delta t_2 A c_1 \qquad \text{Equation 2.7}$$

Where Ac_1 is the average area from which the physically adsorbed gas is desorbed which can be generalized so as to represent any of the desorption steps:

$$V_{\Delta t_n} = \Delta t_n \sum_{j=1}^{n-1} Ac_j \qquad \text{Equation 2.8}$$

This equation represents the summation of the average area of unfilled pores down to but not including the pore that was emptied in the nth desorption and by inserting this into a generalised form of equation 2.6 yields the equation:

$$V_{pn} = R_n \Delta V_n - R_n \Delta t_n \sum_{j=1}^{n-1} Ac_j \qquad \text{Equation 2.9}$$

This equation is still unsatisfactory however as Ac_j is not constant for any one set of pores but varies with each subsequent change in relative pressure. The pore area is a constant however and can be calculated from its volume as follows:

$$A_c = A_p \frac{(\bar{r}_p - t_{\bar{r}})}{\bar{r}_p} \qquad \text{Equation 2.10}$$

Where $\bar{r}_p$ is the average radius of all the pores emptied during a relative pressure decrement and $t_{\bar{r}}$ is the thickness of the physically adsorbed layer at the corresponding value of P/P_0.

Thus equation 2.9 can be rewritten as:

$$V_{pn} = R_n \Delta V_n - R_n \Delta t_n \sum_{j=1}^{n-1} b_j A_{pj} \qquad \text{Equation 2.11}$$

Where $b = \frac{(\bar{r}_p - t_{\bar{r}})}{\bar{r}_p}$

This equation forms the model for the BJH pore size analysis. It is possible to calculate rk from the relative pressure (P/P0) by the classical Kelvin equation:

$$\ln P / P_0 = \frac{-2\sigma V}{r_c RT} \qquad \text{Equation 2.12}$$

Where σ is the surface tension of the adsorbate (in our case liquid nitrogen), V is the molar volume of adsorbate, R is the gas constant and T is the absolute temperature. As the BJH model is based on a cylindrical pore system errors begin to creep in when considering spherically based pore systems.

2.5 Powder X-ray Diffraction

Powder x-ray diffraction is routinely used to study crystalline solid state materials. It differs from single crystal x-ray diffraction in that the beam strikes a finely powdered sample, which ideally contains crystals, arranged randomly. The lattice planes of the crystals diffract the x-ray beam. Those planes oriented at the correct angle (Bragg angle 2θ) result in constructive interference of the x-ray beam providing a signal. The powder x-ray patterns, that are recorded, can be interpreted by using the Bragg equation $n\lambda=2d\sin\theta$. Where λ is the wavelength of the incident beam and d is the lattice spacing. Commonly a Cu $K_{\alpha 1}$ radiation source is used (λ=1.5406 Å) and detection of the scattered x-rays carried out by a scintillation counter. With such a setup the scattered x-rays result in Bragg reflections at wide angles (10-90°) for crystalline materials.

The form of the diffraction pattern is determined by the lattice type, crystal class, unit cell parameters and the distribution and types of the various atoms and molecules in the unit cell. As a result of this nearly all crystalline solids have a unique powder X-ray diffraction pattern in terms of both the position and intensity of the observed diffraction peaks. As such powder X-ray diffraction is a very powerful technique to determine which materials are present in any crystalline inorganic material.

Instrumentation

Data was collected using a Siemens D5000 diffractometer, employing CuK_{α} (1.54 Å). The monochromatic x-ray beam was then collimated through an aperture diaphragm and directed onto the sample, mounted flush in a recessed aluminium or plastic holder. Diffracted x-rays were detected by a standard scintillation counter. The sample goniometer was rotated at a constant angular velocity and the detector moved at twice this velocity to ensure the diffraction angle, 2θ. In all cases data was collected for values of 2θ between 10 - 80° using a scan rate of 12° min^{-1}.

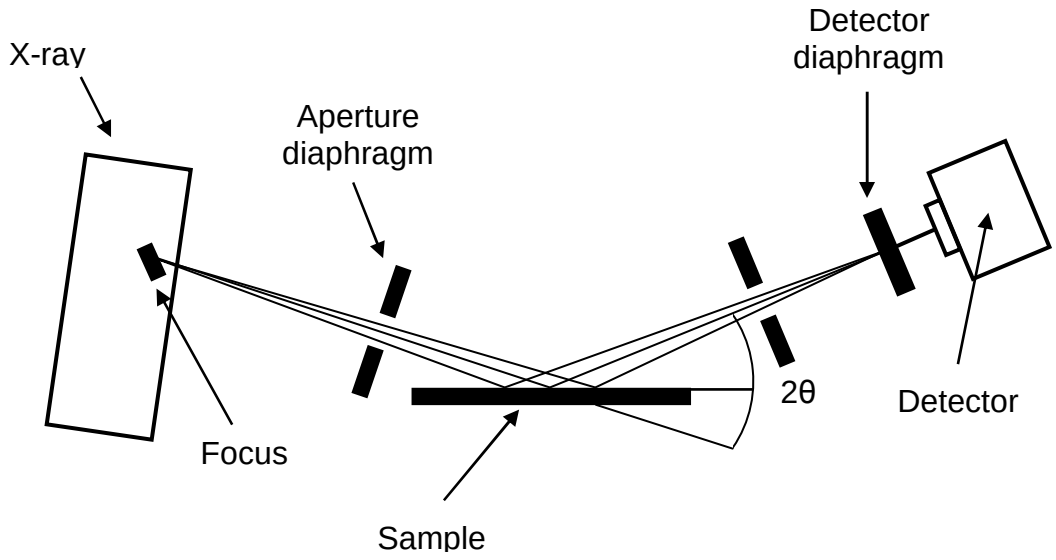

Figure 2.12: A Schematic representation of the Siemens D5000 diffractometer.

2.6 References

(1) Hurd, A. J.; Brinker, C. J., Sol-gel film formation by dip coating. *Materials Research Society Symposium Proceedings* **1990,** 180, (Better Ceram. Chem. 4), 575-81.

(2) Levich, B.; Landau, L., Dragging of a liquid by a moving plate. *Acta Physicochim* **1942,** 17, (42).

(3) Sing, K., The use of nitrogen adsorption for the characterization of porous materials. *Colloids and Surfaces, A: Physicochemical and Engineering Aspects* **2001,** 187-188, 3-9.

(4) Sing, K. S. W., The use of gas adsorption for the characterization of porous solids. *Int. Conf. Fundam. Adsorpt., 3rd* **1991**, 69-83.

(5) Brunauer, S.; Deming, L. S.; Deming, W. E.; Teller, E., A theory of the van der Waals adsorption of gases. *Journal of the American Chemical Society* **1940,** 62, 1723-32.

(6) Brunauer, S.; Emmett, P. H.; Teller, E., Adsorption of gases in multimolecular layers. *Journal of the American Chemical Society* **1938,** 60, 309-19.

(7) Barrett, E. P.; Joyner, L. G.; Halenda, P. P., The determination of pore volume and area distributions in porous substances. I. Computations from nitrogen isotherms. *Journal of the American Chemical Society* **1951,** 73, 373-80.

(8) Williams, D. B.; Carter, B., Transmission Electron Microscopy – A Textbook for Materials Science, *Published by Springer,* **1996**.

Chapter 3

Contents page

3D MACROPOROUS METAL SILICATE MATERIALS

CHAPTER 3 – 3D MACROPOROUS METAL SILICATE MATERIALS

3.1 Introduction

Periodic macroporous materials are of considerable interest for adsorption, separation, catalysis and molecular hosting of organic, inorganic and biological systems requiring a periodicity > 50 nm[1-8]. The sub-micrometer structure further allows Bragg diffraction of visible light, producing vivid optical colour shifts that are potentially suitable for pigment applications. The more ordered systems might also find applications in optoelectronics[9, 10].

Three dimensionally ordered macroporous materials with periodicities in the sub micrometer size range are more difficult to fabricate than their microporous (< 2 nm) or mesoporous analogues (2- 50 nm) [11]. Techniques such as emulsion templating, rod-coil block copolymer self-assembly and solvent evaporation have resulted in foam like materials with minimal structural order [12-15]. The most successful route employs ordered arrays of sub micrometer spheres (colloidal crystals) as templates [16]. Infiltration of the interstitial voids with materials, using chemical vapour deposition (CVD), electrodeposition, or sol-gel deposition, followed by template removal leaves a highly ordered interconnected porous spheroid matrix [17]. The resultant macroporous material replicates point, line and planar defects present in the original packed spheres with further defects arising from incomplete void filling and cracking during template removal [18]. Defects in the colloidal crystal can be minimised by using monodisperse colloidal spheres and tightly controlled slow, gravity dependent packing mechanisms. However, defects arising during material infiltration and template burn-off are more difficult to control.

Macroporous silica, titania and alumina materials fabricated via sol-gel templating from collidal crystal architectures have been widely reported [19, 20]. Recently, Becheger et al described the consecutive deposition of ZrO_2, TiO_2 and Al_2O_3 to form macroporous oxides with multilayered pore walls [21]. However, the incorporation of mixed metal oxide infiltrates has not yet been achieved. Mixed metal oxide macroporous composites of silicon/aluminium, silicon/titanium and silicon/tin are of potential interest for catalytic and ion exchange applications [22]. Porous titanosilicates have found application as epoxidation catalysts of long chain olefins and, in more recent studies, as photocatalysts for the decomposition of organic matter [8, 23, 24]. The band gap structure of titania (rutile

phase, band-gap 3.2 Ev), makes it an effective absorber of UV light, producing electron hole pairs for the oxidation of adsorbed donor molecules and the reduction of adsorbed acceptor molecules respectively [25]. Porous aluminosilicate frameworks have found a niche application as solid-acid catalysts. Tetrahedrally co-ordinated aluminium ions, at the pore walls, function as Bronsted acid sites that are ideal for catalytic cracking of fuel oils [26, 27]. In addition, macroporous alumina membranes have demonstrated strong potential for the selective oxidation of alkane gasses [28].

Achieving high heteroatom aluminium, titanium and tin loadings in silica, in addition to maintaining an ordered porosity has proven difficult. The problem arises from incompatibility between the hydrolysis rates of alkoxides of silicon to those of aluminium or titanium. The faster hydrolysing metal alkoxide species favour self condensation instead of reaction with the silicon alkoxide, resulting in precipitation of metal rich compounds. In particular, titanium loading in mesoporous silica films is limited to 2% with direct alkoxide sol-gel synthesis [29]. Loadings of 20% (5:1 Si:Ti) have been obtained through selective complexation of titanium alkoxide species to reduce the active sites for hydrolysis [24]. However, the presence of complexing species also restricts the condensation process resulting in films with poor mechanical and thermal stability. The mixed oxide films are often further subject to heterometal leaching at high temperatures. To-date, macroporous silica films with high (> 20%) loadings of aluminium, titanium or tin have not been reported.

The work reported in this chapter describes a facile silicon alkoxide prehydrolysis technique that allows the direct formation of highly ordered mixed metal oxide macroporous materials with Si:Al ratios of 2:1, Si:Ti ratios of 1:1 and Si:Sn ratios of 1:1 respectively. The solutions allow excellent infiltration of close packed packed arrays of polystyrene spheres completely filling the interstitial voids. Both the aluminosilicate and titanosilicate macroporous metal oxides are defect free over large areas (2500 μm^2) and show no evidence of metal leaching during the template removal process. Homogeneity of the mixed oxide binders is evidenced by FT-IR, X-ray diffraction and EDX analysis. In contrast the tin silicate macroporous films exhibited a large number of defects which are seen to increase with increasing heterometal loading indicating that mechanical instability results from phase separation in the mixed metal material.

3.2 Experimental

Experimental details are presented in four sections, the first three sections give a general procedure for fabricating macroporous mixed metal oxides. The fourth section describes the different characterisation methods that were used in this study.

3.2.1 Assembly of the colloidal templates

The colloidal crystal templates were assembled by a simple sedimentation method. Initially microscope slides were precleaned by sequential sonication in water, acetone, isopropyl alcohol and chloroform before a Teflon ring (Internal diameter - 10 mm, Ext. dia. - 20 mm, thickness - 10 mm) was attached by double sided tape. 0.5 ml of a monodisperse suspension of PMMA spheres diluted with water to 1-wt % was confined within the Teflon ring. The water was allowed to evaporate in a fridge at 3 °C over about 5 days. After all the water had evaporated the Teflon ring was removed exposing a circular iridescent packed array of polystyrene spheres on the substrate. This approach formed uniform films of 40 μm thickness.

The surface area analyser required larger quantities of materials than were typically synthesised using the standard preparation and as such a scaled up fabrication was required. In this case 8 ml of 1 % wt pmma sphere solution was confined within a 10 cm internal dia. 11 cm ext. dia. and 1 cm thick Teflon ring which had been adhered to a 10 * 10 cm glass slide by double sided tape. This was then dipped into a sol as described previously however in order to get a sufficient amount of sol it was necessary to scale up the quantity of reactants used ten fold. This was then allowed to dry for 48 hours before the samples was scraped from the glass slide and heated in an oven to 350 °C in air at a rate of 2 °C min^{-1}. This temperature was maintained for 30 minutes before slowly cooling over 16 hours.

3.2.2 Preparation of Sol-Gel Precursors

Aluminosilicate, titanosilicate and tin silicate sol-gel precursor solutions were prepared by the pre-hydrolysis method developed by Ryan et al for the production of mesoporous thin-films [30]. Tetraethyl orthosilicate (TEOS, Aldrich, 10 g), ethanol (5.4 g) and HCL (0.8 ml, 0.1 M) were mixed and stirred at 37 °C for 10 mins to prehyrolyse the silica

precursor. The solution was cooled in an ice bath prior to the respective addition of aluminium in the form of aluminium tri-*sec*-butoxide, tin in the form tin (IV) chloride ($SnCl_4$) and titanium in the form of titanium tetra-ethoxide ($Ti(OC_2H_5)_4$, Aldrich) followed by H_20 (1 ml). Finally the mixture was allowed to condense for 20 hours at room temperature.

3.2.3 Fabrication of macroporous films by dip coating.

The crystalline template adhered to the glass substrate was immersed vertically into the sol, at a rate of 150 mm min^{-1}, before immediately withdrawing at 50 mm min^{-1}. Due to capillary forces the sol infiltrates the interstitial voids of the template. The sample was dried at 50 °C for 1 hour allowing gelation of the sol. Finally the template was removed by heating the sample to 350 °C in air at a rate of 2 °C min^{-1}. This temperature was maintained for 30 minutes before slowly cooling over 16 hours. This process yields a circular (10 mm dia.) macroporous metal silicate film with a thickness of approximately 40 µm.

3.2.4 Characterisation

A field emission scanning electron microscope (JSM-6500F) was used to study both the morphology and microstructure of the macroporous films. The films were coated with a thin layer of gold (ca ~ 20 nm) prior to both topographical observation and energy dispersive X-ray analysis.

X-ray diffraction (Siemens D5000) using Cu K_α radiation was used to study the microstructure of both macroporous films and powdered titanosilicate and aluminosilicate samples.

An Olympus BX51 microscope at 10 times magnification with an Ocean Optics 'USB 2000' spectrometer was used to collect the reflectance data. The microscope was equipped with a 100W halogen bulb. At 10 times magnification the spot size is 1 mm but the spectra is taken from an area with a diameter of about 50 µm.

FTIR absorption spectra were recorded on a Mattson Satellite FT-IR spectrometer fitted with a Specac Golden Gate Single Reflection ATR sampling platform.

Nitrogen absorption/desorption isotherm was obtained using a Gemini 2375 BET surface area analyser.

3.3 Results

Ordered metal silicate macroporous films were prepared by the sol-gel infiltration of monodisperse (365, 356 or 294 nm) close packed spheres. Materials were prepared with a range of heterometals at various loadings. Presented below is a detailed discussion of the surface morphology of the materials which was investigated by scanning electron microscopy.

3.3.1 Structure

Figures 3.1a-d, 3.2a-d and 3.3a-f show SEM images of a series of titanosilicate, aluminosilicate and tin silicate macroporous samples respectively with varying heterometal loadings.

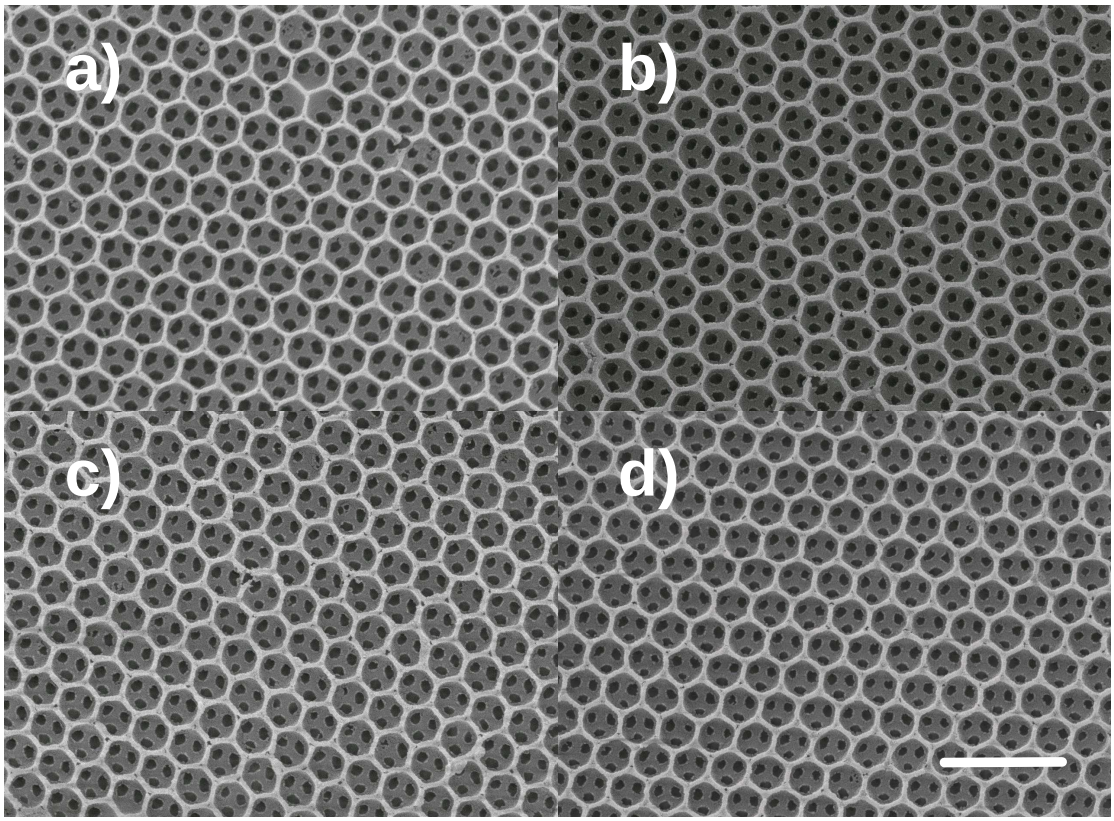

Figure 3.1: SEM image of macroporous titanosilicate materials with Ti:Si atomic ratios of (a) – 1:1, (b) – 1:3, (c) - 1:5, (d) – 1:10. Materials were fabricated from a colloidal crystal template composed of 365 nm PMMA spheres. Scale bar represents 1 µm.

Both the aluminosilicate and titanosilicate samples maintain the hexagonal arrangement of pores in the inverse opals reflecting the close packed ordering of the colloidal crystal template independent of heterometal loading. Uniformity of thickness in the binding walls further evidences the complete filling of the interstitial voids during sol-gel infiltration. It is clear from figures 3.1 and 3.2 that the macrostructure in the alumino- and titanosilicates is unaffected by differences in the heterometal loading, however in the case of the tin silicate materials the hexagonal structure is only maintained when the heterometal loading is at 20 % or less (Figures 3.3d-f), increasing the heterometal loading to 25 % led to a disordered macroporous material which encompassed a very large number of defects. Further increases in the level of tin incorporation led to further degradation of the macrostructure. This is likely a result of phase separation occurring in the sol leading to both tin and silica rich regions which in turn causes a reduction in the mechanical stability of the macrostructure.

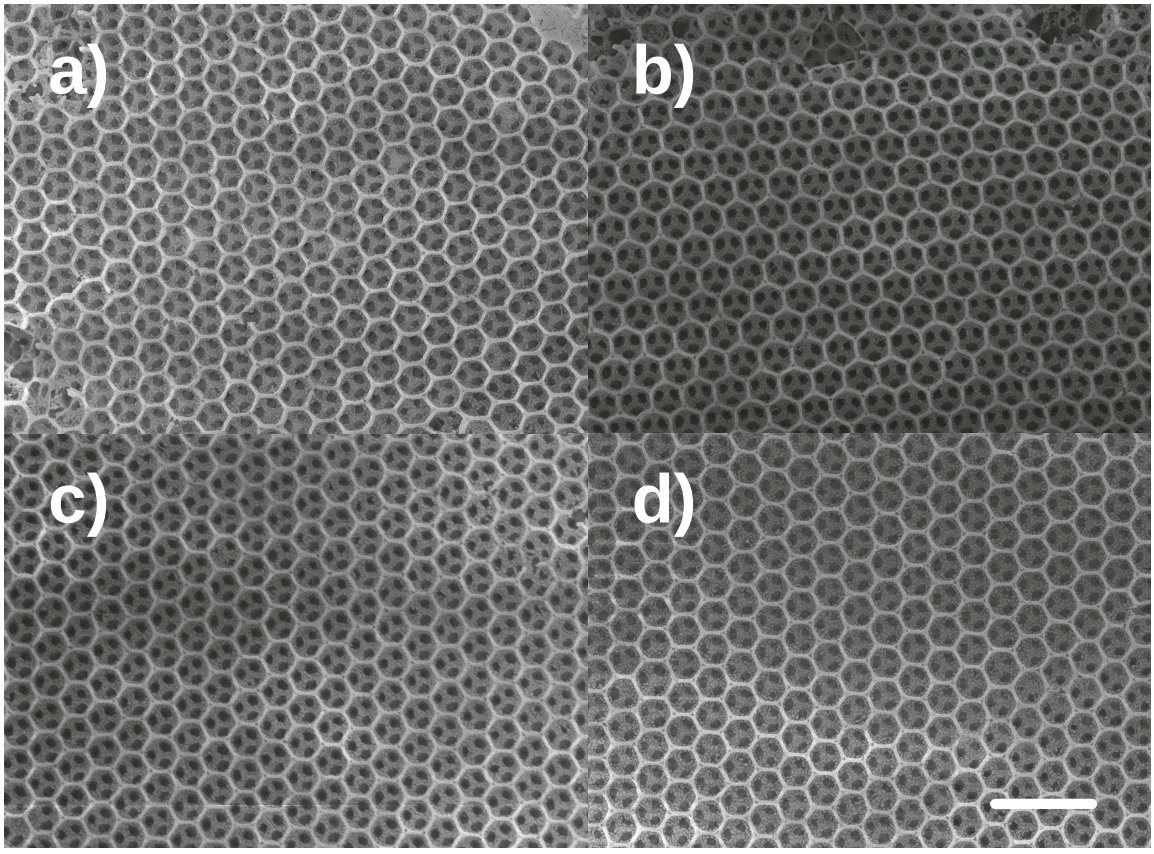

Figure 3.2: SEM image of macroporous aluminosilicate materials with Al:Si atomic ratios of (a) – 1:2, (b) – 1:3, (c) - 1:4, (d) – 1:5. Materials were fabricated from a colloidal crystal template composed of 365 nm PMMA spheres. Scale bar represents 1 µm.

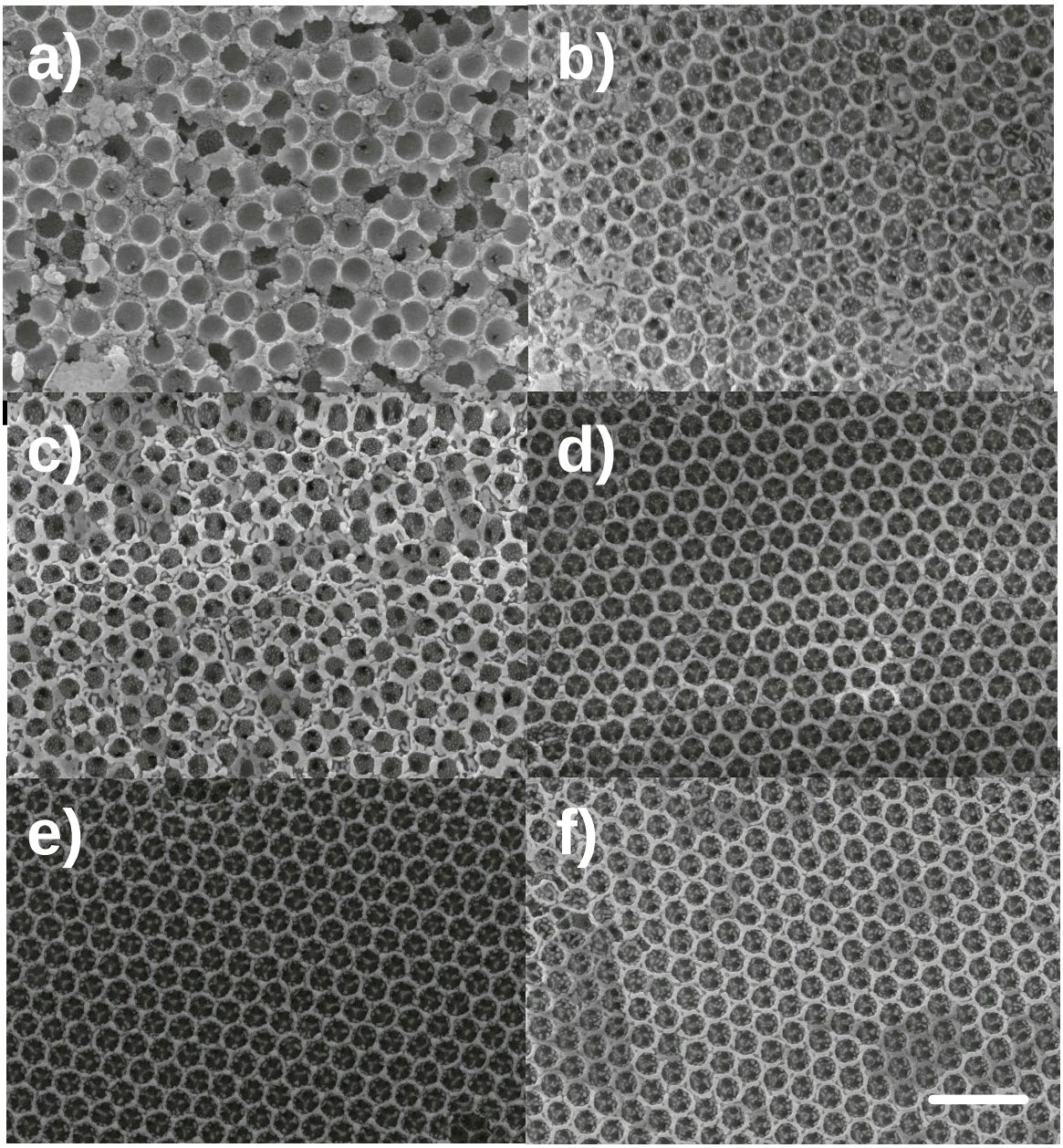

Figure 3.3: **SEM image of macroporous tin silicate materials with Sn:Si atomic ratios of (a) – 1:1, (b) – 1:2, (c) - 1:3, (d) – 1:4, (e) – 1:6, (f) – 1:10. Materials were fabricated from a colloidal crystal template composed of 356 nm PMMA spheres. Scale bar represents 1 μm.**

The pore diameter was calculated for each sample from the SEM images. As the diameter of the template spheres is known this also allows the percentage shrinkage that occurs during calcination to be calculated (Table 3.1), and within experimental error these values were consistent for all the synthesised materials, regardless of composition, heterometal and template sphere size. The average volume shrinkage of the materials was about 20 % which is consistent with that reported for sol-gel processes and results in the films cracking into several large domains from 0.1 mm^2 up to 2 mm^2.

Heterometal	PMMA sphere diameter/ nm	Si/M atomic ratio in the initial sol	Pore diameter / nm	Volume shrinkage %	Error
Al	365 ± 13.7	2	332.3	24.5	5.4
Al	365 ± 13.7	3	337.8	20.7	5.6
Al	365 ± 13.7	4	343	17	5.1
Al	365 ± 13.7	5	345	15.6	4.8
Al	365 ± 13.7	10	342	17.7	5.2
Ti	365 ± 13.7	1	345.4	15.3	6.9
Ti	365 ± 13.7	2	350.8	11.2	5.3
Ti	365 ± 13.7	3	342.8	17.2	4.7
Ti	365 ± 13.7	4	349.2	12.4	4.4
Ti	365 ± 13.7	5	345.7	15	4.4
Ti	365 ± 13.7	10	332.8	24.2	5.3
Sn	356 ± 12.6	4	328	21.8	7.2
Sn	356 ± 12.6	6	326	23.2	5.6
Sn	356 ± 12.6	8	328	21.8	5.1
Sn	356 ± 12.6	10	313	32	4.9
Sn	294 ± 10.4	4	280	13.6	6.1
Sn	294 ± 10.4	6	271	21.7	5.1
Sn	294 ± 10.4	8	278	15.5	5.5
Sn	294 ± 10.4	10	273	19.9	4.2

Table 3.1: Tabulated data showing the average pore size and corresponding % shrinkage for all the synthesised macroporous materials.

Fine scale structure

Figure 3.4 is a further magnified SEM image of a macroporous mixed metal oxide consisting of silica and titania in the ratio of 1:1. The pore diameter is 345.4 ± 12.9 nm with an average wall thickness of 48.9 ± 8.9 nm. The air sphere volume for these inverse opal structures is 74.2%. The image also reveals the complicated interconnected network of air spheres in the macroporous framework. Each large cavity in the surface layer contains three internal windows (diameter 96.4 ± 20.6 nm) to successive layers at the points of contact of the original spheres.

Another interesting feature is the presence of small openings, or spandrels (marked with an arrow in figure 3.4, diameter ~ 5 nm) at the centre of each triangular intersection of three air spheres. The presence of these spandrels indicates that the templating proceeds by a surface templating mechanism where the condensation of the sol-gel precursors occurs primarily on the surface of the spheres thereby blocking the introduction of additional precursors into the interstitial spaces between the spheres. The net result of this is the presence of small vacancies at the centre of each triangular intersection of three air spheres. Alternatively if the precursors do not adhere to the spheres the templating proceeds by a volume templating mechanism in this case the precursors completely fill the void volume between the spheres prior to solidification. In the case of sol-gel derived inverse opals the mechanism by which the templating proceeds is heavily dependant on the degree of wetting of the colloidal crystal template by the sol-gel precursors. If the precursors strongly adhere to the template a surface templating mechanism takes place, resulting in the inverse opal encompassing spandrels[31], whilst fluid precursors that do not adhere to the template result in a volume templating mechanism. Sol-gel techniques most commonly proceed via a surface templated mechanism whilst electrochemical routes always proceed by a volume templated mechanism which is evidenced by the absence of spandrels in opals prepared in this manner.

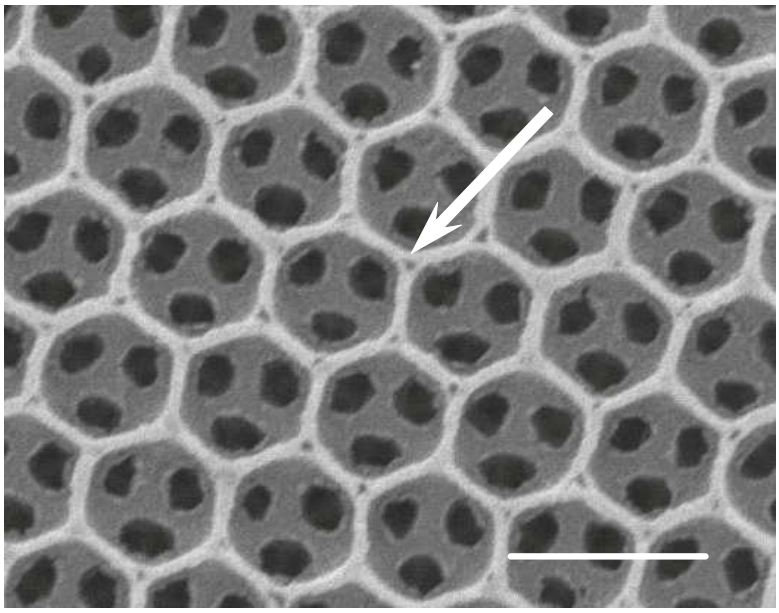

Figure 3.4: **High resolution SEM image of a macroporous titanosilicate sample (Si:Ti, 1:1). The sample was fabricated from a colloidal crystal template composed of 365 nm PMMA spheres. Scale bar represents 100 nm.**

Defects

Materials fabricated by colloidal crystal templating typically encompass a large number a defects. Either thermal shock and shrinkage during calcinations or packing irregularities in the close packed template are the main causes of defects in the final material. Packing irregularities are replicated in the final material whilst thermal shock and shrinkage typically results in tears and cracks appearing in the material. Figures 3.5 (a-d) show the most common defects exhibited by these materials, whilst figure 3.6(a-c) shows some packing irregularities in a colloidal crystal template which form the basis of the defects in the final material.

Figure 3.5a shows a defect that occurs when a small fraction of the original opal template adopts body centred packing as opposed to the favoured close packing. Regions exhibiting body centred packing are uncommon but as the energy difference between the close packed and body centred structures is quite small these small areas occasionally nucleate by chance (Figure 3.6a). Figure 3.5b shows a point defect, these defects are more common and are once again caused by imperfections in the original colloidal crystal template resulting from the absence of a sphere in the original template (Figure 3.6b). Figure 3.5c shows a large rent in the material. This large tear occurs due to shrinkage occurring during the calcination step of the fabrication. Finally figure 3.5d shows a line

defect which in a similar way to the point defect is caused by the absence of a row of spheres in the original colloidal crystal (Figure 3.6c).

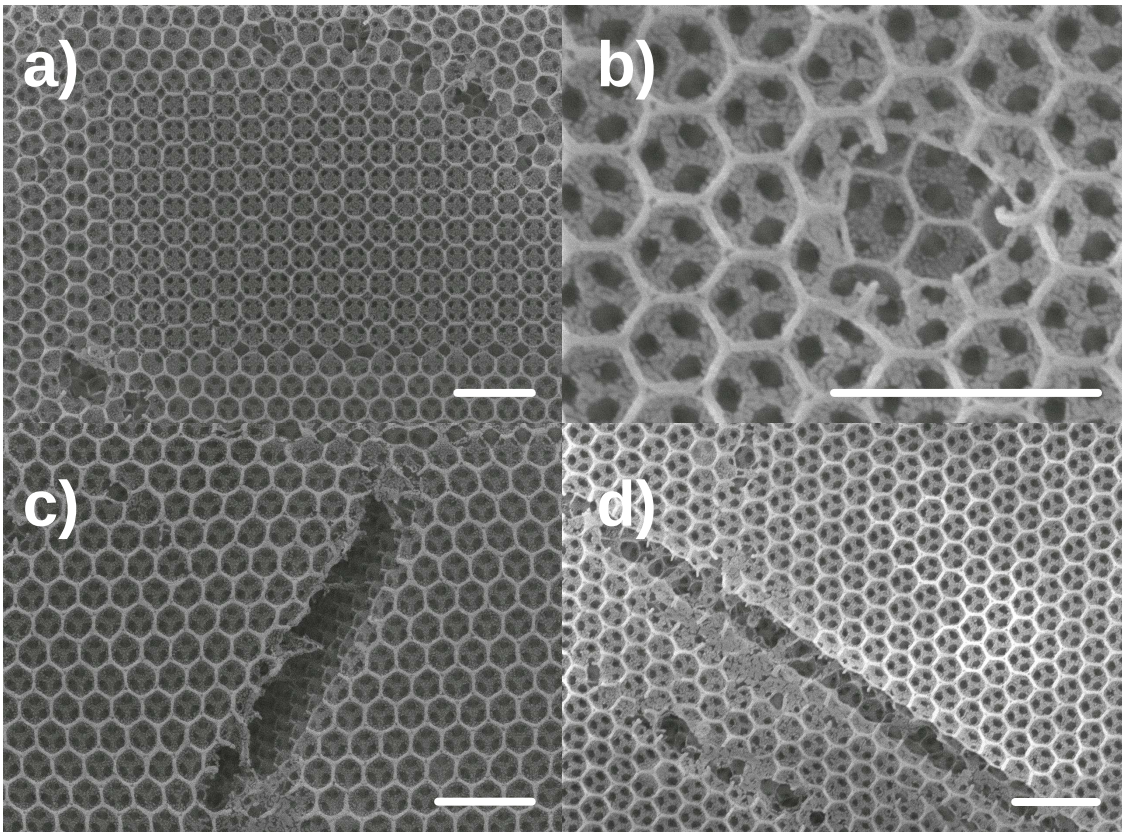

Figure 3.5: **(a) SEM image of a point defect in a macroporous aluminosilicate sample (Si:Al, 5:1), (b) SEM image of a region with body centred packing in a macroporous aluminosilicate sample (Si:Al, 4:1), (c) SEM image of a tear in a macroporous titanosilicate sample (Si:Ti, 3:1), (d) SEM image of a line defect in a macroporous aluminosilicate sample (Si:Al, 4:1). All samples were fabricated from colloidal crystal templates composed of 365 nm PMMA spheres. Scale bars represent 1 µm.**

The packing of microspheres by sedimentation involves a strong coupling of several processes such as gravitational settling, Brownian motion and nucleation and growth, as such it is possible to minimise the defects caused by imperfections in the initial template by tightly controlling several factors such as sphere density and size as well as the rate of sedimentation. The simplest technique to reduce imperfections in the initial crystal is to carry out the sedimentation at very low temperatures (~3 °C) in order to minimise the effect Brownian motion has on the colloids. On the other hand defects arising from shrinkage are typically much more difficult to control but can be kept to a minimum by using slower heating rates during the calcination step.

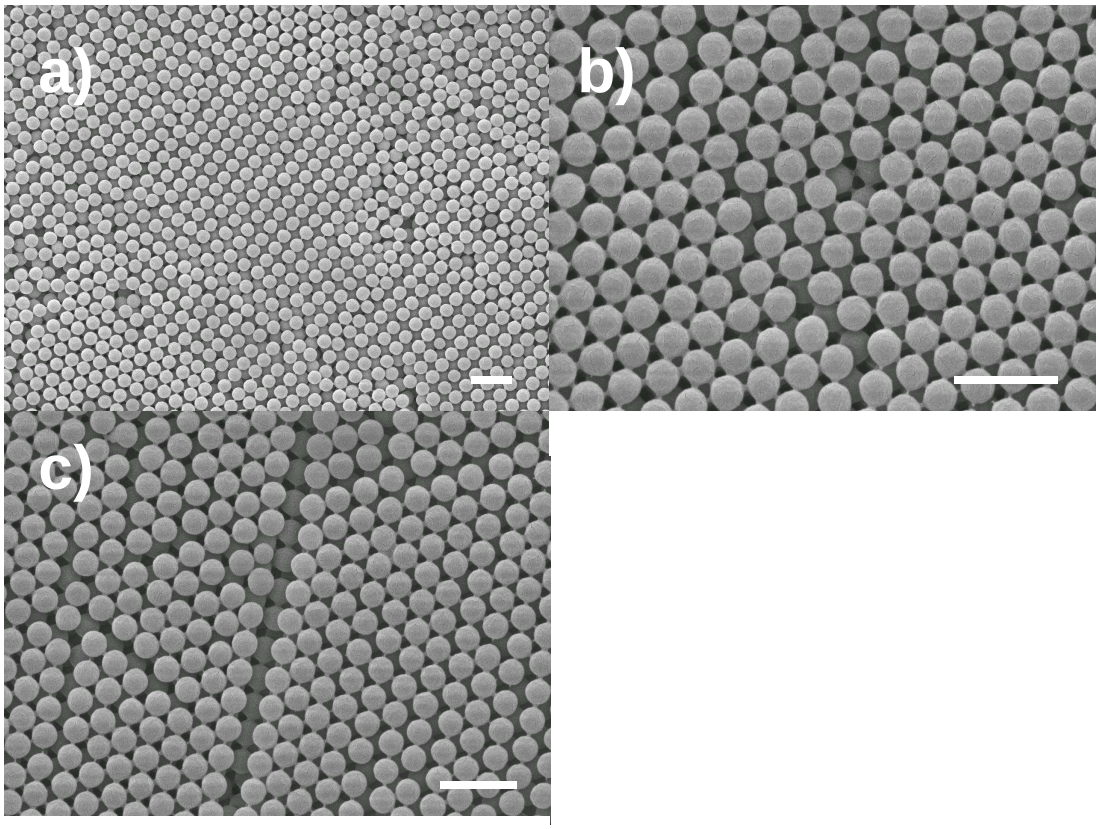

Figure 3.6: **SEM images of imperfections in a colloidal crystal template fabricated by gravimetric sedimentation of 365 nm PMMA spheres (a) cubic close packed region, (b) point defect, (c) line defect. Scale bars represent 1 µm.**

Analysis of the mixed oxide inverse opals at lower magnification reveals regular grain boundaries permeating the particles. Figure 3.7 is an SEM image illustrating the polycrystalline distribution of the hexagonal domains in the close packed structure of macroporous (1:1 Ti:Si) titanosilicate. The domains are randomly orientated with respect to one another in a striped morphology. These grain boundaries are probably present in the original template and are transferred to the final material during the templating process.

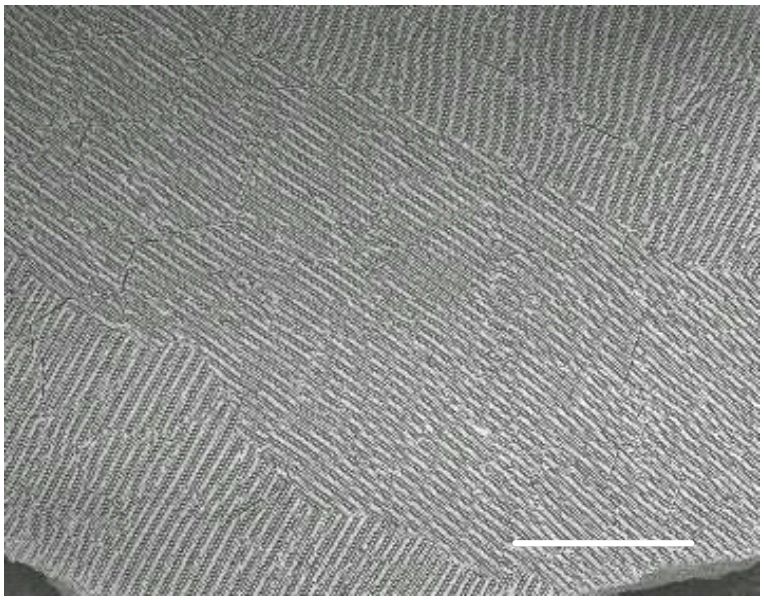

Figure 3.7: SEM image showing the polycrystalline nature of a titanosilicate macroporous film, (Si:Ti, 1:1). The sample was fabricated from a colloidal crystal template composed of 365 nm PMMA spheres. Scale bar represents 50 µm.

In the case of the aluminosilicate and titanosilicate materials, defects were limited to about one per 150 spheres and were further minimized using slow (several weeks) gravity sediment templates obtained at 3 °C. However the tin silicate materials typically encompassed a larger number of defects many of which were not transferred from the original template and this once again can be attributed to sol separation resulting in the mechanical instability of the tin analogues. On average, both the titanosilicate and aluminosilicate films were found to be defect free in large domains (50×50 μm^2) regardless of elemental composition using slow gravity deposited templates. The even distribution of material at pore walls and smooth topography evidences the uniform deposition of mixed oxide sol-gel precursors during fabrication.

3.3.2 Thickness control

It has often been suggested that one of the disadvantages that chemical routes towards macroporous materials have over electrochemical methods is the inability to control the thickness of the final material. Furthermore for these materials to have any potential as special effect pigments it is necessary that the flakes are no more than 4-5 microns in thickness.

The samples described in the previous section were typically prepared with a thickness of 30 μm (90 layers) by partially filling a 40 μm thick artificial opal template from the substrate with the sol-gel solution.

In section 2.2, pg 35 it was stated that the thickness of a film deposited onto a flat substrate during a sol gel dip-coating process can be evaluated using the following equation originally derived by Landau and Levich:

$$h_0 = \frac{0.94(\eta U_0)^{2/3}}{\gamma_{LV}^{1/6}(\rho g)^{1/2}} \qquad \text{Equation 2.1}$$

where η is the liquid viscosity, U_0 is the withdrawal speed, γ_{LV} is the liquid vapour surface tension, ρ is the liquid density and g is the acceleration by gravity.

It is obvious from the equation that two factors that are crucial to the thickness of the deposited film and these are the substrate withdrawal speed (U_0) and the viscosity of the fluid mixture (η). This equation describes the forces governing the deposition of films onto planar substrates, whilst our system involves the deposition of a films onto a colloidal crystal adhered onto a glass substrate. The infiltration of the colloidal crystal is governed by capillary forces and as such the thickness of the final coating will depend on a variety of factors, namely the sol viscosity, the substrate withdrawal speed and the colloidal crystal template.

With this in mind the following section describes three approaches to gain some control over the thickness of these metal silicate macroporous materials, namely by:

a) Varying the concentration of precursors in the sol

b) Varying the substrate withdrawal speed

c) Varying the thickness of the colloidal crystal template

a. Increased sol dilutions

A concentrated aluminosilicate sol (6:1, Si:Al) was synthesised and diluted with varying quantities of ethanol. This reduced the concentration of both the TeOS and Aluminium tri-sec butoxide in the initial sol and served to reduce the viscosity of the solution. Table 3.2 shows the composition of each sol.

EtOH / wt %	TeOS/ wt %	Al-sec-but/ wt %	H_2O/ wt %	HCl/ wt %
29.3	53.0	10.5	2.1	5.1
57.6	31.8	6.3	1.3	3.1
74.6	19.1	3.8	0.8	1.8
84.7	11.5	2.3	0.5	1.1
90.8	6.9	1.4	0.3	0.7
94.5	4.1	0.8	0.2	0.4

Table 3.2: The chemical makeup of the various sol dilutions used in the study. Values are expressed as wt % with respect to all the components in each mixture.

A 40 μm thick colloidal crystal was dipped into each solution detailed above and withdrawn at a rate of 50 mm min^{-1}. Subsequent calcinations yielded the inverse opal and the thickness of each sample was evaluated via image analysis of 30 cross-sectional SEM images. The results of this study are presented below in figure 3.8 which shows the average flake thickness as a function of the wt % of TeOS in the initial sol gel solution.

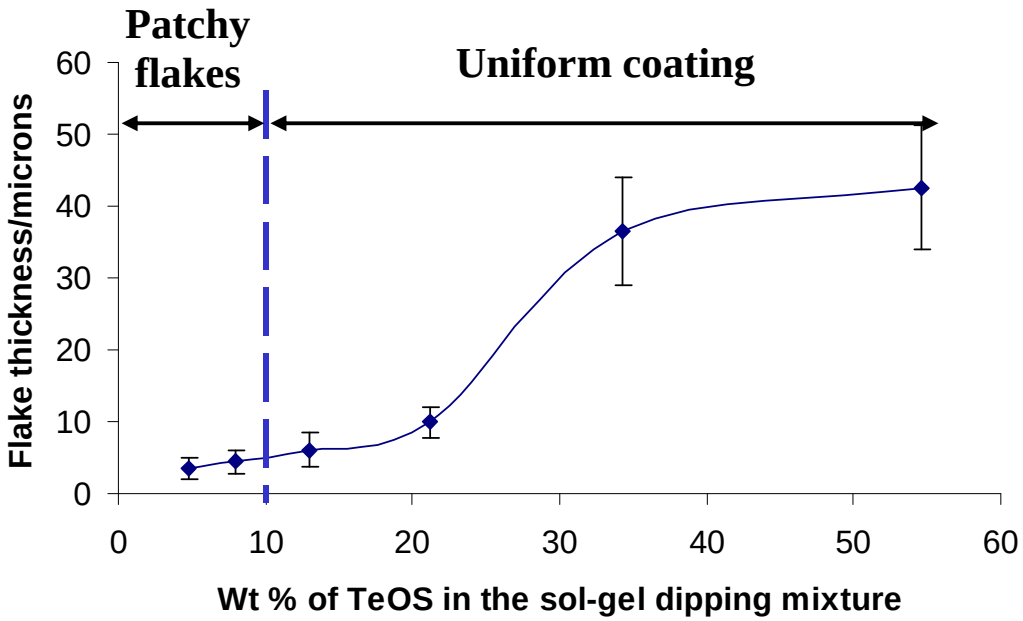

Figure 3.8: **A graph showing the dependency of the flake thickness upon the concentration of silicon alkoxide (TeOS) in an aluminosilicate (5:1 = Si:Al) sol-gel mixture. Materials were fabricated from a colloidal crystal template composed of 365 nm PMMA spheres.**

As expected the results show a pronounced decrease in flake thickness with increasingly diluted sols. Dilution results in sols that are both lower viscosity and have a lower concentration of reaction precursors. Both these factors result in a decrease in flake thickness with increased dilution. Thus by controlling the concentration of the sol it is possible to control the amount of the original colloidal crystal template that is filled. For example, if a 40 μm artificial opal is quarter filled with solution from the substrate excess template removal during calcinations yields a 10 μm film.

This technique is limited to producing materials with a minimum thickness of about 6 μm however as after about 10 wt % TeOS we observe coatings typified by the SEM images presented below (Fig. 3.9). As shown there is now incomplete filling of the voids of the template resulting in the incomplete macroporous coating. The cut off limit for producing uniform coatings is highlighted in the graph above (Fig. 3.8) by the dashed blue line.

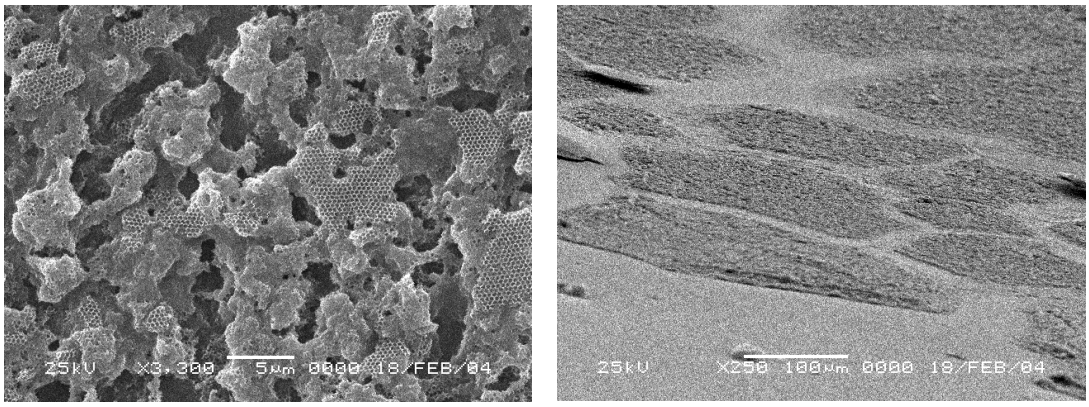

Figure 3.9: SEM images showing the resultant coating that arises from using an over diluted sol. In the case above the sol has a silicon alkoxide (TeOS) concentration of 5.1% by weight. Materials were fabricated from a colloidal crystal template composed of 365 nm PMMA spheres.

b. Varied withdrawal Speed

In a dip-coating process the speed with which a substrate is withdrawn from the solution is also commonly exploited to gain control over the coating thickness. From equation 2.1 it is clear that the relationship between withdrawal rate and coating thickness is counter intuitive with faster withdrawal speeds yielding coatings with thicker films. Physically this occurs because less solution drains away from the substrate.

The table below shows the average flake thickness of a series of materials synthesised using varied withdrawal speeds:

Withdrawal speed/mm min^{-1}	Coating thickness/µm
20	7.3 +/- 1.3
50	10.3 +/- 1.3
100	7.1 +/- 1.0
150	7.8 +/- 2.5

Table 3.3: The dependency of the flake thickness upon the dip withdrawal speed.

The TeOS weight percent in the initial sol was 18.2 so we would expect a thickness of about 8 µm (Figure 3.9) and this is indeed the case. The dip speed appears to have no effect on the thickness of the resultant coating, which can be attributed to the infiltration of the colloidal crystal occurring by capillary forces and undermining the draining mechanism that would normally occur for dip coating process.

c. Varied colloidal crystal template thickness

Finally in attempts to reduce the thickness of the macroporous flakes experiments were undertaken varying the thickness of the initial colloidal crystal template. Once again image analysis was used to evaluate the flake thickness and these results are presented below.

Colloidal crystal template thickness / μm	Coating thickness/μm
8	6.9 +/- 0.9
16	12.4 +/- 1.7
24	9.5 +/- 2.3
32	7.9 +/- 2.7
40	8.7 +/- 1.4

Table 3.4: The dependency of the flake thickness upon the initial template thickness

The sol once again contained 18.2 % TeOS and as such a final flake thickness of about 8 μm would be expected, and this is once again what we see regardless of the thickness of the initial template. This indicates the template thickness has no effect on the final material unless the template is too thin in which case the sol overfills the template resulting in a material that has a solid metal silicate layer on top of the desired macroporous metal silica framework (Figure 3.10).

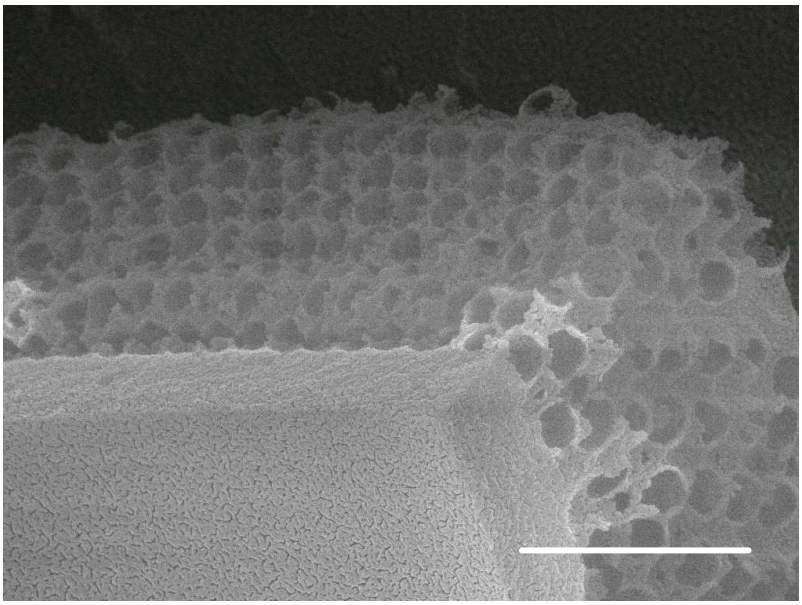

Figure 3.10: SEM image of a macroporous aluminosilicate sample with a solid aluminosilicate layer on top of the macroporous matrix. Sample was

fabricated from a colloidal crystal template composed of 365 nm PMMA spheres. Scale bar represents 1 micron.

3.3.3 Surface area

A nitrogen adsorption/desorption isotherm was obtained using a micromeritics Gemini 2375 surface analyser for a macroporous titanosilicate sample (Fig 3.11). The shape of the isotherm is characteristic of a macroporous sample, at very low pressures a monolayer of nitrogen forms on the surface of the solid. As the limit of monolayer coverage is reached, nitrogen begins to condense and fill the very smallest pores of the sample. As the pressure increases further larger and larger pores are filled. The isotherm below shows a sudden sharp increase in gas absorbed at very high pressure and this corresponds to the filling of the large macropores.

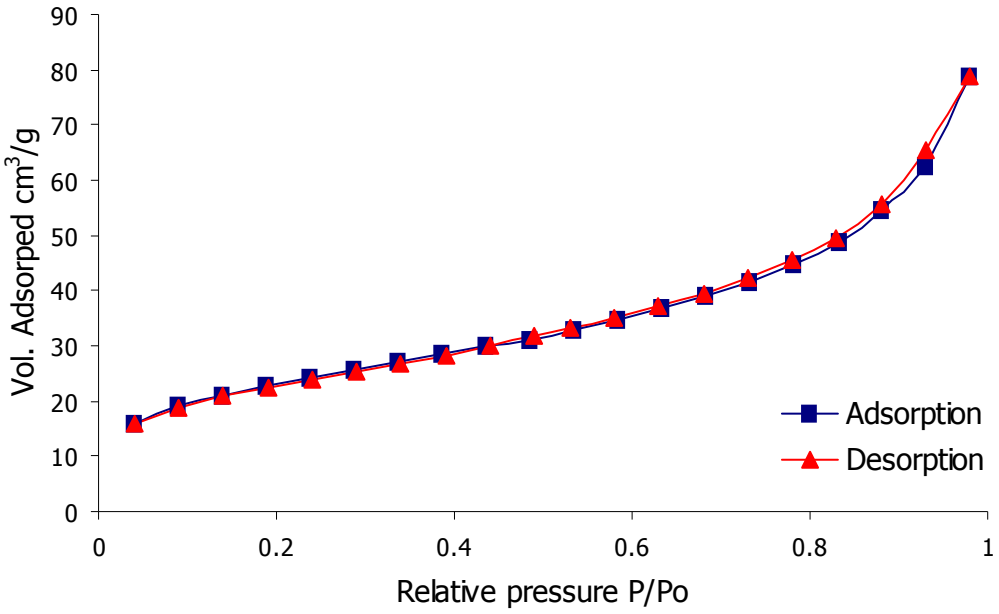

Figure 3.11: Nitrogen adsorption and desorption isotherm for a titanosilicate sample (Si:Ti, 5:1, figure 3.1 c). The inverse opal was fabricated from a colloidal crystal composed of 365 nm spheres which resulted in a macropore size of 346 nm.

The surface area was also measured from the isotherm as 76.9 $m^2 g^{-1}$ using the BET technique. This value is in good agreement with other published values for similar macroporous materials.

3.3.4 Composition

Energy dispersive X-ray Analysis (EDX) was used to quantify the elemental composition of the titanosilicate, tin silicate and aluminosilicate matrices. Figure 3.12 compares the silicon/heterometal atomic ratios of the calcined macroporous material to the ratio in the initial sol, the dotted line is the ideal case where the exact ratio in the initial sol is maintained in the final material and in all three cases a tight fitting linear relationship is obtained indicating that the ratio of metal to silicon is preserved throughout the deposition and calcinations process.

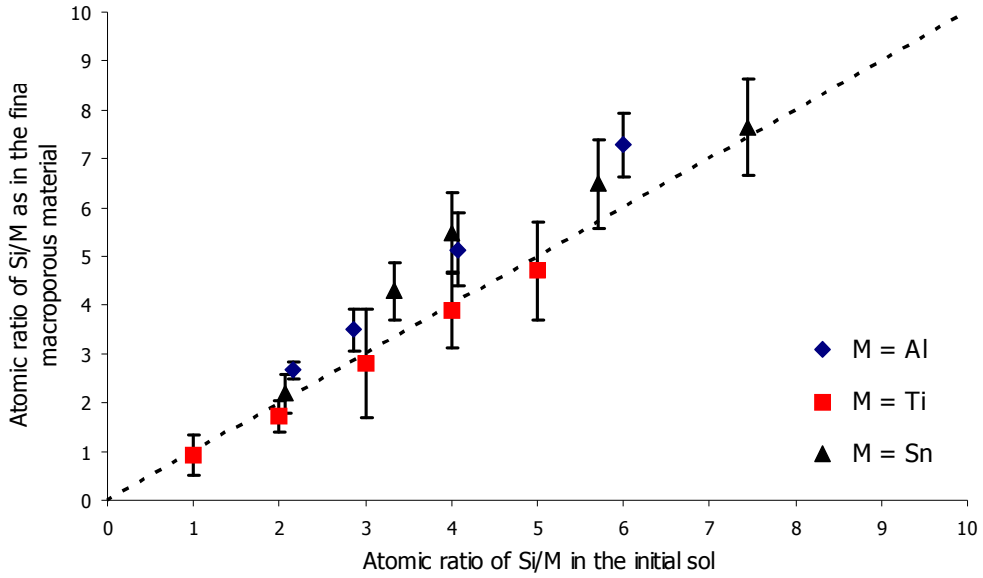

Figure 3.12: Comparison of the Si/M atomic ratio in the macroporous materials to initial sol concentration for M = Al, Sn and Ti.

Sol-gel routes towards mixed metal oxides of silicon and aluminium, tin or titanium often result in precipitation of metal rich intermediates at the solution stage. Clearly, dimerisation and precipitation of metal rich intermediates has not occurred, as the mixed metal ratio at the pore walls is consistent with reactant concentrations. The optimised prehydrolysis process was effective for the formation of Si:Ti binders with a 1:1 atomic ratio and Si:Al in a 2:1 ratio.

EDX analysis also revealed residual carbon as a by-product of template combustion. Carbon is always detected during EDX analysis on account of carbon deposition occurring

under the electron beam due to contamination. However, the amount detected by the EDX system was large enough to suggest carbon was present in the sample. The carbon content is a potential contaminant in catalytic and optical applications and was removed by passing an ozone stream over the sample for 30 minutes. Subsequent EDX analysis revealed a considerable reduction in the carbon content of the sample highlighting the effectiveness of the ozone treatment. In the case of the tin silicates, trace quantities of chlorine were also detected in the final materials. This contaminant arises because tin (IV) chloride was used as a precursor and some residual chlorine retained in the final material.

3.3.5 Homogeneity

Although the final composition has been verified to be consistent with the initial sol compositions in the section above it is still unclear if the sol is separating into discreet metal rich and silicon rich regions. A common problem in the sol-gel fabrication of mixed metal oxides is that the hydrolysis rates of the various metal alkoxides is often very different. In the case of M-Si binary gels the rate of hydrolysis of the metal alkoxides is usually much higher than that of the silicon alkoxides. As a result of this the metal alkoxides tend to react with themselves preferably to reacting with the silicon alkoxides resulting in phase separation in the gels. This separation often reduces the usefulness of these materials and is not desirable for atomic scale homogeneity.

Two main approaches can be utilised to try and overcome this problem the first involves complexation of the faster hydrolysing alkoxide. This serves to reduce the number of active sites available for hydrolysis thereby bringing the hydrolysis rates of the two alkoxides closer together. However, the presence of complexing species also restricts the condensation process resulting in films with poor mechanical and thermal stability. The second method, which was adopted in this work, is the prehydrolysis route whereby the silicon alkoxide is prehydrolysised in order to produce species which react faster with the metal alkoxide than the self condensation of metal alkoxide occurs.

The effectiveness of the prehydrolysis route in the formation of homogenous sols was discussed in detail in a recent publication by Ryan and co-workers. The publication states that judicious pre-hydrolysis of silicon alkoxides produces reaction intermediates that react faster with metal alkoxides (specifically aluminium alkoxides) than the self-condensation of the metal alkoxide occurs. Ideally, the silicon alkoxide in the form of tetra ethoxy silane hydrolyses to its Q_2 species ($(OEt)_2Si(OH)_2$) prior to the addition of

metal alkoxides. This process takes approximately 10 minutes in the presence of a dilute acid at 40 °C and can be monitored effectively by nuclear magnetic resonance spectroscopy (Figure 3.14).

In order to assess the homogeneity of the samples prepared in this research, they were investigated using both FT-iR and solid state NMR.

a) Titanosilicates

Solid phase Si-Ti mixed oxides are often characterized by infrared (IR) absorption spectroscopy. Distinctive absorptions by silica and titania species in the low wavenumber region of the IR absorption spectrum are particularly useful for characterising the degree of homogeneity in titanosilicate materials. Figure 3.13 shows accumulated spectra for solid phase macroporous Ti-Si mixed oxides with atomic ratios of 1:1, 1:2, 1:3, 1:4 and 1:10 respectively.

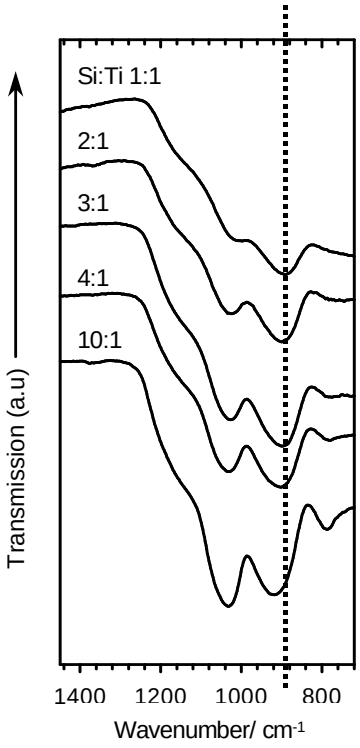

Figure 3.13: Low wavenumber FT-IR transmission spectra of Si:Ti mixed oxides. All samples were calcined at 350 °C. The dotted line is an eye guide for the shift in the Ti-O-Si peak at 920 cm-1.

The sample with the highest silica loading (Ti:Si, 1:10) selectively absorbs at 800 cm^{-1}, 920 cm^{-1} and 1050 cm^{-1} with a small shoulder at 1200 cm^{-1} related to the longitudinal optical (LO) component of the Si-O-Si asymmetric stretching [32]. The lowest wavenumber absorption corresponds to symmetric stretching vibration of Q_4 (SiO^{4-}) species. This feature diminishes as more titanium content is introduced into the silica framework and is completely absent in macroporous oxides with 50% titania loading. Similarly, the intensity of asymmetric vibration from the Q_4 species (1050 cm^{-1}) decreases in line with titanium enrichment. The absorption band at 920 cm^{-1} mirrors that expected for asymmetric stretching of oxygen atoms coordinated to silicon and titanium and is characteristic of homogenous titanosilicate glasses [33]. Absorption bands in this region can also be attributed to the stretching vibrations of the silanol Si-OH groups. However, the constant feature intensity as a function of titania together with the lack of a further silanol band at 3400 cm^{-1} implies Si-O-Ti is the more likely absorber. Close inspection of this peak shows that the band gradually broadens and shifts to lower frequency as the Si:Ti ratio increases. This behaviour can be attributed to successive incorporation of Ti^{4+} ions into the silica network, accompanied by a reduction of the average bond strength of the Si-O bonds in the glass structure [34, 35]. The absence of silica features in the binary (1:1) Si-Ti Macroporous oxide combined with a strong resonance from Si-O-Ti is evidence for homogenous distribution of silicon and titanium atoms in the sol-gel binder after calcinations. Clearly, metal leaching has not occurred such that the sol-gel approach is proven effective for the deposition of homogenous titanosilicate matrices with 50 % loading without the need for complexing agents.

b) Aluminosilicates

The aluminosilicate sols were synthesised using a method previously described by Ryan et al. Figure 3.14 below shows a ^{29}Si MAS-NMR study of the sol formation that was presented in the publication. Figure 3.14i shows NMR of the unhydrolysed sol and shows a strong peak due to TeOS at -82.3 ppm. Hydrolysis of the TeOS causes the up-field resonances at -87 ppm and -94 ppm and these are due to hydroxylated Q_1 ($Si(OSi)(OH)_3$) and Q_2 ($Si(OSi)_2(OH)_2$) silicon species (Figures 3.14ii and iii). Aluminium incorporation immediately prior to the onset of silicon self-condensation, in the form of aluminium sec butoxide, results in rapid condensation of the Q_1 and Q_2 silicon species (Figure 3.14iv), and subsequently a highly homogenous aluminosilicate matrix with no evidence of silica

rich regions. If silica rich regions were present we would expect a very strong peak at about -112 ppm corresponding to the fully condensed Q_4 species $Si(OSi_4)$ (Figure 3.14v).

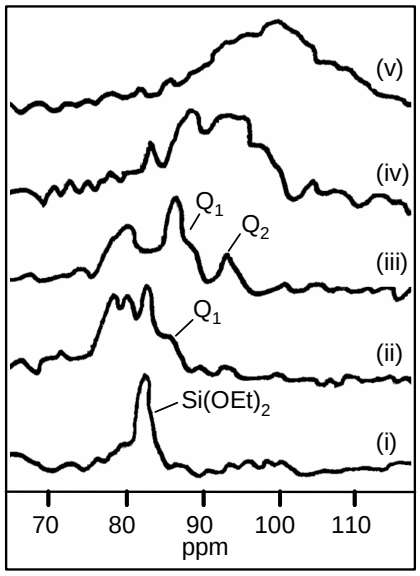

Figure 3.14: Stacked ^{29}Si MAS-NMR of silica and aluminosilicate hydrolysis

The sol-gel synthesis in the paper however describes an aluminosilicate sol with a relatively low aluminium loading (ca ~ 4 %), in our work heterometal loadings as high as 33 % were achieved so the question of homogeneity is still unclear with regards to these materials with very high heterometal incorporation. Low wavenumber iR is typically less useful for characterising the aluminosilicate materials as the Al-O-Si bonds do not exhibit any characteristic bends or stretches in this region.

Presented in figure 3.15 is accumulated iR data for a series of aluminosilicates with increasing aluminium loadings, the data shows that both the peaks at 1200 cm^{-1} and 800 cm^{-1} which results from Si-O-Si bonds as detailed previously decrease with increasing aluminium incorporation indicating that the degree of Si-O-Si bonds in the bulk material is decreasing. Furthermore the lack of a band at 920 cm^{-2} which can be attributed to terminal Si-OH stretching vibrations indicates that there is not a sudden increase in silanol bonds which would be expected if phase separation was occurring. This is because we would expect these terminal silanol bonds to occur at the boundaries of neighbouring silicon rich and aluminium rich regions. The lack of these bonds lends extra support to the homogeneity of these materials.

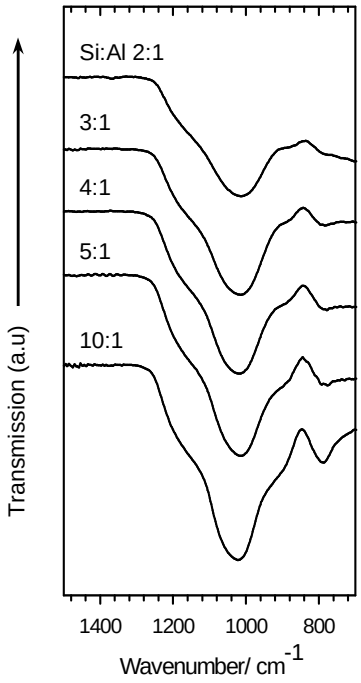

Figure 3.15: Low wavenumber FT-IR transmission spectra of Si:Al mixed oxides. All samples were calcined at 350 °C.

3.3.6 Thermal stability

For any catalytic applications it is essential that a nanoporous material has both structural and compositional stability and consequently the stability of the mixed metal macroporous oxides as a function of temperature was studied using powder X-ray diffraction, FT-IR and SEM imaging. Figure 3.16 shows stacked X-ray diffraction plots of macroporous (Macropore diameter = 351 nm) 2:1 Si:Ti subjected to calcination temperatures from 350 °C to 1300 °C.

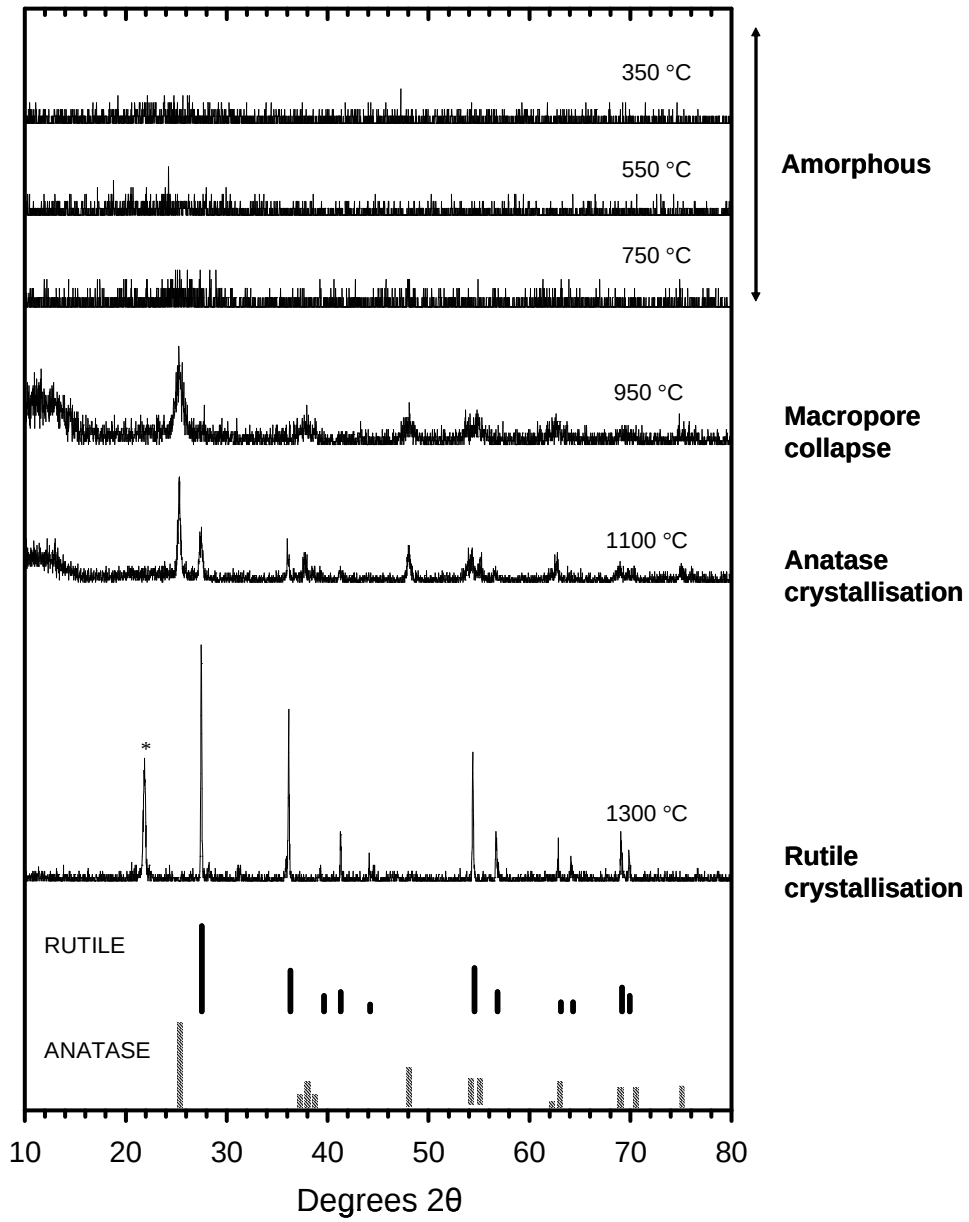

Figure 3.16: Powder XRD patterns of 1:1 Ti:Si titanosilicate samples calcined at the temperatures indicated. The asterisk denotes the Cristobalite reflection.

As expected, the sol-gel deposited Si-Ti framework is completely amorphous at 350 °C. The onset of crystallisation (950 °C) coincides with an observed loss of opalescence as framework degradation leads to macropore collapse. Crystalline anatase peaks emerged at 950 °C and sharpened at 1100 °C from particle sintering. At temperature extremes > 1300 °C the rutile phase of TiO_2 dominates and SiO_2 begins to crystallise in the form of Cristobalite (Figure 3.16).

Figure 3.17 shows accumulated FT-IR spectra of a 1:1 titanosilicate matrix calcined at temperatures of (350, 550, 750, 950, 1100 and 1300 °C respectively). The Ti-O-Si absorbance at 920 cm^{-1} is clearly evident at 350 °C but diminishes considerably as the degree of heterogeneous bonding decreases at greater temperatures. The concomminant increase in intensity of the band at 1050 cm^{-1} resulting from homogenous Si-O-Si bonding shows that as the calcination temperature is increased TiO_6 rich phases are formed at the expense of Ti^{4+} in tetrahedral coordination. It is likely that nanosized titanium rich phases are present even at the lowest temperatures but prolonged heat treatment causes these regions to grow and eventually crystallise out at sufficiently intense temperatures. The degree of heterogeneous bonding within the titanosilicate matrix is clearly highly dependent upon the temperature at which the samples are treated upon template removal.

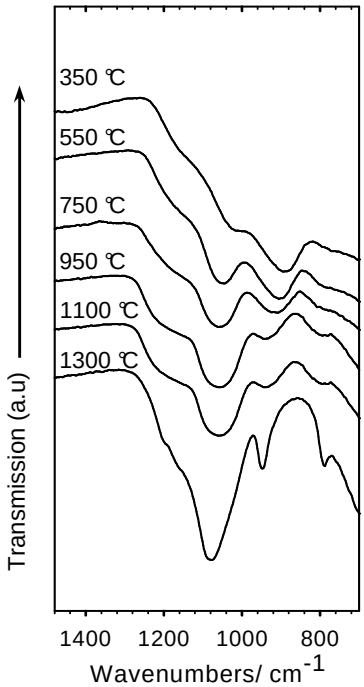

Figure 3.17: Low wavenumber FT-IR transmission spectra of 1:1 titanosilicate samples calcined at temperature ranges from 350 – 1300 °C,

The macroporous pore structure is extremely robust at temperatures below 900 °C. Figure 3.18 shows an SEM image of a sample cleaved from a substrate followed by calcination at 750 °C for 6 h. The image is a cross-section of the macroporous network showing that the three-dimensional structure and morphology is preserved at these conditions.

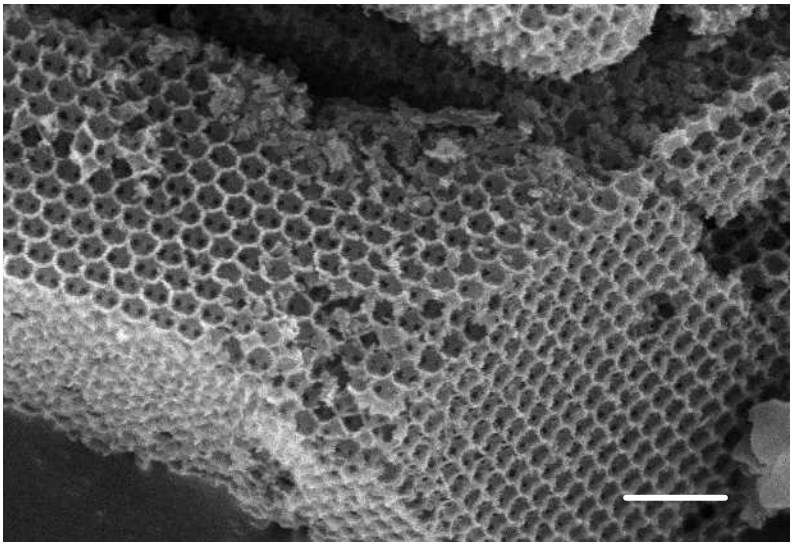

Figure 3.18: SEM image of a powdered macroporous titanosilicate sample with Ti:Si atomic ratio of 1:1 which has been subjected to further heat treatment at 750 °C for 6 hours. Scale bar represents 1 µm.

The macroporous aluminosilicate matrices were more robust; in this case pore collapse occurred at 1100 °C. The aluminosilicate (1:2) matrix was completely amorphous up to temperatures of 1300 °C where crystalline reflections from the silica rich Cristobalite phase and the aluminium silicate sillimanite phase (Al_2SiO_5) emerged and sharpened due to sintering at 1300 °C (Figure 3.19).

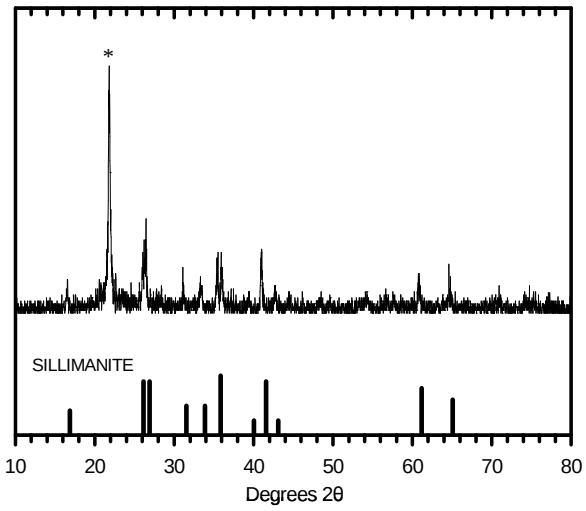

Figure 3.19: Powder XRD pattern of a 1:2, Al:Si aluminosilicate sample calcined at 1300 °C. The asterisk denotes the Cristobalite reflection.

The tin silicates also required a greater degree of heating before the two metal oxides completely separated and crystallised out with the onset of crystallisation occurring at 1100 °C with sharp peaks observed for samples calcined at 1300 °C (Figure 3.20). The tin crystallised out in the form of syn-cassiterite whilst the silica once again crystallised out as Cristobalite.

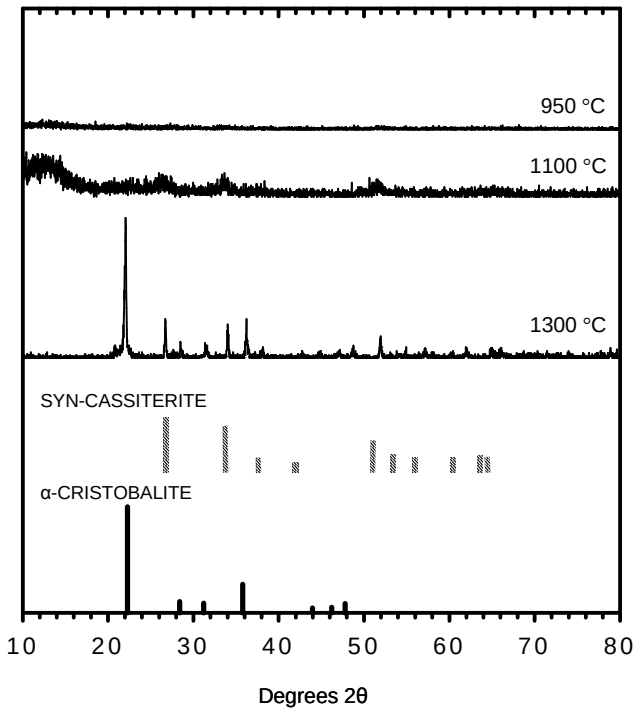

Figure 3.20: Powder XRD pattern of a 1:2, Sn:Si tin silicate sample calcined at various temperatures.

3.3.7 Optical properties

The structural order in the templated macroporous oxides causes Bragg diffraction of white light, which results in vivid diffractive colours dependent on the angle of observation (Figure 3.21). This occurs providing the pore size is within the same length scale as the visible spectrum and this property has lead to commercial interest in these materials as potential special effect pigments.

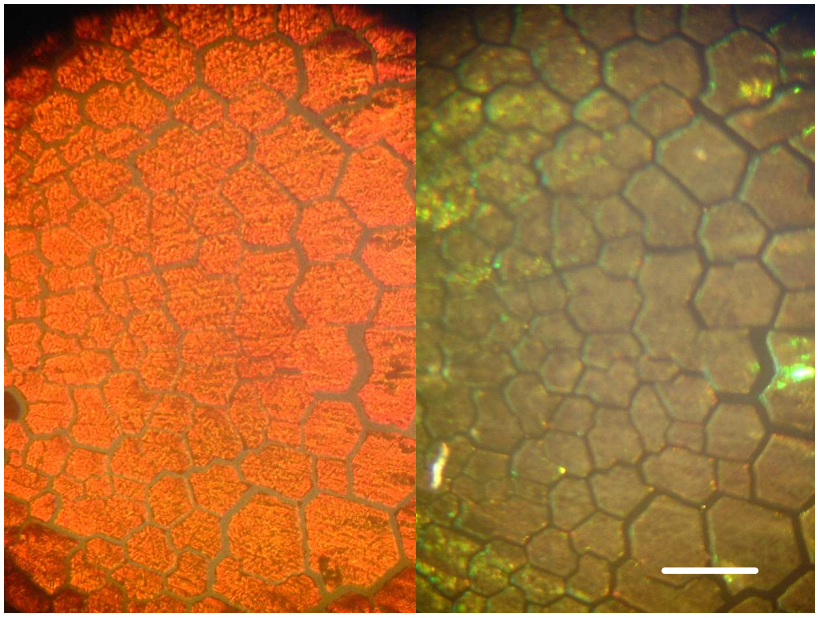

Figure 3.21: Optical microscope image of macroporous titanosilicate film (Si:Ti, 2:1) illuminated with light at (left) 0° (right) 75°. Materials were fabricated from a colloidal crystal template composed of 356 nm PMMA spheres. Scale bar is represents 1 mm.

Reflectance spectra were recorded for macroporous mixed oxide samples at normal incidence in the range 400 to 1000 nm. Figure 3.22 shows the reflectance spectra of titanosilicate films with Ti:Si ratios of 1:1, 1:4 and 1:10 respectively. A large diffraction maximum is observed at around 610 nm and this maxima clearly shifts towards higher frequencies with increasing titanium incorporation

The effective refractive index of the film (n_a) can be evaluated using the Bragg equation [1] where, λ is the maximum of the reflectance peak, d is the lattice constant, n_a is the average refractive index of the film and θ is the angle of incident light. As the dominant surface in our close packed samples (fcc) is the (111) face d can be evaluated by equation [2] which gives the relationship between the lattice constant (d) and nearest

neighbour distance of spheres (D). Finally the refractive index of the titanosilicate material (n_0) can be evaluated by equation [3] where n_{air} is the refractive index of air, which is 1 and ϕ is the volume fraction occupied by the air spheres (0.74).

$$[1] \quad \lambda = 2d\, n_a \sin\theta$$

$$[2] \quad d = d_{111} = (2/3)^{1/2} D$$

$$[3] \quad n_0 = (n_a - n_{air}\, \phi) / (1-\phi)$$

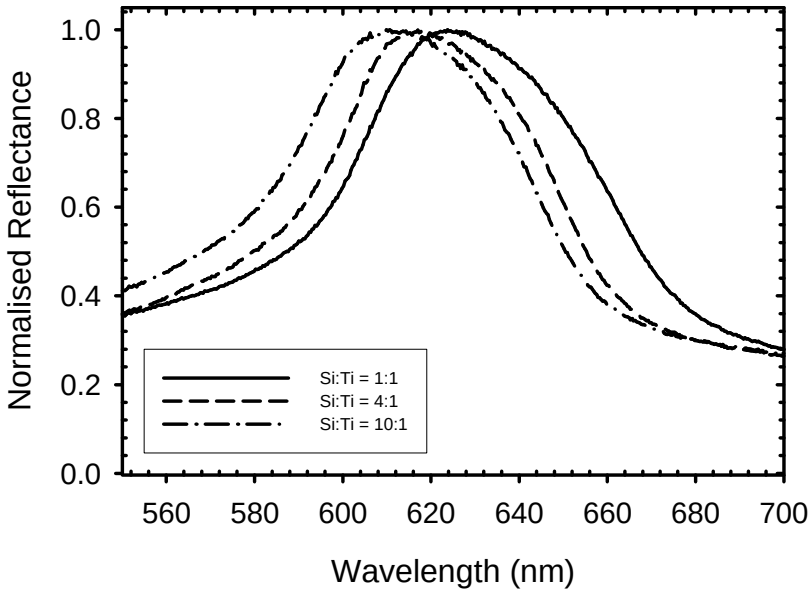

Figure 3.22: Optical reflectance spectra of Si:Ti mixed oxides

The refractive indices of the mixed macroporous oxides as a function of atomic ratios were calculated with D = 329 nm (Assumed constant for all the samples) and a volume fraction, ϕ = 0.74, typical for face centred cubic close packing. The refractive indexes are shown in table 1 and range between 1.526 and 1.625. These values show incremental increases from a pure silicate sample synthesized in the same manner (n = 1.431) as a function of titania incorporation. Therefore, the incorporation of titania in silicate networks using prehydrolysis assisted sol-gel routes allows the effective modulation of refractive index as a function of Si:Ti atomic ratio.

Si/Ti Atomic ratio	Peak maximum (nm)	n_a	n_0
1	624.5	1.163	1.625
2	622.1	1.160	1.614
3	619.7	1.156	1.601
4	618.0	1.151	1.579
5	616.7	1.149	1.572
10	610.3	1.137	1.527

Table 3.5: Atomic ratios, reflection wavelength maxima and refractive indices of a range of titanosilicate macroporous oxides

3.4 Conclusions

The formation of three dimensionally ordered macroporous mixed metal oxides using a facile sol-gel process is reported. Judicious prehydrolysis of the silicon alkoxide precursors allows the formation of titanosilicate and aluminosilicate macroporous oxides with very high heterometal loading. In particular, the route allows macroporous oxides to be synthesised with framework walls consisting of Si:Ti oxide walls in a 1:1 ratio. The titanosilicate and aluminosilicate porous networks were stable to temperature extremes of 900 ^{o}C and 1000 ^{o}C respectively prior to crystalline phase separation and pore collapse. Consequently, the mixed macroporous oxides are ideal for high temperature catalytic applications with large molecular weight compounds. This work represents a significant advance in the synthesis of mixed metal oxide macroporous oxides where previous synthetic routes were limited to a maximum of 3:1 Silica:Heterometal loading and required the use of complexing agents to equalise the hydrolysis rates of the metal alkoxide precursors. The ability to vary the heterometal content with precision allowed the refractive index of the macroporous matrix to be effectively modulated. Controlling the refractive index of a material periodic to the wavelength of light has useful applications for light manipulation in photonic systems.

3.6 References

(1) Yang, Y.; Guo, Y.; Hu, C.; Wang, E., Lacunary Keggin-type polyoxometalates-based macroporous composite films: preparation and photocatalytic activity. *Applied Catalysis, A: General* **2003,** 252, (2), 305-314.

(2) Johnson, B. J. S.; Stein, A., Surface Modification of Mesoporous, Macroporous, and Amorphous Silica with Catalytically Active Polyoxometalate Clusters. *Inorganic Chemistry* **2001,** 40, (4), 801-808.

(3) Farrusseng, D.; Julbe, A.; Guizard, C., Evaluation of porous ceramic membranes as O2 distributors for the partial oxidation of alkanes in inert membrane reactors. *Separation and Purification Technology* **2001,** 25, (1-3), 137-149.

(4) Choudhary, V. R.; Mamman, A. S.; Uphade, B. S.; Babcock, R. E., CO2 reforming and simultaneous CO2 and steam reforming of methane to syngas over CoxNi1-xO supported on macroporous silica-alumina precoated with MgO. *ACS Symposium Series* **2002,** 809, (CO2 Conversion and Utilization), 224-240.

(5) Yabuki, M.; Takahashi, R.; Sato, S.; Sodesawa, T.; Ogura, K., Silica-alumina catalysts prepared in sol-gel process of TEOS with organic additives. *Physical Chemistry Chemical Physics* **2002,** 4, (19), 4830-4837.

(6) Gille, W.; Enke, D.; Janowski, F.; Hahn, T., Platinum Dispersion Analysis Depending on the Pore Geometry of the Support. *Catalysis Letters* **2004,** 93, (1-2), 13-17.

(7) Nowak, I., Textural and structural properties of niobium-containing micro-, meso- and macroporous molecular sieves. *Colloids and Surfaces, A: Physicochemical and Engineering Aspects* **2004,** 241, (1-3), 103-111.

(8) Rubio, F.; Rubio, J.; Oteo, J. L., Effect of TiO2 on the pore structure of SiO2-PDMS ormosils. *Journal of Sol-Gel Science and Technology* **2000,** 18, (2), 105-113.

(9) Jiang, P.; Bertone, J. F.; Hwang, K. S.; Colvin, V. L., Single-Crystal Colloidal Multilayers of Controlled Thickness. *Chemistry of Materials* **1999,** 11, (8), 2132-2140.

(10) Ni, P.; Dong, P.; Cheng, B.; Li, X.; Zhang, D., Synthetic SiO2 opals. *Advanced Materials (Weinheim, Germany)* **2001,** 13, (6), 437-441.

(11) de Soler-Illia, G. J.; Sanchez, C.; Lebeau, B.; Patarin, J., Chemical Strategies To Design Textured Materials: from Microporous and Mesoporous Oxides to Nanonetworks and Hierarchical Structures. *Chemical Reviews (Washington, DC, United States)* **2002,** 102, (11), 4093-4138.

(12) Imhof, A.; Pine, D. J., Ordered macroporous materials by emulsion templating. *Nature (London)* **1997,** 389, (6654), 948-951.

(13) Imhof, A.; Pine, D. J., Uniform macroporous ceramics and plastics by emulsion templating. *Advanced Materials (Weinheim, Germany)* **1998,** 10, (9), 697-700.

(14) Widawski, G.; Rawiso, M.; Francois, B., Self-organized honeycomb morphology of star-polymer polystyrene films. *Nature (London, United Kingdom)* **1994,** 369, (6479), 387-9.

(15) Jenekhe, S. A.; Chen, X. L., Self-assembled aggregates of rod-coil block copolymers and their solubilization and encapsulation of fullerenes. *Science (Washington, D. C.)* **1998,** 279, (5358), 1903-1907.

(16) Velev, O. D.; Jede, T. A.; Lobo, R. F.; Lenhoff, A. M., Porous silica via colloidal crystallization. *Nature (London)* **1997,** 389, (6650), 447-448.

(17) Xia, Y.; Gates, B.; Yin, Y.; Lu, Y., Monodispersed colloidal spheres: Old materials with new applications. *Advanced Materials (Weinheim, Germany)* **2000,** 12, (10), 693-713.

(18) Wong, S.; Kitaev, V.; Ozin, G. A., Colloidal Crystal Films: Advances in Universality and Perfection. *Journal of the American Chemical Society* **2003,** 125, (50), 15589-15598.

(19) Jiang, P.; Cizeron, J.; Bertone, J. F.; Colvin, V. L., Preparation of macroporous metal films from colloidal crystals. *Journal of the American Chemical Society* **1999,** 121, (34), 7957-7958.

(20) Turner, M. E.; Trentler, T. J.; Colvin, V. L., Thin films of macroporous metal oxides. *Advanced Materials (Weinheim, Germany)* **2001,** 13, (3), 180-183.

(21) Bechger, L.; Vos, W. L., Homogeneity of Oxide Air-Sphere Crystals from Millimeter to 100-nm Length Scales: A Probe for Macroporous Photonic Crystal Formation. *Chemistry of Materials* **2004,** 16, (12), 2425-2432.

(22) Dirken, P. J.; Smith, M. E.; Whitfield, H. J., 17O and 29Si Solid State NMR Study of Atomic Scale Structure in Sol-Gel-Prepared TiO2-SiO2 Materials. *Journal of Physical Chemistry* **1995,** 99, (1), 395-401.

(23) Schattka, J. H.; Shchukin, D. G.; Jia, J.; Antonietti, M.; Caruso, R. A., Photocatalytic activities of porous titania and titania/zirconia structures formed by using a polymer gel templating technique. *Chemistry of Materials* **2002,** 14, (12), 5103-5108.

(24) Huesing, N.; Launay, B.; Doshi, D.; Kickelbick, G., Mesostructured Silica-Titania Mixed Oxide Thin Films. *Chemistry of Materials* **2002,** 14, (6), 2429-2432.

(25) Fujishima, A.; Rao, T. N.; Tryk, D. A., Titanium dioxide photocatalysis. *Journal of Photochemistry and Photobiology, C: Photochemistry Reviews* **2000,** 1, (1), 1-21.

(26) Biz, S.; White, M. G., Syntheses of Aluminosilicate Mesostructures with High Aluminum Content. *Journal of Physical Chemistry B* **1999,** 103, (40), 8432-8442.

(27) Corma, A.; Martinez, A.; Martinez-Soria, V.; Monton, J. B., Hydrocracking of vacuum gas oil on the novel mesoporous MCM-41 aluminosilicate catalyst. *Journal of Catalysis* **1995,** 153, (1), 25-31.

(28) Spirkova, M.; Brus, J.; Hlavata, D.; Kamisova, H.; Matejka, L.; Strachota, A., Preparation and characterization of hybrid organic-inorganic epoxide-based films and coatings prepared by the sol-gel process. *Journal of Applied Polymer Science* **2004,** 92, (2), 937-950.

(29) Ogawa, M.; Ikeue, K.; Anpo, M., Transparent self-standing films of titanium-containing nanoporous silica. *Chemistry of Materials* **2001,** 13, (9), 2900-2904.

(30) Ryan, K. M.; Erts, D.; Olin, H.; Morris, M. A.; Holmes, J. D., Three Dimensional Architectures of Ultra-High Density Semiconducting Nanowires Deposited on Chip. *Journal of the American Chemical Society* **2003,** 125, (20), 6284-6288.

(31) Zakhidov, A. A.; Baughman, R. H.; Iqbal, Z.; Cui, C.; Khayyrullin, I.; Dantas, O.; Marti, J.; Ralchenko, V. G., Carbon structures with three-dimensional periodicity at optical wavelengths. *Science (Washington, D. C.)* **1998,** 282, (5390), 897-901.

(32) Almeida, R. M.; Pantano, C. G., Structural investigation of silica gel films by infrared spectroscopy. *Journal of Applied Physics* **1990,** 68, (8), 4225-32.

(33) Davis, R. J.; Liu, Z., Titania-Silica: A Model Binary Oxide Catalyst System. *Chemistry of Materials* **1997,** 9, (11), 2311-2324.

(34) Carrington, A.; McLachlan, A. D.; Editors, *Introduction To Magnetic Resonance; With Applications to Chemistry and Chemical Physics*. ed.; 1967; 'Vol.' p 266 pp.

(35) Canham, L. T., Silicon quantum wire array fabrication by electrochemical and chemical dissolution of wafers. *Applied Physics Letters* **1990,** 57, (10), 1046-8.

Chapter 4

Contents page

HIERARCHICALLY ORDERED MESO/MACRO SILICA

CHAPTER 4 – Hierarchically ordered meso/macro silica

4.1 Introduction

Hierarchical porous materials have become the focus of much attention recently on account of their potential for technological applications[1] such as electrode materials, selective chemical separation, wave guides and catalysis[2, 3]. For catalytic applications in particular these materials hold considerable promise as they combine the high surface area of mesoporous materials with the large framework structure of macroporous materials, thereby increasing the mass transfer of reactants to the active sites whilst minimising pore blocking. Some groups have already reported methods to synthesise bimodal meso/macro[4-7], micro/meso[8, 9] and micro/macro materials and in very few cases tri-modal micro/meso/macro materials[10].

The preferred method for the production of hierarchical meso/macro materials is to use a dual templating technique. As the name suggests the dual templating method involves combining two templating methods to achieve porosity on both the meso and macro scale. Surfactant aggregates are most commonly employed as the structure directing agent for the mesopores whilst another substance such as colloidal crystals[5, 7, 10], polymer foams[11], bio cellulose's, emulsions[12], vesicles, inorganic salts or ice crystals, are combined into the synthesis to guide the formation of the macrostructure.

For many applications a pore system that is ordered on both the meso and macro scale would be desirable, however dual templating methods commonly result in materials with disordered pore structures which have considerable dispersion in pore size on at least one of the size regimes. The most successful preparative method for hierarchical meso/macro materials, which are ordered on both the meso and macroscale, involves using colloidal crystals as the macrotemplates.

The technique was first reported by Yang et al[7] who used block copolymer, PS spheres and micromoulding to prepare patterned meso/macro silica with ordered cubic mesopores within an ordered macroporous framework on a glass substrate. Sen et al[5] synthesised a series of hierarchically ordered porous meso/macro silica samples by immersing a colloidal crystal into a solution containing triblock copolymer (F127 or P123), TEOS, ethanol and co-surfactants. The resultant materials had a low surface area when

the template was removed by calcination (46 m^2 g^{-1}) and a larger surface area when the template was removed by solvent extraction (531 m^2 g^{-1}) a large portion of which was due to a further microporous structure.

In all cases these preparative methods have been limited to the use of block copolymer surfactants and hence limited size scales of the mesoporous pore walls. Furthermore, to the best of our knowledge the formation of hexagonally ordered pore walls within a 3d ordered macroporous structure is yet to be reported.

The work reported in this chapter details a simple dual templating dip infiltration method that enables the production of highly ordered well defined macroporous materials with mesoporous pore walls using a number of different surfactants. The final materials have very high surface areas and large pore volumes. Furthermore, by varying the sol composition it is possible to tailor the nano-architecture of the final inorganic material at both the meso and macro scale imparting a degree of predictability into this technique.

4.2 Experimental

This experimental section details the general procedure for fabricating hierarchically ordered meso/macroporous silica samples by a dip infiltrated dual templating technique. The first three sections describe the preparation of the colloidal crystal, sol-gel dipping solution and dipping conditions respectively whilst the fourth section describes the different characterisation methods that were used in this study.

4.2.1 Assembly of the colloidal templates

The colloidal crystal templates were assembled by a simple sedimentation method. Microscope slides were precleaned by sequential sonication in water, acetone, isopropyl alcohol and chloroform before a Teflon ring (Internal diameter - 10 mm, Ext. dia. - 20 mm, thickness - 10 mm) was attached by double sided tape. 0.3 ml of a monodisperse suspension of PMMA spheres diluted with water to 1-wt % was confined within the Teflon ring. The water was then allowed to evaporate at room temperature over about 2-3 days. After all the water had evaporated the Teflon ring was removed exposing a circular iridescent packed array of polystyrene spheres on the substrate. This approach formed uniform films of approximately 40 μm thickness.

To enable surface area analysis by N_2 sorption a much larger quantity of material was required than was produced by the standard preparation. As such, larger colloidal crystal templates were required. To prepare the large area templates a larger Teflon ring (Internal diameter ~ 100 mm, ext. dia. 10 mm, thickness 10 mm) was attached to a glass plate using double sided tape. 7 ml of the 1 wt % monodisperse PMMA sphere solution was confined within the ring and was allowed to evaporate at room temperature over 2-3 days. This process produced samples that were only partly iridescent indicating that the ordering of the colloidal crystal was poorer.

4.2.2 Preparation of Sol-Gel Precursors

All the sol-gel precursor solutions were prepared by the same route. Initially surfactant (Pluronic P123, BASF; Pluronic F127, BASF; Brij 56, Aldrich; Brij 78, Aldrich; cetyltriammonium bromide (CTAB), Aldrich) was dissolved in tetraethyl orthosilicate (TEOS, Aldrich) by gentle heating. This was then allowed to cool to room temperature

before the addition of ethanol. This solution was then stirred whilst 0.5 M HCl was added dropwise. This solution was then left stirring at room temperature for up to 21 days.

4.2.3 Fabrication of meso/macro films by dip coating.

The colloidal crystal template adhered to the glass substrate was immersed vertically into the sol, at a rate of 150 mm min^{-1}, before immediately withdrawing at 50 mm min^{-1}. Due to capillary forces the sol infiltrates the interstitial voids of the template. The sample was then dried at room temperature for 24 hours allowing gelation of the sol. Finally the template was removed by slowly heating the sample to 350 °C in air at a rate of 0.9 °C min^{-1}. This temperature was maintained for 600 minutes before slowly cooling over 16 hours.

4.2.4 Characterisation

The primary analytical tools used in this chapter were a scanning electron microscope and a transmission electron microscope. A FEG-SEM (JEOL JSM-6500F) was used to study the macrostructure of the meso/macro films, whilst a 300 kV high resolution TEM (JEOL 3010) was used to study the mesostructure of the materials. As the materials were non conductive they were coated with a thin layer of gold (ca ~ 20 nm) prior to topographical observation in the SEM. The samples were prepared for the TEM as outlined in experimental section 2.32 on page 44.

Finally, nitrogen sorption isotherms were also used to further characterise both the pore morphology and surface area of some of the samples and these were collected using a Gemini 2375 BET surface area analyser.

4.3 Results

A range of hierarchically ordered meso/macro silica materials were prepared successfully by the dip-infiltration of a colloidal crystal, comprising close packed PMMA spheres, with a surfactant containing sol-gel mixture. The process involves impregnating the voids of a colloidal crystal with a solution of surfactant, acid, water and TEOS and excess ethanol via capillary forces. Preferential evaporation of ethanol then drives the formation of an ordered mesophase within the voids of the colloidal crystal in a manner analogous to the evaporation induced self assembly (EISA) method widely reported in the literature to produce mesoporous films[13-16]. An amorphous silica matrix then forms around both the mesophase and the colloidal crystal resulting in a macroporous material with mesoporous pore walls. Both templates can then be removed simultaneously by calcination.

A large number of materials were prepared using reaction mixtures with various compositions and using a variety of surfactants. Systematic changes to the composition of the sol-gel reaction mixture enabled the comprehensive examination of compositional phase space and the following sections provide a detailed discussion of how the various components of the sol-gel mixture affect the nanostructure of the materials on both the meso and macro scale.

Initial work focussed on meso-macro materials fabricated using Brij 56 as the structure-directing agent for the mesophase. Subsequently, Brij 78, block-copolymer surfactants (P123, F127) and the cationic surfactant (CTAB) were also investigated as potential structure directing agents. Finally, the effect of altering the quantity of ethanol in the reaction mixture was also investigated.

4.3.1 Meso/macro silica prepared using Brij 56

The Brij 56 surfactant consists of a mixture of polyethylene oxide (PEO) compounds with the average molecular formula $CH_3(CH_2)_{15}(OCH_2CH_3)_{10}OH$. Brij 56 has previously been utilised as a structure directing agent in the synthesis of mesoporous silica[17-19]. The main advantage of using Brij surfactants over their pure, single chain length, analogues is that they are a fraction of the cost.

a. Phase behaviour of Brij 56

When considering which mesostructures any particular surfactant is likely to form it is often useful to consider its aqueous phase behaviour. Figure 4.1 shows the binary phase diagram of Brij 56 in water, and highlights its diverse phase behaviour. The main phases of interest are the large bimodal (H_1 and I_1), hexagonal (H_1) and lamellar (L_α) domains. There is also a small V_1 (discontinuous cubic) domain.

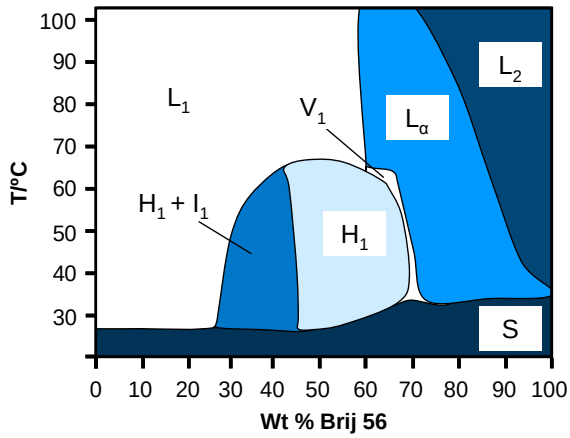

Figure 4.1: Binary phase diagram of Brij 56 in water[27].

Whilst the binary phase diagram above shows how Brij 56 will behave in water the reaction mixtures that were used in this work to synthesise hierarchically ordered meso-macro silica also included a large quantity of ethanol. The inclusion of ethanol inhibits the formation of a mesophase. However, when the colloidal crystal is dipped into the sol preferential evaporation of the ethanol occurs effectively increasing the surfactant concentration and driving the formation of a mesophase.

The reaction mixture used in this work is also further complicated by the presence of both HCl and TEOS, which also alter the phase behaviour of the surfactant. Consequently, the binary phase diagram will only give an indication of the likely phase behaviour of the surfactant and will not be give definitive answers about which specific mesostructure will be formed.

In order to examine the effects each of the constituents of the sol had on the final material, each component was systematically varied whilst the quantity of ethanol with which the sols were diluted was kept constant throughout.

The exact composition of each reaction mixture that was investigated is detailed below in table 4.1.

Sample Ref	0.5 M HCl/g	EtOH/g	TEOS/g	Brij 56/g
$B5^{1}$	3	12	2	3.5
$B5^{2}$	3	12	5	3.5
$B5^{3}$	3	12	9	3.5
$B5^{4}$	3	12	13	3.5
$B5^{5}$	1	12	5	3.5
$B5^{6}$	2	12	5	3.5
$B5^{7}$	4.5	12	5	3.5
$B5^{8}$	7	12	5	3.5
$B5^{9}$	11	12	5	3.5
$B5^{10}$	3	12	5	1
$B5^{11}$	3	12	5	2
$B5^{12}$	3	12	5	3
$B5^{13}$	3	12	5	4
$B5^{14}$	3	12	5	5
$B5^{15}$	3	12	5	9

Table 4.1: **The composition of the reaction mixtures used to fabricate meso/macro silica using Brij 56 as the structure-directing agent for the mesophase.**

This compositional information is also plotted in the ternary diagram (Figure 4.2) which provides a more intuitive view of how these compositions are related to one another.

In the ternary diagram ethanol is neglected and the values presented are then relative wt % of the other three constituents. For example, the relative weight % of HCl for each sample was calculated by the following formula:

$$\frac{Wt_{HCl}}{Wt_{HCl} + Wt_{Surfacatnt} + Wt_{TEOS}} * 100$$

Where Wt_n = Weight of constituent n in grams.

Each sample is also given a code ($B5^{n}$) for simple referral later in the chapter.

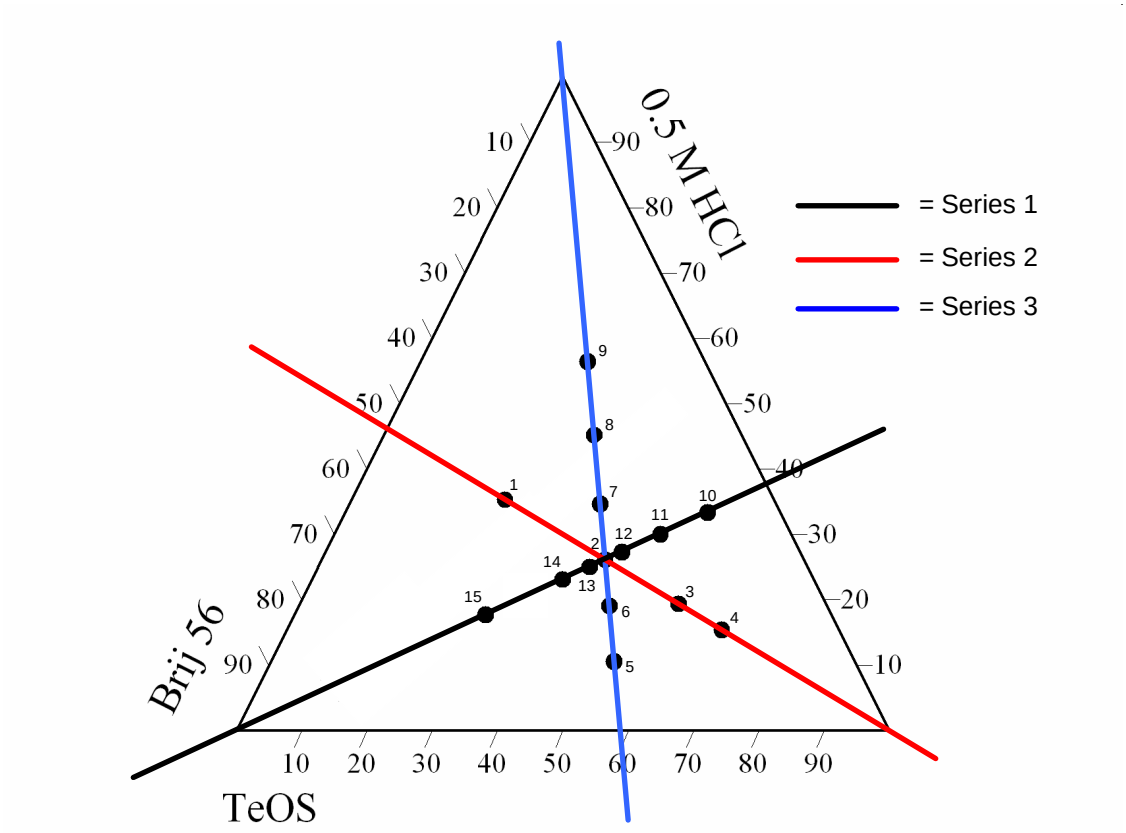

Figure 4.2: Ternary diagram showing the composition of all the silica samples prepared from Brij 56 + TEOS + 0.5 M HCl mixtures.

As shown the different preparations can be classified into three distinct series as highlighted in Figure 4.2.

Series 1 examines the effect of altering the quantity of Brij 56, whilst Series 2 examines the effect of changing the quantity of TEOS in the initial sol. Finally, Series 3 examines the effect of altering the quantity of 0.5 M HCl in the initial reaction mixture.

b. Mesostructure

In order to evaluate the mesostructure of all the samples prepared, each sample was analysed in a 300 kV TEM. The TEM used has a resolution of 0.21 nm enabling the direct observation of any mesostructure within the materials.

Series 1 – Effect of different Brij 56 concentrations

Figure 4.3 shows typical TEM images from each sample in Series 1. Starting with sample $B5^{10}$ (Figure 4.3a) through to sample $B5^{15}$ (Figure 4.3f) the series examines the effect incremental increases in the quantity of surfactant in the initial sol has on the final material.

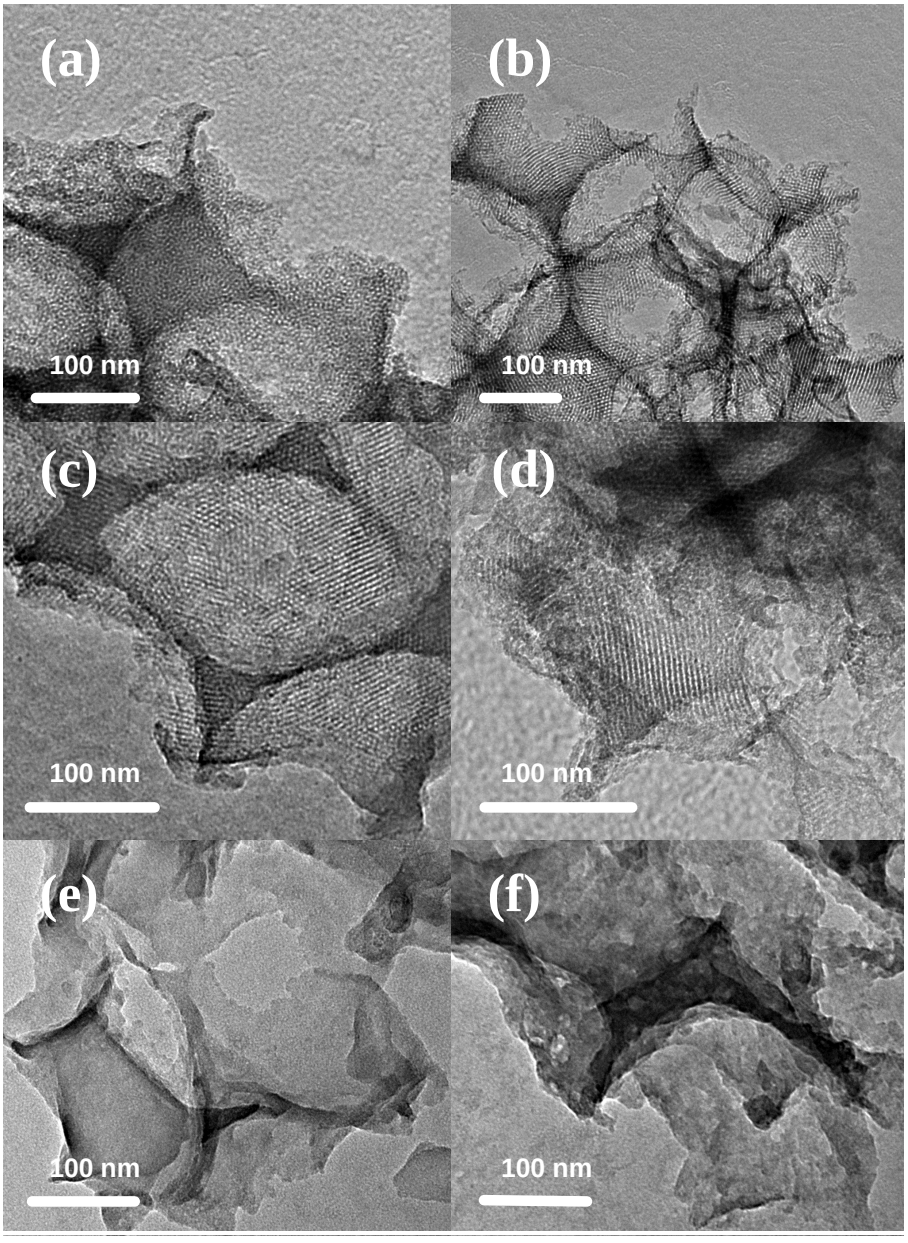

Figure 4.3: **TEM images of meso/macro silica materials fabricated from a sol containing 12 g EtOH, 5 g TEOS, 3 g 0.5M HCl and (a) – 1g Brij 56 (*Sample B5^{10}*), (b) – 2g Brij 56 (B5^{11}) (c) – 3g Brij 56 (B5^{12}), (d) – 4g Brij 56 (B5^{13}), (e) – 5g Brij 56 (B5^{14}) and (f) – 9g Brij 56 (B5^{15}). Materials were templated around a colloidal crystal comprising 346 nm PMMA spheres.**

Both meso- and macro-pore regimes can be clearly seen in the TEM micrographs for samples $B5^{10}$ - $B5^{13}$, highlighting the effectiveness of this method in producing materials with highly ordered mesopore substructures within a macroporous framework.

Variations in the amount of surfactant added to the initial sol produced significant changes to the mesopore structure, which appeared to reflect the binary phase behaviour of Brij 56 and water.

When a sol with a low concentration of Brij 56 was used the final material exhibited a wormhole type mesopore structures (Sample $B5^{10}$, Figure 4.3a). When the surfactant concentration was increased the observed mesopore structure changed from a wormhole structure to an ordered line mesostructure (Samples $B5^{11-13}$, Figures 4.3b-d). From our knowledge of the phase behaviour of Brij 56 it is postulated that the observed line structure is due to the formation of a hexagonal mesophase in the interstitial voids of the colloidal crystal. It is clear that these observed line structures are not conclusive proof of the formation of a hexagonal mesophase and small angle x-ray spectroscopy (SAXS) data on the as formed materials would be an interesting avenue of research in order to conclusively evaluate the ordering of the mesostructure. Further increasing the surfactant concentration had a detrimental effect on the samples mesoporosity, yielding materials with little or no mesoporosity (Samples $B5^{14-15}$, Figures 4.3e-f).

In turn if we consider the binary phase diagram of Brij 56 and water (Figure 4.1), at low surfactant concentration the surfactants aggregate into a hexagonal/cubic multiphase (I_1 + H_1) , as the surfactant concentration is increased a hexagonally ordered mesostructure is formed (H_1). Finally, at high surfactant concentrations the surfactants form a lamellar phase (L_α).

Comparing this pattern with that observed for the materials fabricated in Series 1 three distinct regions were clearly observed. In the first instance we had a wormhole type structure which may well have been the result of templating around a multiphasic mesophase. The second regime we observe is the line structure which is as expected were the hexagonal mesophase acting as the structure directing agent. Finally we have a third region where we have no mesoporosity. It is unlikely this third regime results from a lamellar mesophase as in this case one would expect removal of the template to be

accompanied with the collapse of the mesoporous pore walls and this was not observed. As such, it must be concluded that whilst the phase diagram provides a useful tool for predicting which mesostructure will be formed it does not provide definitive answers.

Series 2 – Effect of different TEOS concentrations

Figure 4.4 shows typical TEM images of each sample from Series two:

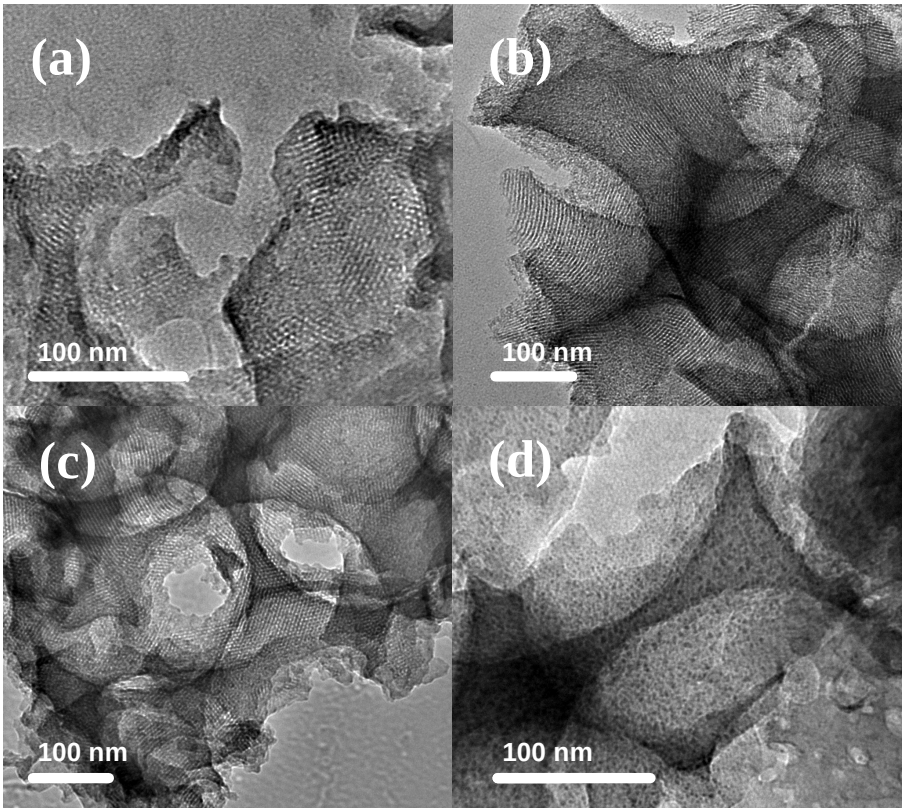

Figure 4.4: Typical TEM images of meso/macro silica materials fabricated from a sol containing 12 g EtOH, 3.5 g Brij 56, 3 g 0.5M HCl and (a) – 2g TEOS (B5^{1}), (b) – 5g TEOS (B5^{2}), (c) – 9g TEOS (B5^{3}) and (d) – 13g TEOS (B5^{4}). Materials were templated around a colloidal crystal comprising 346 nm PMMA spheres.

Once again many of the samples had highly mesoporous substructures incorporated into the macroporous framework. Starting with sample B5^{1} (Fig. 4.4a) the quantity of TEOS was increased systematically throughout Series 2 and it is apparent that varying the TEOS concentration has a considerable impact on the final materials mesostructure.

Increasing the concentration of TEOS in the dipping mixture appeared to affect the mesophase in a manner analogous to increasing the surfactant concentration. At low TEOS concentrations (Sample B5[1], Figure 4.4a) the final material had a mesostructure with poorly defined wormhole type mesoporosity (Fig. 4.4a). Increasing the concentration of TEOS yielded materials with a well defined ordered line structure mesoporosity (Samples B5[2-3], Figures 4.4b & c) throughout the sample. Finally, a large increase in the quantity of TEOS (Samples B5[4], Figure 4.4d) resulted in a largely non-porous material (Fig. 4.4d).

The observed pattern seems to indicate that increasing the concentration of TEOS in the sol promotes the formation of less curved aggregate structures by the surfactant molecules. This phenomenon could occur due to a number of different mechanisms. For instance the silica species could decrease the absorbed surfactant surface charge on the surfactant head groups, by shielding, allowing the head groups to get closer together. It is also plausible the silica species act as bridging species, actively bringing the surfactant head groups closer together.

Series 3 – Effect of the amount of 0.5M HCl

Figure 4.5 shows typical TEM images from each sample in Series 3.

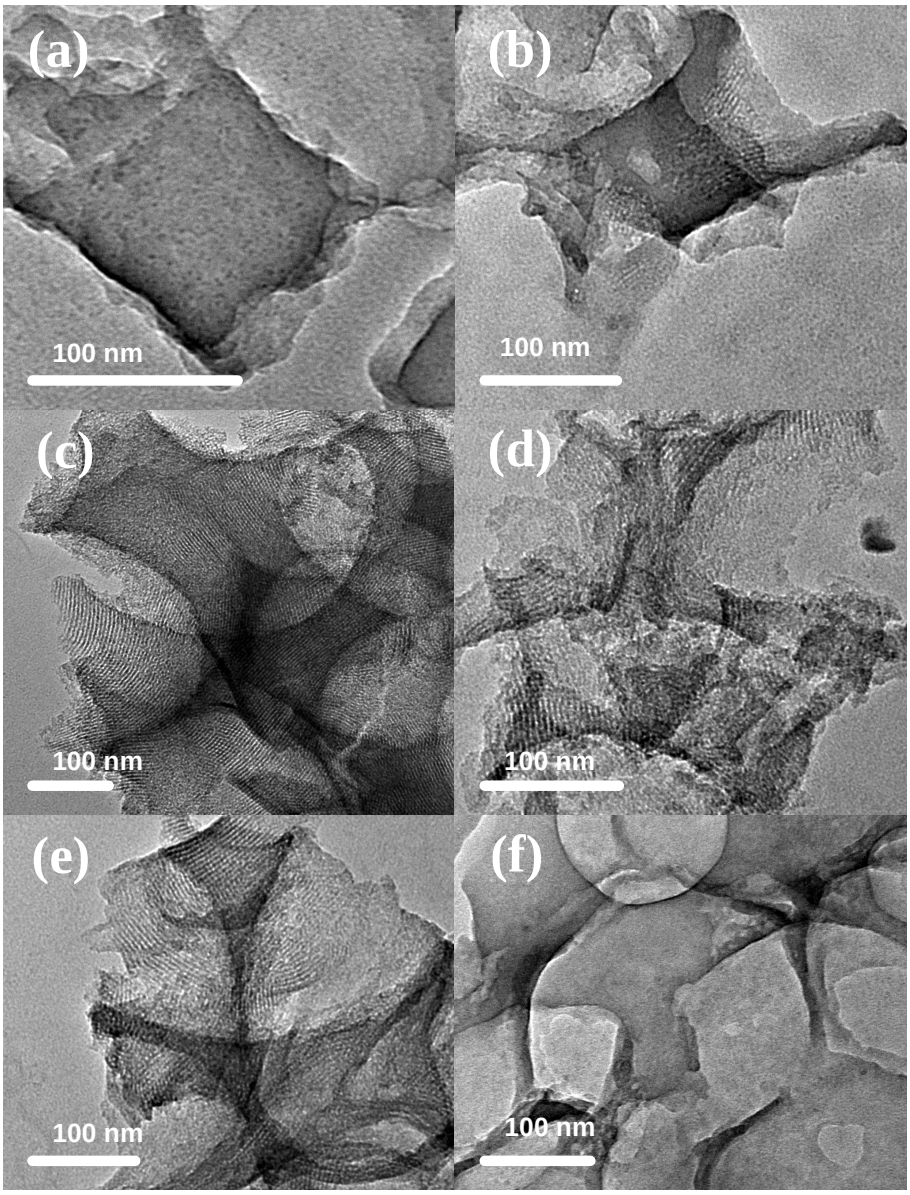

Figure 4.5: **TEM images of meso/macro silica materials fabricated from a sol containing 12 g EtOH, 5 g TEOS, 3.5 g Brij 56 and (a) – 1 g 0.5M HCl (*B5*^{5}), (b) – 2 g 0.5M HCl (*B5*^{6}), (c) – 3 g 0.5M HCl (*B5*^{2}), (d) – 4.5 g 0.5M HCl (*B5*^{7}), (e) – 7 g 0.5M HCl (*B5*^{8}) and (f) – 11 g 0.5M HCl (*B5*^{9}). Materials were templated around a colloidal crystal comprising 346 nm PMMA spheres.**

Series three was investigated to assess what effect varying the quantity of 0.5 M HCl in the initial sol has on the structure of the final material. Once again varying this component of the sol impacted the mesostructure of the final material.
The sample prepared from a solution containing the smallest quantity of 0.5 M HCl had no mesoporous substructure (Sample B5^{5}, Figure 4.5a). A small increase in the amount of HCl resulted in a material that, despite having some small regions with disordered mesoporosity (Sample B5^{6}, Figure 4.5b), was also mostly non-porous. A further increase yielded a material with well-defined ordered mesoporous line structure throughout the sample (Sample B5^{2}, Figure 4.5c). Yet further additions of HCl to the dipping solution resulted in materials with a wormhole mesoporosity (Samples B5$^{7\text{-}8}$, Figures 4.5d –e). Finally, when a very large quantity of 0.5 M HCl was used the sample once again had no mesoporosity (Sample B5^{9}, Figure 4.5f).

When accounting for any observations relating to changes in the quantity of 0.5 M HCl in the initial sol a couple of factors must be considered. Firstly, increasing the quantity of acid in the reaction mixture is accompanied by an increase in the quantity of water in the sol-gel mixture. Secondly, the addition of more acid will, of course, be accompanied by an increase in the pH of the sol.

If we first consider the increase in the quantity of water in the sol the observed pattern can easily be rationalised in terms of the phase diagram, with the ratio of surfactant to water essentially determining the observed mesophase. Increasing the water content moves the system from right to left through the phase diagram in much the same way as observed earlier for decreased surfactant concentration. As such the line structure can once again be attributed to templating around the hexagonal mesophase, whilst the wormhole structure results from templating around the multiphasic mesophase.

On the other hand the ionic strength also affects the PE-groups with the chlorine removing water from the PE region (likely caused by osmotic effect). As a result of this phenomenon the surfactant becomes less hydrophilic and less water soluble. This further explains why poor mesostructures were formed when increased quantities of HCl were added to the dipping mixture.

To help characterise the mesoporous substructures of the materials the average mesopore size and wall thickness for each sample was measured from a number of TEM micrographs, the results of which are summarised below in Table 4.2.

Sample	Pore morphology	Mesopore size /nm	Mesopore wall thickness/nm
1	Wormhole	2.04 ± 0.34	2.00 ± 0.36
2	Line structure	2.30 ± 0.36	2.57 ± 0.48
3	Line structure	2.32 ± 0.32	2.39 ± 0.23
7	Wormhole	2.21 ± 0.36	2.27 ± 0.39
8	Wormhole	2.23 ± 0.24	2.28 ± 0.48
10	Wormhole	2.39 ± 0.55	2.75 ± 0.21
11	Line structure	2.42 ± 0.55	2.63 ± 0.44
12	Line structure	2.3 ± 0.41	2.37 ± 0.26
13	Line structure	2.44 ± 0.50	2.55 ± 0.32

Table 4.2: **Details of the pore morphology, pore size and mesopores wall thickness as evaluated by carrying out image analysis on the TEM images.**

The mesopore size and wall thickness were consistent across the whole range of samples with an average mesopore size of 2.29 ± 0.40 nm and an average wall thickness of 2.42 ± 0.35 nm.

The mesopore morphology was also plotted on a ternary diagram (Figure 4.6) which gives a clearer picture of how changes to the composition of the initial sol gel mixture affect the structure of the final mesophase.

The ternary plot shows that discreet regions within the compositional phase space result in a material with a particular mesostructure, be it wormhole or line structure, and these are highlighted on the ternary diagram.

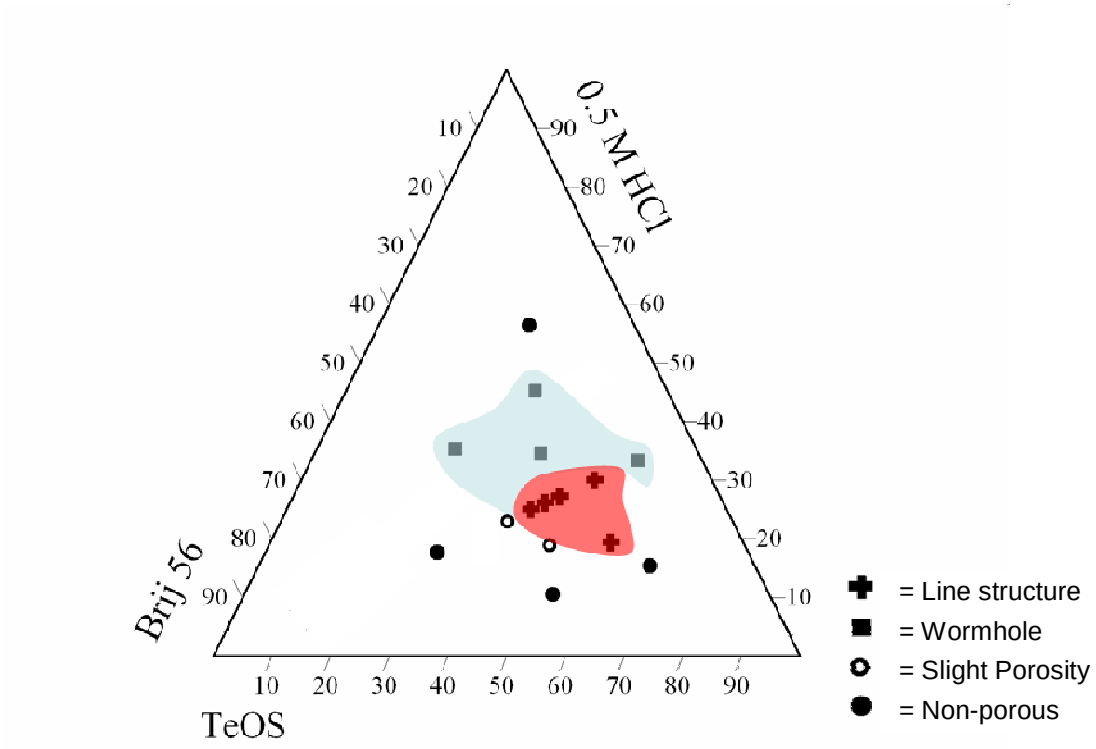

Figure 4.6: Ternary diagram showing the mesopores morphology of meso/macro silica's prepared from a solution containing Brij 56, 0.5 M HCl, TEOS and ethanol.

In summary, the relative concentrations of the three main constituents of the reaction mixture play an integral part in determining the structure and ordering of the mesopores in the final material. Careful manipulation of the components of the initial sol allows both the prediction and synthesis of materials encompassing the desired ordered mesostructure.

This dual templating technique therefore opens up the exciting possibility to specifically tune a material's effectiveness to a particular application by imparting a particular mesopore substructure into the macropore walls by judiciously selecting the appropriate sol-gel composition.

c. Macrostructure

Samples B5[1-15] were also observed in an SEM to assess how altering the composition of the reaction mixture affected the macrostructure of the final material. The results of which are presented below:

Series 1 – Varied Brij 56

Figure 4.7 below shows a typical SEM image for each sample from series one.

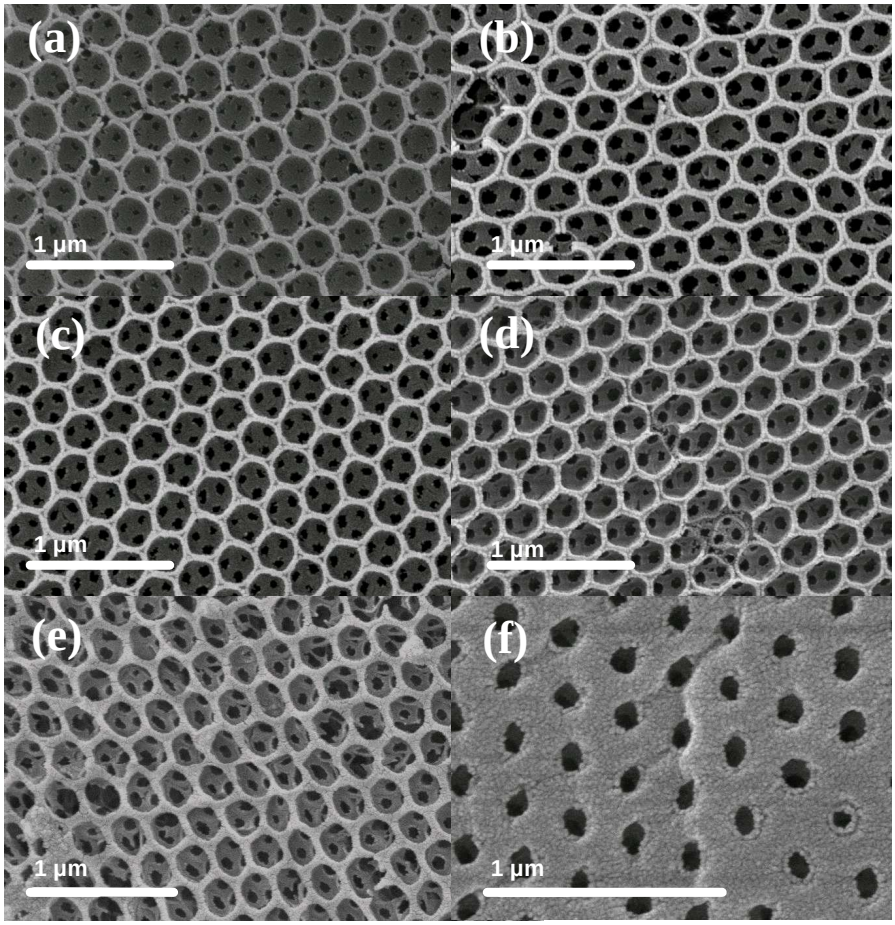

Figure 4.7: SEM images of meso/macro silica materials fabricated from a sol containing 12 g EtOH, 5 g TEOS, 3 g 0.5M HCl and (a) – 1g Brij 56 (B5*[10]*), (b) – 2g Brij 56 (B5*[11]*), (c) – 3g Brij 56 (B5*[12]*), (d) – 4g Brij 56 (B5*[13]*), (e) – 5g Brij 56 (B5*[14]*) and (f) – 9g Brij 56 (B5*[15]*). Materials were templated around a colloidal crystal comprising 346 nm PMMA spheres.

The quantity of surfactant in the initial sol clearly has a lesser effect on the final materials macrostructure than the mesostructure. In all cases the structure of the original colloidal crystal can be clearly identified in the final material. However, when a very large quantity of surfactant was incorporated into the sol (Sample B5[15], Figure 4.7f) the pore walls were

considerably thicker. Another less obvious difference between the six samples was the presence of spandrels in the material fabricated from the sol containing the lowest quantity of Brij 56 (Figure 4.7a) whilst they were not formed when more surfactant was used. Both of these features can be attributed to increases in the surfactant concentration leading to a corresponding increase in the viscosity of the dipping mixture.

Series 2 – Effect of TEOS concentration on Macrostructure

Figure 4.8 shows a typical of SEM image from each sample of Series 2.

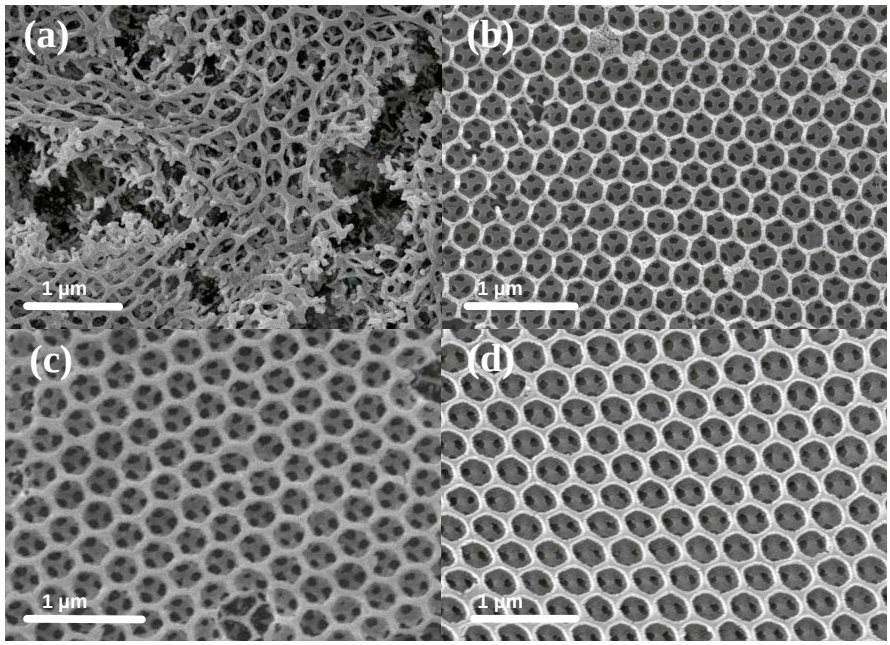

Figure 4.8: SEM images of meso/macro silica materials fabricated from a sol containing 12 g EtOH, 3.5 g Brij 56, 3 g 0.5M HCl and (a) – 2g TEOS (B5^{1}), (b) – 5g TEOS (B5^{2}), (c) – 9g TEOS (B5^{3}) and (d) – 13g TEOS (B5^{4}). Materials were templated around a colloidal crystal comprising 346 nm PMMA spheres.

When only a small amount of TEOS was incorporated into the initial sol-gel mixture the final material had an extremely disordered macroporous structure (Sample B5^{1}, Figure 4.8a). The films were only about 1 micron in thickness (~3 layers) and exhibited a highly distorted pore structure with a large number of tears throughout. Increasing the quantity of TEOS in the initial sol (Sample B5^{2}, Figure 4.8b) resulted in a much more organised film with fewer defects. Further increases (Samples B5$^{3-4}$, Figures 4.8c & d) had no adverse effect on the ordering of the film but led to a slight thickening of the macropore walls.

This progression is expected from alterations in the quantity of TEOS. Initially if we template from a sol containing an insufficient quantity of TEOS there is a deficiency of silica species present to fully infiltrate the interstitial voids of the colloidal crystal. Hence, when the template is removed there is a considerable shrinkage which is accompanied by significant damage to the macroporous framework.

Series 3 – Effect of the amount of 0.5 M HCl on macrostructure

Figure 4.9 shows a typical SEM image from each sample in series 3.

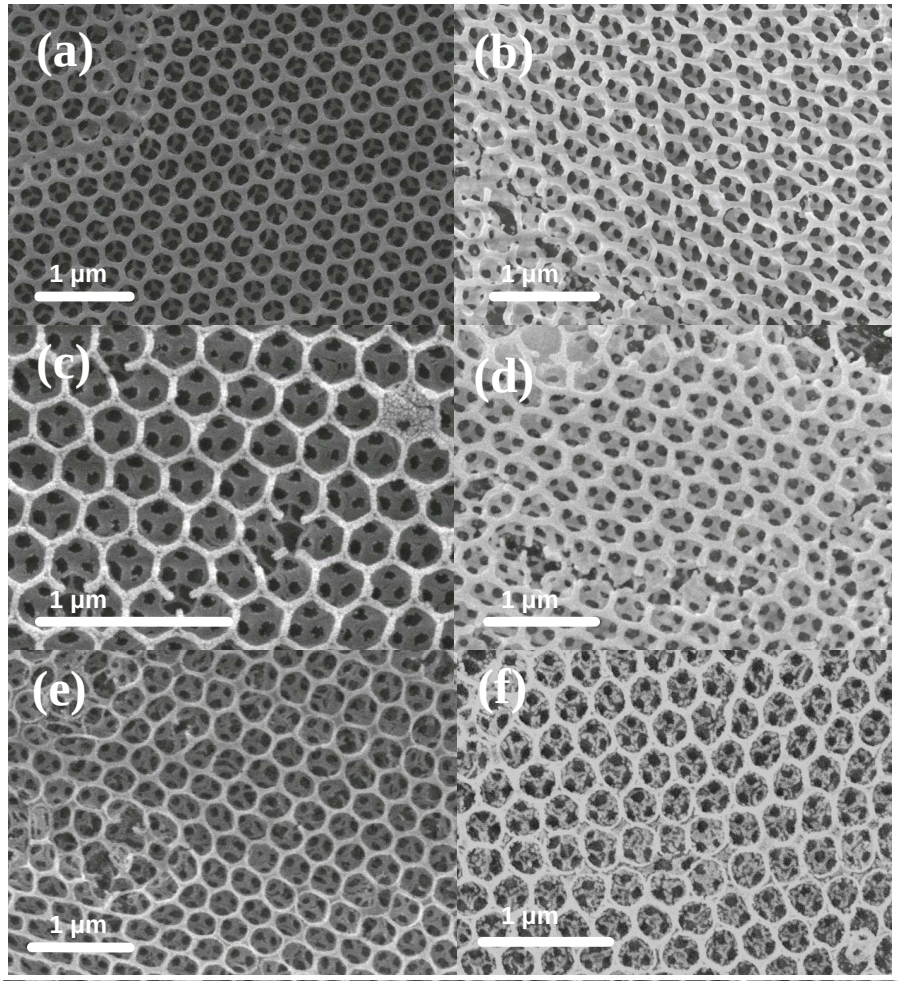

Figure 4.9: **SEM images of meso/macro silica materials fabricated from a sol containing 12 g EtOH, 5 g TEOS, 3.5 g Brij 56 and (a) – 1 g 0.5M HCl (B5^{5}), (b) – 2 g 0.5M HCl (B5^{6}), (c) – 3 g 0.5M HCl (B5^{2}), (d) – 4.5 g 0.5M HCl (B5^{7}), (e) – 7 g 0.5M HCl (B5^{8}) and (f) – 11 g 0.5M HCl (B5^{9}). Materials were templated around a colloidal crystal comprising 346 nm PMMA spheres. Scale bars represent 1 µm.**

In all cases the structure of the original template was replicated in the final material with variation in the quantity of 0.5 M HCl having little effect on the final materials macrostructure.

A point of interest was that the macroporous structure of the meso-macro samples incorporated a much larger number of defects than the macroporous metal silicate materials reported in the previous chapter. Many of the observed defects are tears resulting from shrinkage which accompanies the thermal treatment used for template removal. In addition, areas of the macrostructure where the spherical macropores were heavily distorted in one dimension giving a 'squashed' appearance were also observed. These two observations appear to be due to the introduction of mesopores into the pore walls reducing the mechanical strength of the macrostructure.

In order to quantify the macrostructure the pore-centre to pore-centre distance was measured directly from a number of SEM images for each sample enabling the calculation of the volume shrinkage for each material and this data is summarised below in Table 4.3.

Sample	Mesopore Morphology	Macropore size/nm	Volume shrinkage/%
1	Wormhole	N/A	N/A
2	Line structure	286.5 ± 20.2	43.2
3	Line structure	303.8 ± 14.5	32.3
4	Non-Porous	354.6 ± 20.5	-7.6
5	Non-Porous	333.6 ± 40.1	10.4
6	Slight porosity	334.9 ± 34.7	9.3
7	Wormhole	313.4 ± 25.6	25.7
8	Wormhole	306.1 ± 22.1	30.8
9	Non-porous	300.9 ± 16.9	34.2
10	Wormhole	319.3 ± 14.9	21.4
11	Line structure	306.4 ± 14.9	30.6
12	Line structure	296.0 ± 19.6	37.4
13	Line structure	281.9 ± 19.6	45.9
14	Slight porosity	291.5 ± 25.7	40.2
15	Non-Porous	326.4 ± 27.3	16.0

Table 4.3: **The average macropore size for all the samples prepared from Brij 56 + TEOS + 0.5 M HCl. The original template was composed of 346 nm PMMA spheres.**

The average pore sizes were also plotted on a ternary diagram (Figure 4.10).

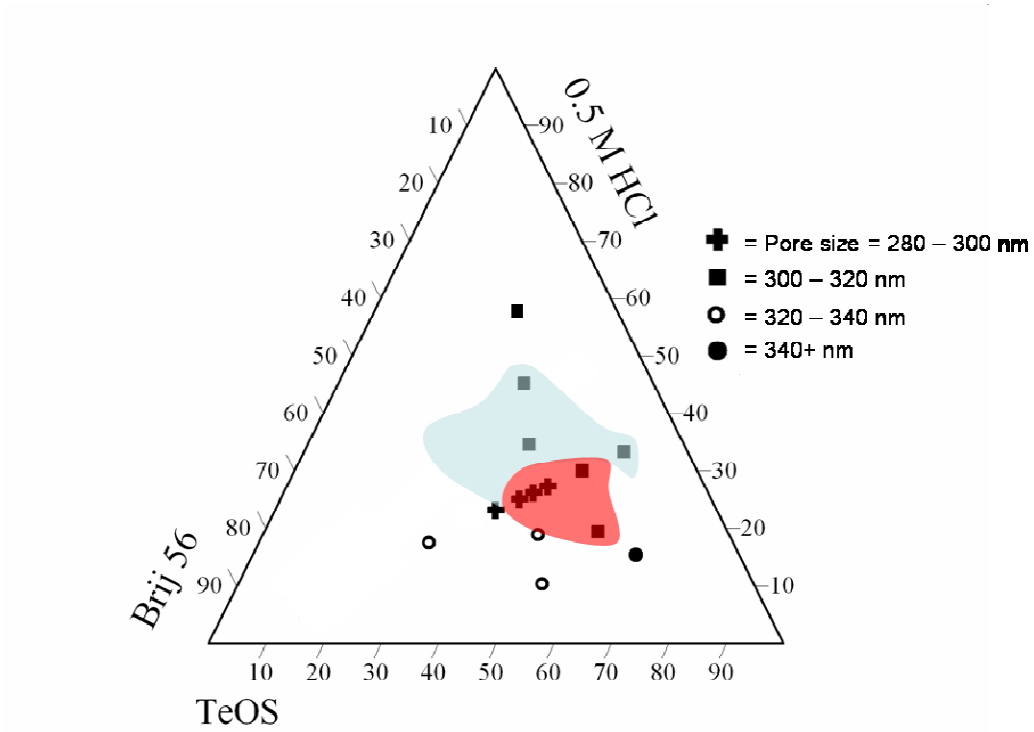

Figure 4.10: **Ternary diagram showing both the macropore size and the mesopore morphology for a range of meso/macro samples synthesised from Brij 56 + TEOS + 0.5 M HCl. The red region corresponds to line structure mesopores whilst the blue region corresponds to the wormhole mesopores.**

The areas predicted to have an ordered line structure and wormhole type mesoporosity are also superimposed onto the ternary diagram and there is a reasonable correlation between the type of mesoporosity and the macropore size. The regions of the ternary diagram showing the greatest amount of shrinkage correspond to those samples which had ordered line structure mesoporous pore walls. Similarly, the samples subject to the second largest amount of shrinkage correspond to those samples with wormhole mesoporosity. Finally, the samples with no mesoporosity tended to shrink the least.

This suggests that the amount of shrinkage occurring in the production of a meso/macro material is intrinsically linked to its mesopore structure. In general the materials with a wormhole type mesoporosity had a total volume shrinkage of about 26 % whilst the materials with ordered line structure mesopores have a total volume shrinkage in the region of 35 %. It is worth noting that this is considerably larger than the volume shrinkage calculated in the previous chapter for the macroporous metal silicates

(Typically in the region of 15 %). It must be noted however that within the accuracy of the data it is difficult to make any clear conclusions.

In summary, the macrostructure is less sensitive to changes in the sol-gel constituents than the mesostructure. All the samples showed some degree of macroporosity and only in the more extreme cases (i.e. very high concentrations of one of the constituents) were the effects on the macrostructure notably detrimental.

d. BET Surface Area Analysis

One of the major benefits of hierarchically ordered meso-macro materials is the ability to combine the large surface area, inherent with a mesoporous material, with the large open pore structure of a macroporous material.

Nitrogen adsorption/desorption analysis makes it possible to quantify both these properties and as such was used to evaluate the surface area, total pore volume and mesopore size of a sample with both hexagonal (Sample B5[12]) and mixed phase mesoporosity (Sample B5[10]).

The BET isotherms and BJH pore size distribution plots are shown in Figure 4.11 for both samples.

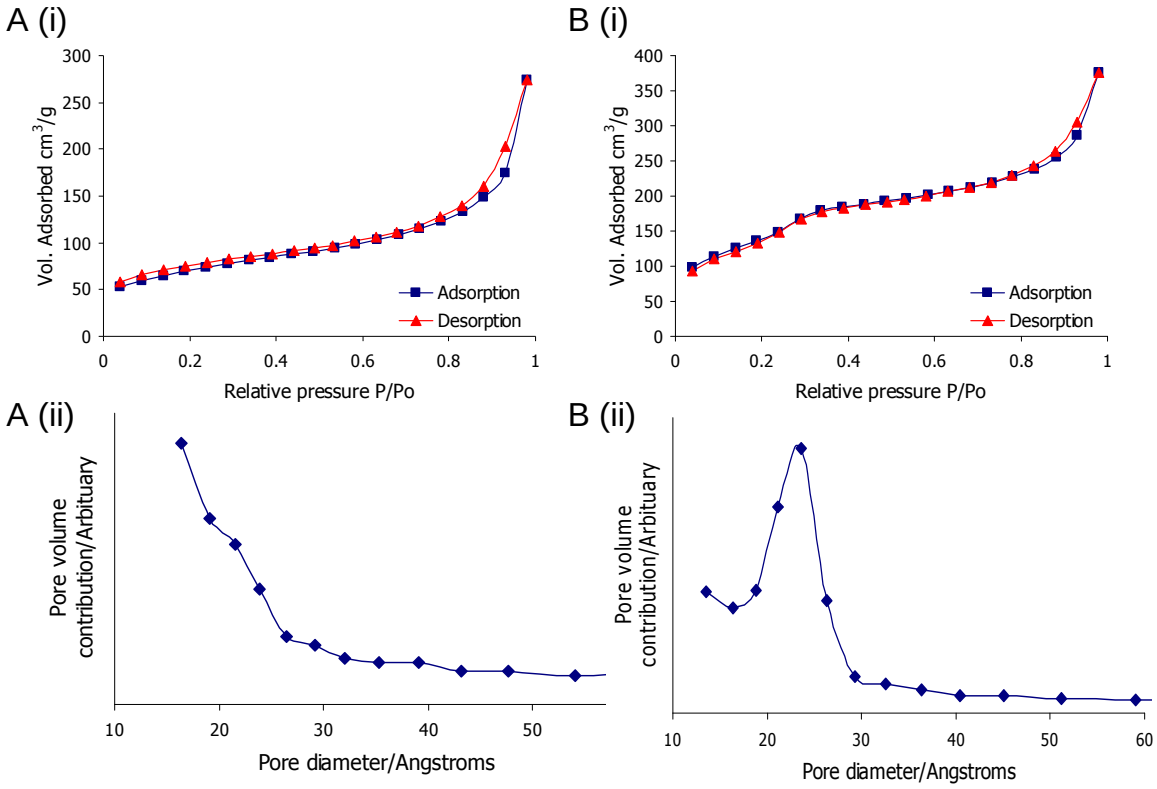

Figure 4.11: Nitrogen adsorption/desorption isotherm for A (i) a sample with wormhole mesopores (*Sample B5*[10]) and B (i) a sample with ordered line structure pores (*Sample B5*[12]). A (ii) and B (ii) The corresponding BJH desorption pore size distribution.

The two materials had very different nitrogen adsorption behaviour. The isotherm from the material with an ordered mesophase (Sample B5[12], Figure 4.11 B (i)) consists of three distinct regions.

Initially there is a steep increase in the volume of nitrogen adsorbed as the pressure increases, corresponding to the filling of the small mesopores in the sample. At a relative pressure of ca ~ 0.37 the rate of adsorption drops considerably and this corresponds to multilayer growth on the surface of the material. Finally, at very high pressures there is a very steep increase in the volume of nitrogen adsorbed which corresponds to the condensation of the adsorbate into the large macropores.

In contrast the isotherm from sample B5[10] (Figure 4.11 A (i)) shows less variation in the initial two phases (Mesopore filling and multilayer growth). The final steep increase in the biphasic isotherm indicates that this also has a highly macroporous structure.

Comparison of the two isotherms suggests that Sample $B5^{12}$ has a higher degree of mesoporosity whilst the macroporous structures are similar in both cases. The surface area was calculated by the BET method for both samples:

Sample 12 (Hexagonal): Surface Area = 517.6 $m^2 g^{-1}$

Sample 10 (Multiphase): Surface Area = 225.6 $m^2 g^{-1}$

The surface area was greater for sample $B5^{12}$ which further confirms the increased level of mesoporosity of the ordered pore system. This is due to the ordered well defined structure enhancing the interconnectivity of the mesopores when compared to the ill defined wormhole type structures.

BJH pore size analysis of the two isotherms also underlines the difference between the two samples. Sample $B5^{12}$ has a sharp peak corresponding to a pore size of 2.3 nm which is consistent with the value calculated from analysis of the TEM images and highlights the tight pore size distribution of the mesopores in this sample and further evidences the ordering of this mesopore system. The material with a wormhole type mesoporosity on the other hand did not have a distinct peak in the BJH pore size distribution and this together with the lower surface area highlights that this material consisted of less well defined mesopores which is consistent with the observation of wormhole type mesoporosity in the TEM micrographs.

4.3.2 Effect of Chemical Structure of Surfactant

One of the principal advantages of surfactant templating is the simplicity, versatility and predictability in producing mesoporous materials with a variety of structures and mesopore sizes simply by employing different surfactants. This enables the tight control of both the mesopores pore size and the ordering of the mesopores by judicious selection of surfactant. The phases observed by any surfactant will relate to the phase behaviour of that surfactant and the size of the mesopores are dependent upon the size of the surfactant molecules.

In the case of Brij 56 it has already been demonstrated that meso/macro silica materials with mesoporous pore walls exhibiting mesophases related to the surfactants phase behaviour can be successfully fabricated by carefully selecting the relative ratios of the sol-gel precursors.

In order to further evaluate the versatility of this dual templating technique in producing meso/macro materials with tailored mesopore sizes and morphologies several other surfactants were used in place of Brij 56 as the structure directing agent for the mesophase.

The results of this study are detailed in the following sections:

a. Brij 78

As already stated the Brij 56 surfactant consists of a mixture of POE compounds with an average molecular formula - $CH_3(CH_2)_{15}(OCH_2CH_2)_{10}OH$, Brij 78 on the other hand has an average molecular formula $CH_3(CH_2)_{17}(OCH_2CH_2)_{20}OH$. Therefore Brij 78 is both longer and has a larger head-group than Brij 56. This structural difference will have a few ramifications on the subsequent mesophase formation. Firstly, because the molecules are longer the subsequent micelles will be larger. Hence using Brij 78 as a structure-directing agent should lead to an increase in the corresponding mesopore size. The second difference will be in the phase behaviour of the two surfactants.

Figure 4.12 shows the binary phase diagram for Brij 78 and water. When the phase behaviour is compared with the phase diagram of Brij 56 it is notable that a cubic phase

is formed as opposed to the multi phase domain formed by Brij 56. Furthermore, the cubic phase domain is much larger than the corresponding mixed phase domain formed by Brij 56. This observation can be rationalised in terms of the larger head-group of Brij 78 which leads to a tendency to favour more curved mesostructures.

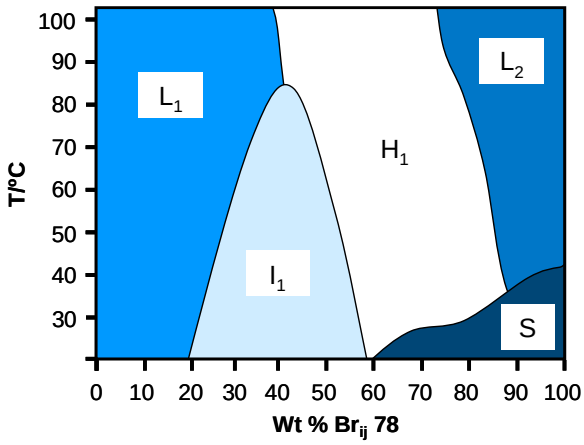

Figure 4.12: The binary phase diagram of Brij 78 in water[27].

Once again to allow the thorough investigation of compositional phase space a large number of sol compositions were used as dipping mixtures. The composition of all the reaction mixtures are summarised below in Table 4.4.

Sample Ref	0.5 M HCl/g	EtOH/g	TEOS/g	Brij 78/g
$B7^{1}$	3	12	5	4
$B7^{2}$	3	12	7	4
$B7^{3}$	3	12	9	4
$B7^{4}$	3	12	13	4
$B7^{5}$	1	12	5	4
$B7^{6}$	2	12	5	4
$B7^{7}$	4.5	12	5	4
$B7^{8}$	7	12	5	4
$B7^{9}$	11	12	5	4
$B7^{10}$	3	12	5	1
$B7^{11}$	3	12	5	2
$B7^{12}$	3	12	5	3
$B7^{13}$	3	12	5	5
$B7^{14}$	3	12	5	6

Table 4.4: Composition of reaction mixtures used to fabricate meso/macro silica using Brij 78 as the structure-directing agent for the mesophase.

The relative composition of the sol constituents is once again plotted onto a ternary diagram together with a sample code B7^{n} (Figure 4.13).

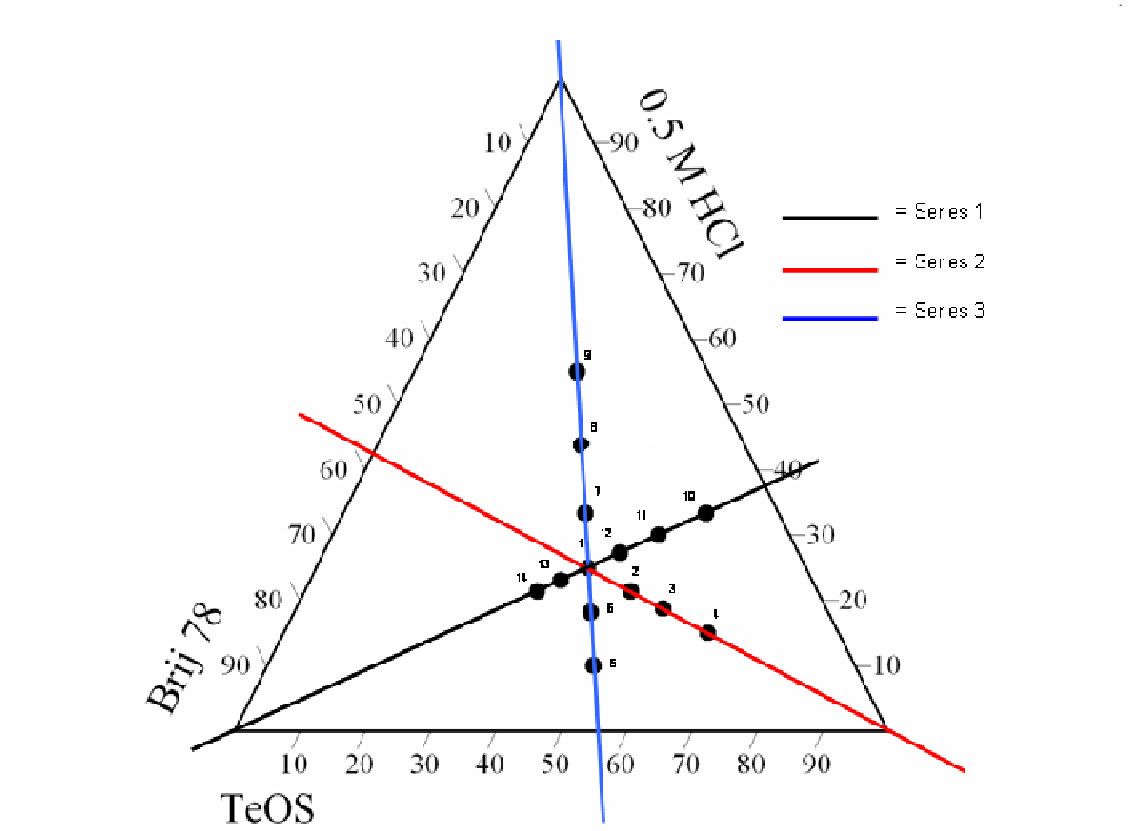

Figure 4.13: Ternary diagram showing the composition of all the silica samples prepared from Brij 78 + TEOS + 0.5 M HCl mixtures.

Again the composition of the reaction mixtures was been chosen such that they can be broken down into three distinct series. Series 1 considers the effect increasing the quantity of surfactant in the reaction mixture has on the final material. Series two looks at the effect of changing the amount of TEOS whilst Series 3 examines the effect of changing the quantity of 0.5M HCl in the reaction mixture.

Series 1 – Effect of different Brij 78 concentration

Figure 4.13 shows a typical TEM image of each sample in series one:

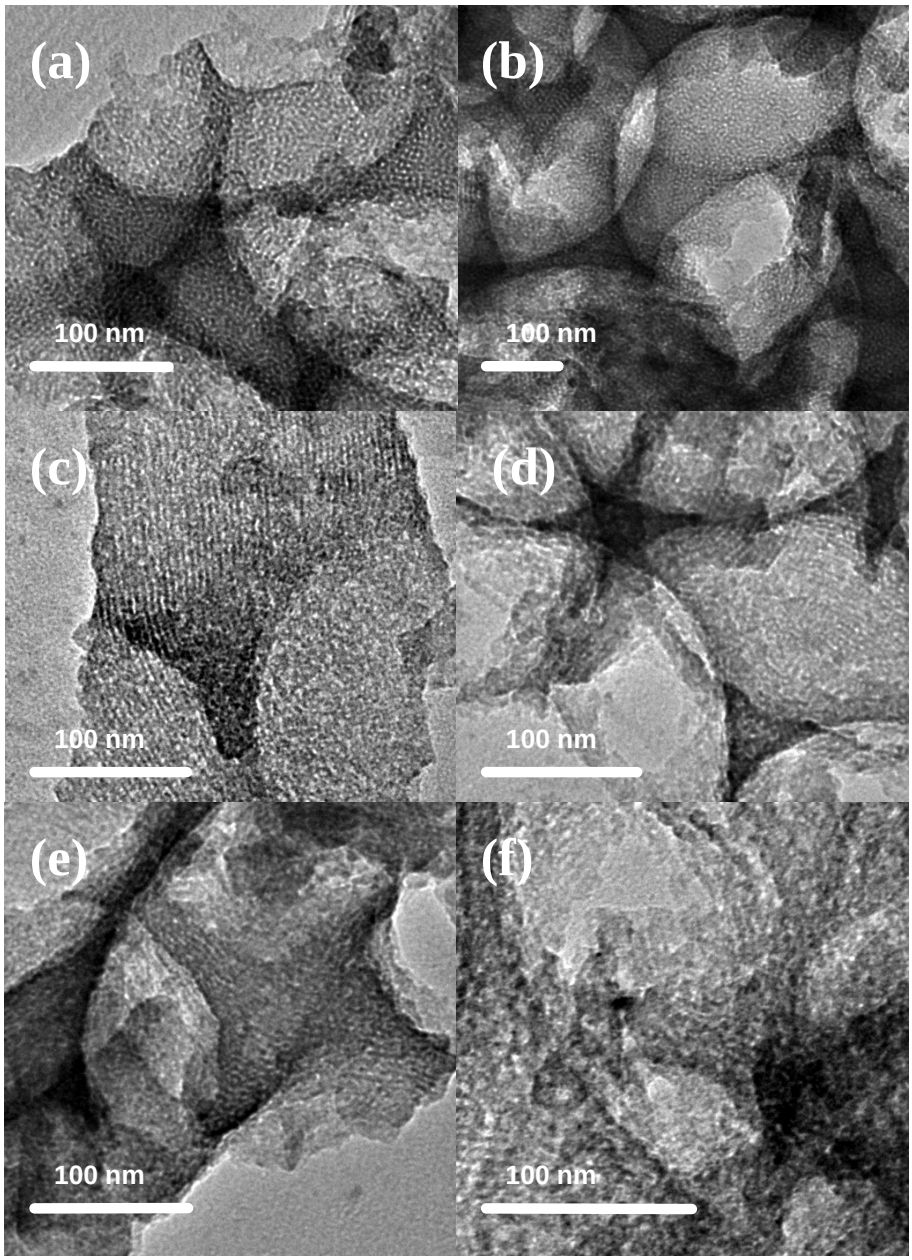

Figure 4.14: TEM images of meso/macro silica materials fabricated from a sol containing 12 g EtOH, 5 g TEOS, 3 g 0.5M HCl and (a) – 1g Brij 78 (*Sample B7^{10}*) , (b) – 2g Brij 78 (*B7^{11}*), (c) – 3g Brij 78 (*B7^{12}*) , (d) – 4g Brij 78 (*B7^{1}*) , (e) – 5g Brij 78 (*B7^{13}*) and (f) – 6g Brij 78 (*B7^{14}*). Materials were templated around a colloidal crystal comprising 346 nm PMMA spheres.

Although many of the samples are clearly mesoporous the mesophases are less distinct than those exhibited by the Brij 56 system. It is however clear that once again changing

the quantity of surfactant in the sol-gel mixture does alter the mesostructure of the final material. The samples prepared from relatively low surfactant concentrations appears to have pore walls with a wormhole structure (Sample B7[10-11], Figure 4.14 a & b). Increasing the quantity of surfactant in the reaction mixture resulted in materials with very poorly defined mesostructures. Sample B7[12,2,13 and 14] all had some regions with very disordered mesoporosity but they also had many regions with no porosity at all (Figures 4.14c-f).

Series 2 – Effect of TEOS concentration

Figure 4.15 shows typical SEM images from each sample in series 2.

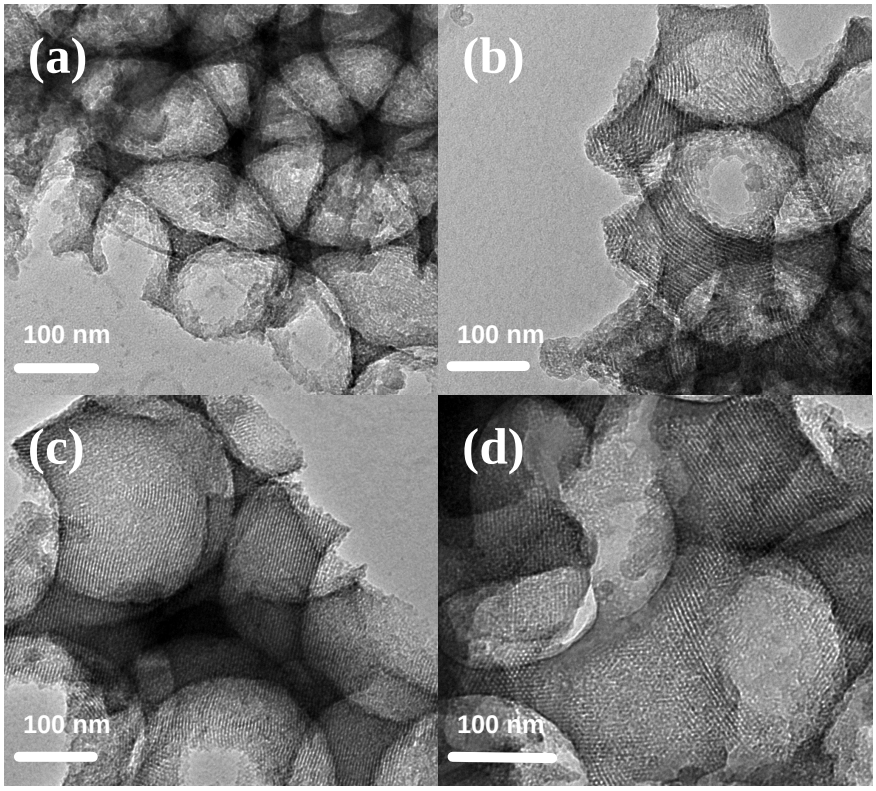

Figure 4.15: TEM images of meso/macro silica materials fabricated from a sol containing 12 g EtOH, 4 g Brij 78, 3 g 0.5M HCl and (a) – 5g TEOS (B7*[1]*) , (b) – 7g TEOS (B7*[2]*) (c) – 9g TEOS (B7*[3]*) and (d) – 13g TEOS (B7*[4]*). Materials were templated around a colloidal crystal comprising 346 nm PMMA spheres.

This series of preparations yielded samples with better defined mesoporous substructures and again it was noted that the final mesostructure was affected by the quantity of TEOS

that was incorporated into the initial sol. When only a small quantity of TEOS is used the final material had some small regions with disordered mesoporosity (Sample B7[1], Figure 4.15a) but was largely non-porous throughout. Increasing the amount of TEOS in the reaction mixture resulted in a marked improvement to the mesostructure of the final material with the sample having clearly ordered mesoporous pore walls (Sample B7[2], Figure 4.15b). Again this was evidenced by the observation of line structures in the TEM micrographs. Further increases in the quantity of TEOS also yielded materials with well-defined mesoporous pore walls with an ordered structure that resulted in a line pattern in the TEM micrographs (Samples B7[3-4], Figures 4.15 c & d).

Again it was postulated that the observed line pattern resulted from templating around a hexagonal mesophase which is consistent with the expected behaviour from the binary phase diagram.

This result can be rationalised by increased TEOS concentration promoting the formation of more curved mesostructures either by shielding the adsorbed surface charges on neighbouring surfactant head-groups or/and acting as a bridging species for the surfactant head-groups.

Series 3 – Effect of 0.5 M HCl concentration

Figure 4.16 shows a TEM image for each sample from series 3.

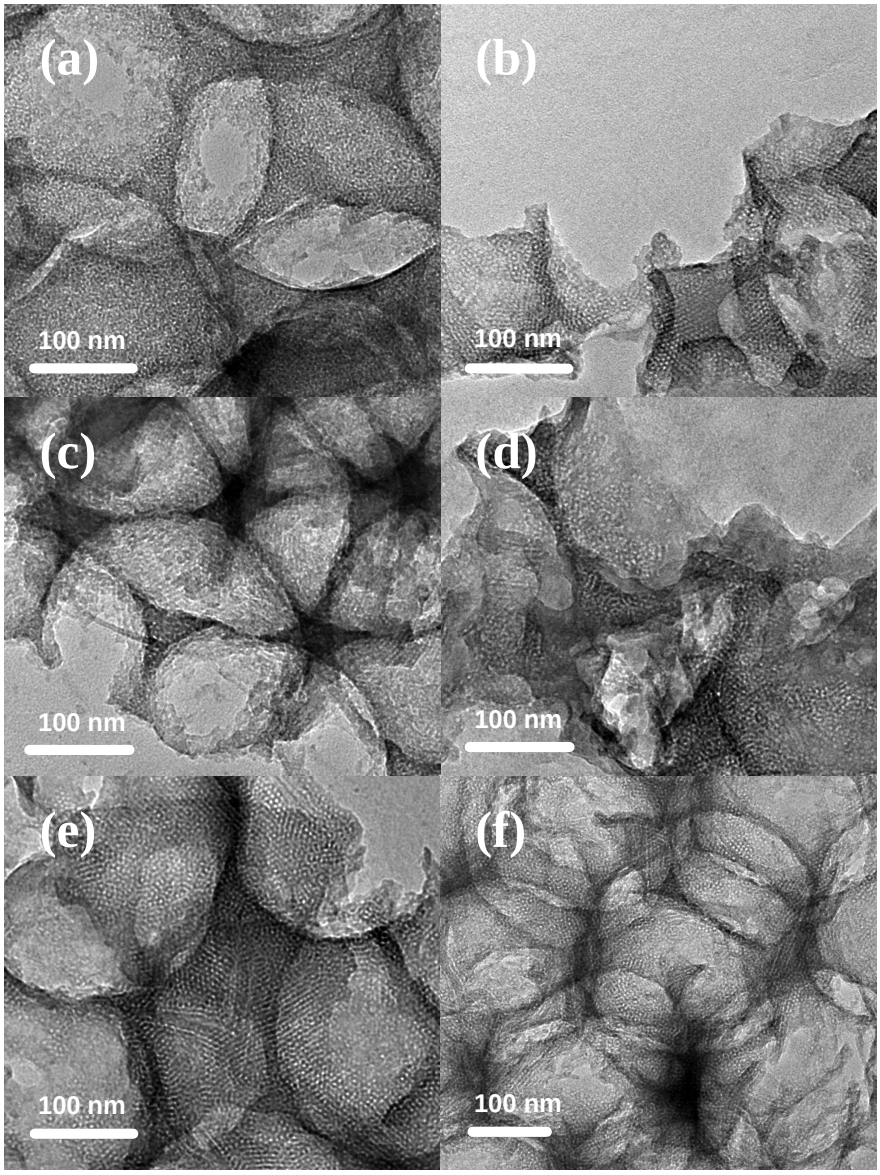

Figure 4.16: SEM images of meso/macro silica materials fabricated from a sol containing 12 g EtOH, 5 g TEOS, 4 g Brij 56 and (a) – 1 g 0.5M HCl (B7^5), (b) – 2 g 0.5M HCl (B7^6), (c) – 3 g 0.5M HCl (B7^2) , (d) – 4.5 g 0.5M HCl (B7^7), (e) – 7 g 0.5M HCl (B7^8) and (f) – 11 g 0.5M HC(B7^9). Materials were templated around a colloidal crystal comprising 346 nm PMMA spheres.

The quantity of 0.5 M HCl had a significant impact on the final mesoporous structure. The sample that was fabricated from the sol containing the smallest amount of 0.5 M HCl had distinct regions with both no-mesoporosity and disordered mesoporosity (Sample B7^5, Figure 4.16a). A small increase in HCl resulted in a sample with a much higher degree of

mesoporosity however the specific phase was indistinct and is best described as having the wormhole type morphology although some regions with an ordered line structure were also observed (Sample B7[6], Figure 4.16b). A further increase led to a significant degradation in the mesoporous structure. The materials typically having only a few regions of disordered porosity (Sample B7[2,7], Figure 4.16c & d). Finally, when a large quantity of 0.5 M HCl was used the mesoporous structure became more coherent with the samples mainly exhibiting a wormhole type mesoporous structures (Samples B7[8-9], Figure 4.16e & f), again there were still some small regions both with no-mesoporosity.

In summary the Brij 78 system yielded samples with mesostructures that were poorer defined than those samples fabricated using Brij 56 containing sol's. The mesopore morphology of this system could be broadly broken down into four regions, namely, line structure, wormhole, wormhole/line structure mixed phase and wormhole/non-porous mixed phase.

Of these four systems only the line structure mesoporosity is ordered and homogenous throughout the samples. Notably the best structures were formed when a high concentration of TEOS was used and examining compositional phase space further in the high TEOS regions would likely enable the synthesis of more ordered and coherent mesostructures.

In order to quantify the ordered line structure mesopores systems, the mesopore size and wall thickness were measured from a number of TEM images. The results of this study are presented in Table 4.5.

Sample	Pore morphology	Mesopore size /nm	Mesopore wall thickness/nm
4	Line structure	2.59 ± 0.29	2.50 ± 0.34
3	Line structure	2.57 ± 0.38	2.60 ± 0.38
2	Line structure	2.64 ± 0.46	2.54 ± 0.55

Table 4.5: **Table detailing the mesopore morphology, size and wall thickness for meso/macro samples fabricated using Brij 78 as the structure-directing agent for the mesophase.**

Both the mesopores size and wall thickness were consistent across the range of samples with an average mesopore size of 2.60 ± 0.41 nm. This represents a small increase on the pore size that was obtained when using Brij 56 as the structure directing agent (Typically ca 2.29 nm) reflecting the increased length of the surfactant and correspondingly the increased size of the subsequent micelles. The average wall thickness was 2.55 ± 0.42 nm and this is also slightly larger than the measured value for the materials synthesised from Brij 56.

The mesopore morphology of each sample was also entered into a ternary diagram revealing discreet compositional regions which resulted in samples with line structure, wormhole, wormhole/line structure mixed phase and wormhole/non-porous mixed phase. and these regions have also been highlighted in the ternary diagram (Figure 4.17).

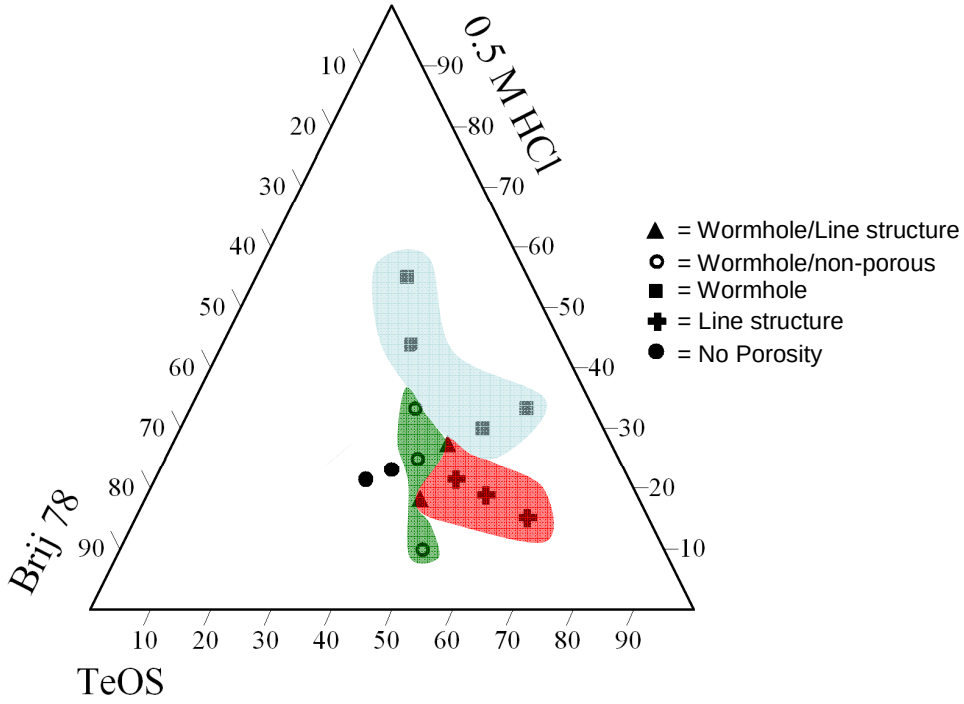

Figure 4.17: Ternary diagram showing the mesopores morphology of meso/macro silica's prepared from a solution containing Brij 78, 0.5 M HCl, TEOS and ethanol.

In a similar manner to Brij 56, the ternary diagram for Brij 78 has discrete compositional regions that exhibit mesophases with particular morphologies. Once again by carefully considering the relative ratios of the initial sol precursors it becomes possible to synthesise a final material with the desired mesostructure. Furthermore, the successful incorporation of Brij 78 into the synthesis resulted in a small increase in the mesopore size when compared to the materials synthesised from Brij 56. As such, this technique has been extended to enable the modification of not only the mesopore morphology but also the pore size.

b. CTAB

Cetyltrimethylammonium bromide (CTAB, chemical formula - $CH_3(CH_2)_{15}N(CH_3)_3Br$) is a cationic surfactant that has been extensively researched as a structure directing agent in the formation of mesoporous materials dating back to the first successful demonstration of liquid crystal templating as reported by the researchers at Mobil. Since then various methods involving CTAB as the structure directing agent[20, 21] in the formation of mesoporous materials have been reported including some dip-coating and spin-coating methods which follow the EISA mechanism [22, 23].

The binary phase diagram of CTAB is shown below in figure 4.18 and consists mainly of a large hexagonal region with cubic and lamellar regions occurring at higher weight percentages and temperatures.

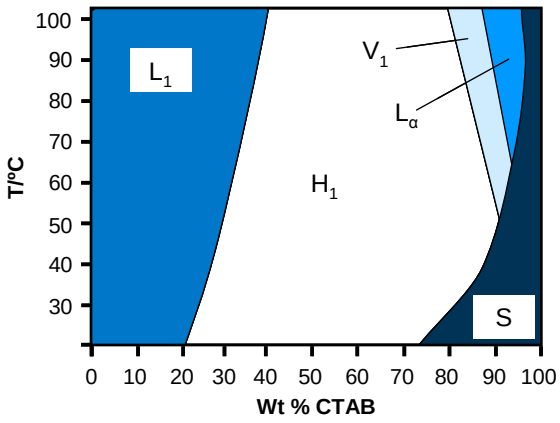

Figure 4.18: Binary phase diagram of CTAB in water[27].

Colloidal crystals were dipped from three silica sols whose composition is summarised in Table 4.6. Each preparation was kept constant in all respect except the incremental increase in the quantity of surfactant used in the initial sol.

Sample Ref	0.5 M HCl/g	EtOH/g	TEOS/g	CTAB/g
CTAB[1]	3	12	5	1
CTAB[2]	3	12	5	2
CTAB[3]	3	12	5	3

Table 4.6: Composition of reaction mixtures used to fabricate meso/macro silica using Brij 78 as the structure-directing agent for the mesophase.

Each sample was characterised by SEM and TEM. Figure 4.19 shows a typical SEM and TEM image from each sample.

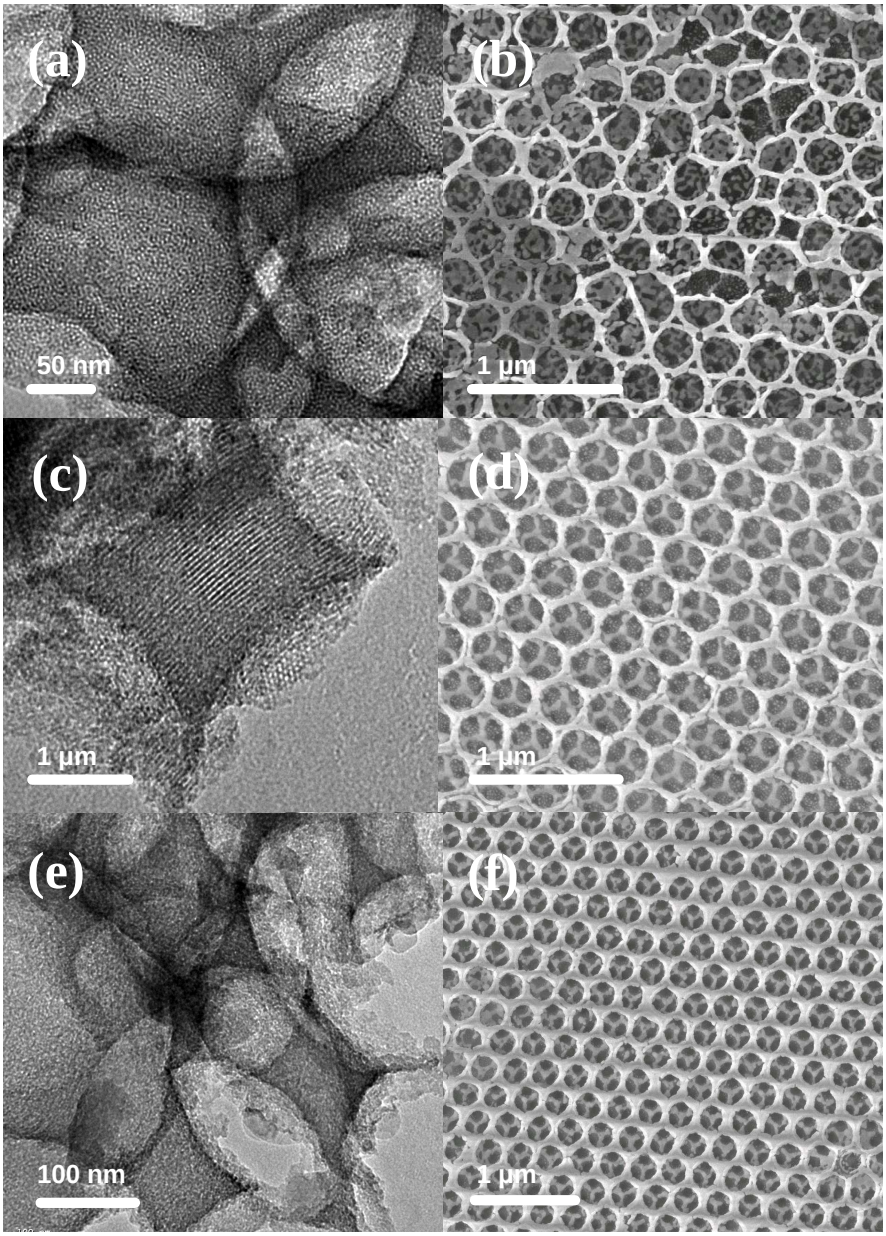

Figure 4.19: TEM and SEM images of a meso/macro silica material fabricated from a sol containing 12 g EtOH, 5 g TEOS, 3 g 0.5 M HCl and (a - b) 1 g CTAB (CTAB^1), (c - d) 2 g CTAB (CTAB^2) and (e - f) 3 g CTAB (CTAB^3). Materials were templated around a colloidal crystal comprising 346 nm PMMA spheres.

If we first consider the TEM images of the three samples, there is some mesostructuring of the macropore walls in all cases however each sample has a different mesopore structure.

Sample CTAB[1] was fabricated using the lowest surfactant concentrations and exhibits a wormhole structure (Figure 4.19a). A small increase in the surfactant concentration leads to an ordered line structure mesopore network (Sample CTAB[2], Figure 4.19c) whilst a further increase leads to the formation of a sample with extremely poorly defined disordered mesopores (Sample CTAB[3], Figure 4.19e).

This progression can not be adequately explained through the binary phase diagram of CTAB in water. This implies that the phase behaviour of the surfactant in this system is affected significantly by the incipient silica network, the acid concentration and the amount of ethanol.

Consideration of the SEM images of each sample on the other hand shows a less marked difference, however it is notable that the pore walls are seen to thicken as the quantity of surfactant used in the initial reaction mixture is increase. Again this is believed to be a direct result of increased surfactant leading to an increase in the viscosity of the dipping mixture.

The TEM images were used to measure average mesopore size and wall thickness whilst the SEM images were used to measure the macropore wall thickness and macropore centre to pore centre distance for each sample. From the macropore centre to centre distance the total volume shrinkage was also calculated and all these results are summarised below in Table 4.7.

		TEM (Mesopore sizes)		**SEM (Macropore sizes)**		
Sample	Mesopore Morphology	Pore Size/nm	Wall Thickness/nm	Pore Centre to Pore Centre/nm	Volume shrinkage/ %	Wall Thickness/nm
CTAB[1]	Wormhole	2.05 ± 0.35	1.72 ± 0.30	324.8 ± 6.1	17.3 ± 4.7	57.0 ± 13.1
CTAB[2]	Line Structure	1.95 ± 0.35	1.56 ± 0.31	304.1 ± 20.5	32.1 ± 14.7	53.1 ± 8.6
CTAB[3]	Wormhole/ non porous	N/A	N/A	325.3 ± 17.2	16.9 ± 13.9	63.7 ± 15.6

Table 4.7: **Table showing the average macropore and mesopore sizes for samples prepared from Ethanol, CTAB, TEOS and 0.5 M HCl reaction mixtures. Colloidal crystal templates were composed of 346 nm PMMA spheres.**

The average mesopore size was consistent for both samples CTAB[1] and CTAB[2] with an average mesopore size of 2.0 ± 0.35 nm. The average mesopore wall thickness was also in line for both samples with an average of 1.64 ± 0.31 nm. Both the mesopore size and wall thickness were smaller than those from the samples prepared by both Brij 56 and Brij 78 and again this is a reflection of the smaller size of the surfactant.

The macropore size on the other hand varied considerably between the three samples with sample CTAB[2] (ordered line structure) having a volume shrinkage that was almost double that of the other two samples. This observation is consistent with that observed for the Brij 56 system.

Finally all three samples were analysed by nitrogen adsorption and the BET surface area is summarised below in Table 4.8.

Sample Ref	Mesopore morphology	Surface area/ $m^2 g^{-1}$
CTAB[1]	Cubic	430.3
CTAB[2]	Hexagonal	544.1
CTAB[3]	Wormhole	378.9

Table 4.8: Table showing the surface area as measured by nitrogen adsorption BET analysis.

All three samples had a high surface area with sample CTAB[2] (ordered mesopores) having the highest which indicates that this mesoporous network was more coherent than the other two samples. Furthermore, the surface area of sample CTAB[2] was larger than the observed surface area for either of the Brij systems and this corresponds to CTAB producing the smallest mesopores.

As expected the sample with the most incoherent disordered mesopore morphology (CTAB[3]) had the lowest surface area and this is likely due to both pore blocking associated with the disordered mesostructure in conjunction with regions of the sample which had no mesoporosity.

c. F127

F127 is a non-ionic tri-block copolymer with the structural formula $EO_{106}PO_{70}EO_{106}$, where EO represents the ethylene oxide block and PO represents the propylene oxide block. The binary phase diagram of Pluronic F127 and water is presented below in Figure 4.20. The main feature of the phase diagram is the large micellar cubic phase (I_1), which is stable across a wide range of temperatures and compositions. The reason this surfactant has such a large cubic phase is due to its large head-group, which favours the formation of the highly curved spherical micelles.

Prior to the introduction of block copolymers as supramolecular templates, preparative methods to produce mesoporous media centred on the use of ionic surfactants such as CTAB, which severely limited the range of both the mesopore sizes and wall thickness' that were accessible. Interest in templating around block copolymers was driven by the desire to produce mesoporous materials with larger pore sizes and thicker walls without the need for swelling agents, which further complicate a fabrication.

Pluronic F127 was first reported as a structure directing agent in the production of mesoporous silica by Zhao et al[24]. Zhao's method centred on a precipitation based self-assembly method and was closely followed in 1998 with the report of a dip-coating EISA method to produce thin silica films using a variety of BC (Block-Copolymer) surfactants[25].

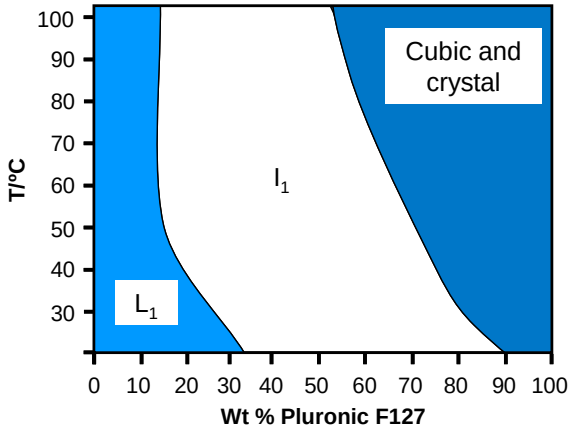

Figure 4.20: Binary phase diagram of F127 in water[26].

Due to the large range of pore sizes that would potentially be made available if BC polymers could be incorporated into the dual tempting technique a range of experiments were designed using F127 as the structure-directing agent. Three preparative methods were investigated each method was identical bar the quantity of F127 that was added to the initial reaction mixture. The precise composition of each reaction mixture is summarised below in Table 4.9:

Sample Ref	0.5 M HCl/g	EtOH/g	TEOS/g	F127/g
F^1	3	12	5	1
F^2	3	12	5	2
F^3	3	12	5	3

Table 4.9: Composition of reaction mixtures used to fabricate meso/macro silica using F127 as the structure-directing agent for the mesophase.

Each sample was subsequently characterised by both SEM and TEM. Figure 4.21 shows both a TEM and a SEM image taken from sample F^1.

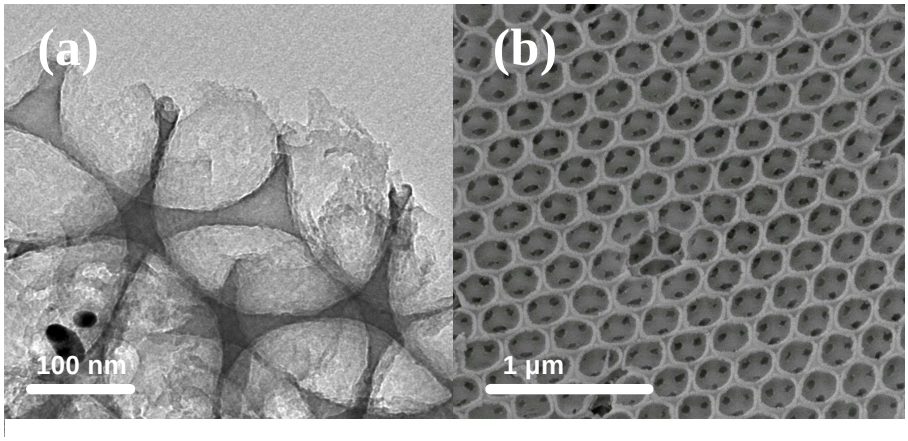

Figure 4.21: SEM and TEM images of a meso/macro silica material fabricated from a sol containing 1 g F127, 12 g EtOH, 5 g TEOS and 3 g 0.5 M HCl (Sample F^1). Materials were templated around a colloidal crystal comprising 295 nm PMMA spheres.

Sample F^1 was fabricated from the sol with the lowest surfactant concentration and resulted in a sample which, despite a few regions with some disordered mesoporosity, was largely non-porous (Figure 4.22a).

This suggests there was insufficient surfactant present in the reaction mixture. As such a homogenous mesophase is not formed within the voids of the colloidal crystal and the regions of porosity that are observe result from discrete surfactant rich regions. The macroporous structure on the other hand was very well ordered throughout.

Figure 4.22 shows typical SEM and TEM images of samples F^2 and F^3.

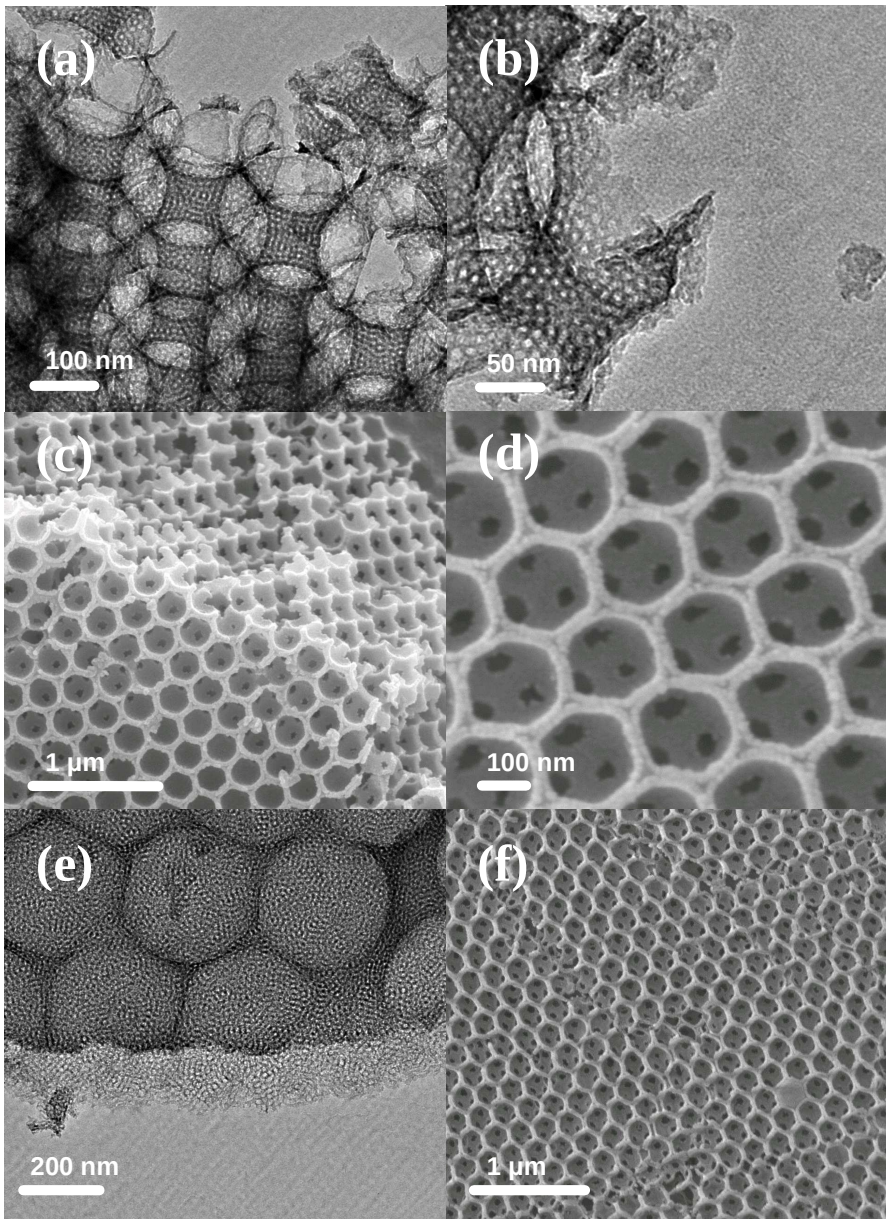

Figure 4.22: SEM and TEM images of a meso/macro silica material fabricated from a sol containing 12 g EtOH, 5 g TEOS and 3 g 0.5 M HCl and (a-d) 2 g F127 (*F²*) and (e-f) 3 g F127 (*F³*). Materials were templated around a colloidal crystal comprising either 346 (Images c and e) or 295 nm (Images a, b, d and f) PMMA spheres.

The increases in the quantity of F127 in the reaction mixture resulted in a considerable change to the mesoporosity of the final silica material. The TEM images clearly showed that the macropore walls were completely mesoporous throughout both samples. In both cases the mesostructure is clearly imparted from templating around spherical micelles. Furthermore, the mesopores were appreciably larger than those incorporated into the samples synthesised using Brij and CTAB as the structure directing agents. No line structures were observed for this system and this is due to the large head group which results in the surfactant almost exclusively forming highly curved spherical micelles. In both cases the macroporous framework was also extremely well ordered in three dimensions.

The ability to incorporate block copolymers into this dip infiltration based dual templating technique opens up the possibility to create much larger mesopores within the macroporous framework and further underlines the versatility of the technique.

The mesopore and macropore size and wall thickness was measured directly from a number of SEM and TEM images for each sample. These values are summarised in Table 4.10:

	TEM (Mesopore sizes)		**SEM (Macropore sizes)**		
Sample	Pore Size/nm	Wall Thickness/nm	Pore Centre to Pore Centre/nm	Volume shrinkage/%	Wall Thickness/nm
F[1]	N/A	N/A	281.9 ± 23.3	12.7 ± 23.5	56.6 ± 8.9
F[2]	6.86 ± 1.20	4.45 ± 0.73	241.5 ± 10.9	45.1 ± 7.8	41.7 ± 5.1
F[3]	7.37 ± 1.19	4.69 ± 0.79	237.1 ± 16.4	48.1 ± 11.5	44.9 ± 5.7

Table 4.10: Table showing both the average macropore and mesopore sizes for samples prepared fro F127 +TEOS + 0.5 M HCl mixtures. Colloidal crystal templates were composed of 296 nm PMMA spheres.

The mesopore size was measured at 6.86 and 7.37 nm representing a significant increase on the sizes of the mesopores reported previously in this chapter and significantly expands the size range of mesopores available through this method. The thickness of the mesopore walls was also considerably larger than the values reported when CTAB and Brij were used as the structure-directing agents.

Again the samples with mesoporous pore walls (Samples F^2 & F^3) were subject to a much greater degree of shrinkage than the sample with non-porous pore walls (F^1) with a volume shrinkage that was over three times larger.

A nitrogen adsorption and desorption isotherm was also collected for sample F^3 in order to accurately determine the surface area and mesopore size.

Both the isotherm and BJH pore size distribution plots are shown below in Figure 4.23:

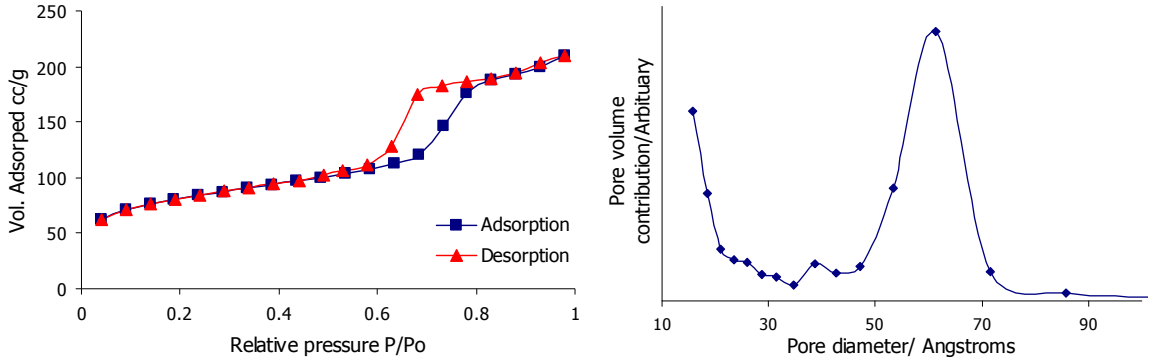

Figure 4.23: Nitrogen adsorption and desorption isotherm and BJH desorption pore size distribution for a meso/macro silica prepared from a sol containing 3 g F127, 12 g EtOH, 5 g TEOS and 3 g 0.5 M HCl. Materials were templated around a colloidal crystal comprising 346 nm PMMA spheres.

The nitrogen sorption isotherm is clearly type IV which is characteristic of mesoporous materials. The sharp jump in volume adsorbed that occurs at a relative pressure of about 0.65 of the adsorption branch of the isotherm corresponds to the pressure at which the nitrogen condenses into the mesopores and highlights the tight pore size distribution of the mesopores.

The tight distribution of mesopore sizes is further underlined by the presence of a H2 hysterisis loop, which is commonly associated with porous materials with narrow pore size distributions. The H2 hysteresis loop further evidences the presence of spherical mesopores in this material. The mechanisms behind the hysterisis loop are presented in the experimental chapter but in short it is related to capillary condensation taking place in the mesopores. Hysterisis loops are not normally observed for smaller pore sizes,

explaining the absence of a hysterisis loop in the previously reported nitrogen sorption isotherms.

Finally the BJH pore size distribution further confirms the tight pore size distribution of the mesopores in the sample with a sharp peak at 6.7 nm which is in excellent agreement with the values evaluated from the image analysis.

The BET surface area of the sample was measured at 248.7 m^2 g^{-1} which compares favourably with meso/macro materials prepared elsewhere in the literature. The surface area is smaller than those values reported previously in this chapter and this is simply a result of the increased pore size.

d. P123

The final surfactant that was investigated was P123. P123 is another tri-block copolymer with the general formula $EO_{20}PO_{68}EO_{20}$. The binary phase diagram (Figure 4.24) has a large hexagonal phase and a smaller cubic phase at a lower surfactant wt %. Both of these phases are only stable across a small range of temperatures and do not form below a temperature of about 30 °C.

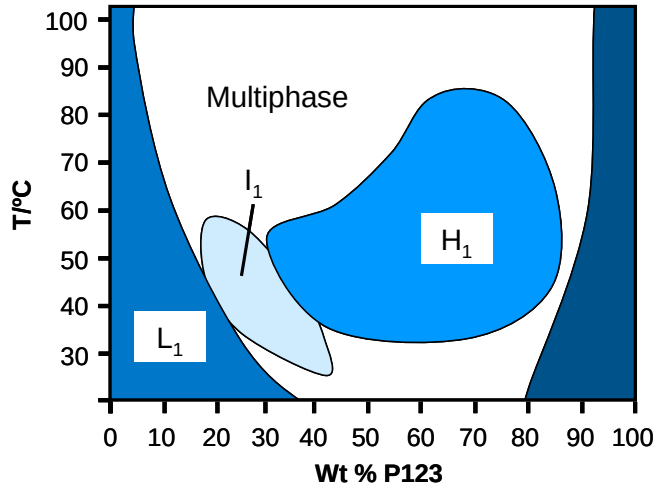

Figure 4.24: Binary phase diagram of P123 in water[26].

Two different reaction mixtures were used to fabricate meso/macro silicas. Both preparations differed only in the quantity of P123 that was incorporated into the initial sol gel mixture.

The precise composition of both these reaction mixtures is detailed in Table 4.11.

Sample Ref	0.5 M HCl/g	EtOH/g	TEOS/g	P123/g
P^1	3	12	5	1.2
P^2	3	12	5	2.9

Table 4.11: Composition of reaction mixtures used to fabricate meso/macro silica using P123 as the mesophase structure-directing agent.

Both samples were thoroughly investigated using both TEM and SEM.

Sample P^1 had a heavily distorted macropore structure and there was absolutely no evidence of any mesoporosity. Increasing the quantity of the surfactant in the sol however resulted in a sample with a distinct mesoporous structure within the macroporous framework.

Figure 4.25 below shows some typical TEM and SEM images from the sample P2.

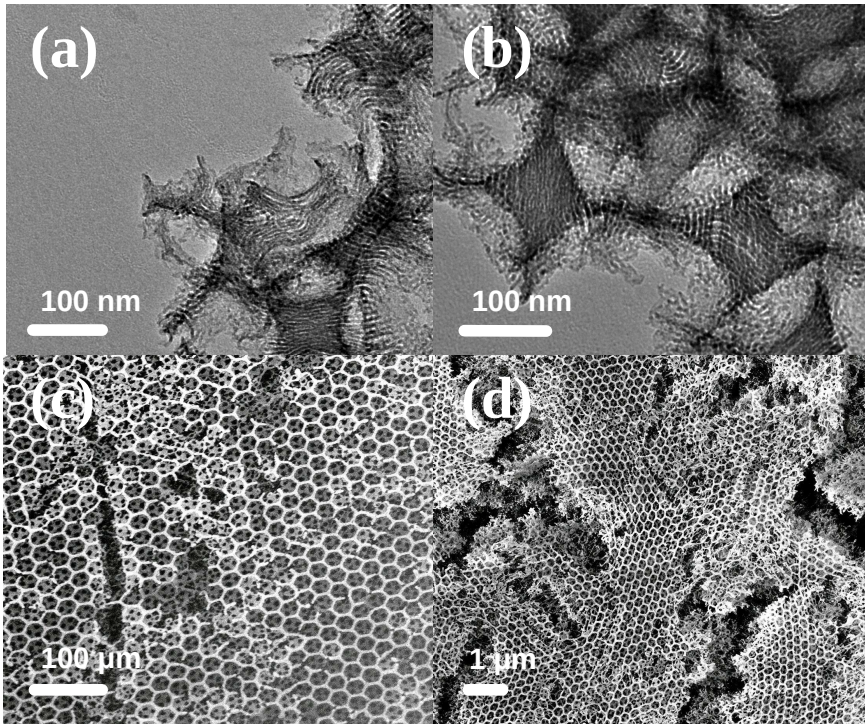

Figure 4.25: TEM and SEM images of a meso/macro silica material fabricated from a sol containing 12 g EtOH, 5 g TEOS, 2.9 g P123 and 3 g 0.5 M HC. Materials were templated around a colloidal crystal comprising 346 nm PMMA spheres.

The TEM images show that the macropore walls consist of a multimodal meso-architecture with regions exhibiting both wormhole type mesoporosity and some areas adopting what appear to be lamellar type silicate sheets.
Although the 3D macroporous structure is again clearly evident in the SEM images the samples were heavily distorted encompassing large tears throughout. The mesoporous lamellar structure exhibited by the macropore walls may account for the large number of defects present in the macroporous framework as this type of mesoporosity would be expected to significantly compromise the mechanical strength of the macrostructure leading to tearing and distortion of the macroporous framework.

e. Summary

To summarise the effect the chemical structure of the surfactant has on the final materials the characteristic pore dimensions, morphologies and surface area measurements for all the different systems are tabulated below in Table 4.12:

Surfactant	Mesopore morphology	BET Pore size/ nm	TEM Pore size/nm	SEM Pore Size/nm	Volume shrinkage	Surface area/ m^2 g^{-1}
Brij 56	Line structure	2.3	2.3	294.9	38.1	517.6
	Wormhole	N/A	2.2	312.9	26.0	225.6
F127	Spherical mesopores	6.6	7.1	239.3	46.6	248.7
Brij 78	Line structure	N/A	2.6	N/A	N/A	424.2
	Wormhole	N/A	N/A	N/A	N/A	N/A
CTAB	Line structure	N/A	2.0	304.1	32.1	523.5
	Wormhole	N/A	2.1	324.8	17.3	430.3
	Disordered	N/A	N/A	325.3	16.9	378.9
P123	Disordered/ Lamellar	N/A	N/A	N/A	N/A	N/A

Table 4.12: Table summarising the meso and macro pore sizes and wall thickness for various surfactants.

In all cases the surface area was well above what would be expected for a macroporous silica system. The mesopore sizes and the morphologies of the mesostructures obtained were directly related to the size of the surfactant that was used in the synthesis. The range of mesopore sizes that were synthesised was 2 - 7.1 nm with spherical, line structure, disordered and lamellar type structure observed. Similarly, the surface areas could be directly linked to the size of the surfactant with the large F127 BC surfactant

having the smallest surface area whilst the smallest surfactant (CTAB) resulted in the largest surface area.

The choice of surfactant also has interesting ramifications on the final macropore structure with the volume shrinkage being related to both the size of the mesopores and the mesopore structure. Firstly it was noted that the larger mesopores resulted in the greatest volume shrinkage with F127 derived structures shrinking the most and CTAB derived structures the least. Secondly, materials with ordered line structure mesopores were prone to greater shrinkage than those with wormhole mesoporosity, which in turn shrank more than the non-porous samples.

4.3.3 Ethanol

So far the effect the quantity of ethanol added to the initial sol has on the final material has been neglected. The primary function of the ethanol is to dilute the reaction precursors such that they are able to infiltrate the colloidal crystal. After this the ethanol evaporates preferentially, driving the mesophase formation.

In order to fully investigate the effect the quantity of ethanol in the reaction mixture has on the final meso/macro silica a series samples were synthesised each using identical preparative methods bar the quantity of ethanol.

In all cases F127 was used as the structure-directing agent and the precise composition of each reaction mixture is detailed below in Table 4.13.

Sample Ref	0.5 M HCl/g	EtOH/g	TEOS/g	F127/g
Eth[1]	3	3	5	2.5
Eth[2]	3	6	5	2.5
Eth[3]	3	9	5	2.5
Eth[4]	3	12	5	2.5
Eth[5]	3	15	5	2.5

Table 4.13: **Composition of reaction mixtures used to fabricate meso/macro silica using F127 as the structure-directing agent for the mesophase and varying the quantity of ethanol with which each sol was diluted.**

Mesostructure

Each sample was observed in a TEM and a typical image for each sample is shown below in Figure 4.26.

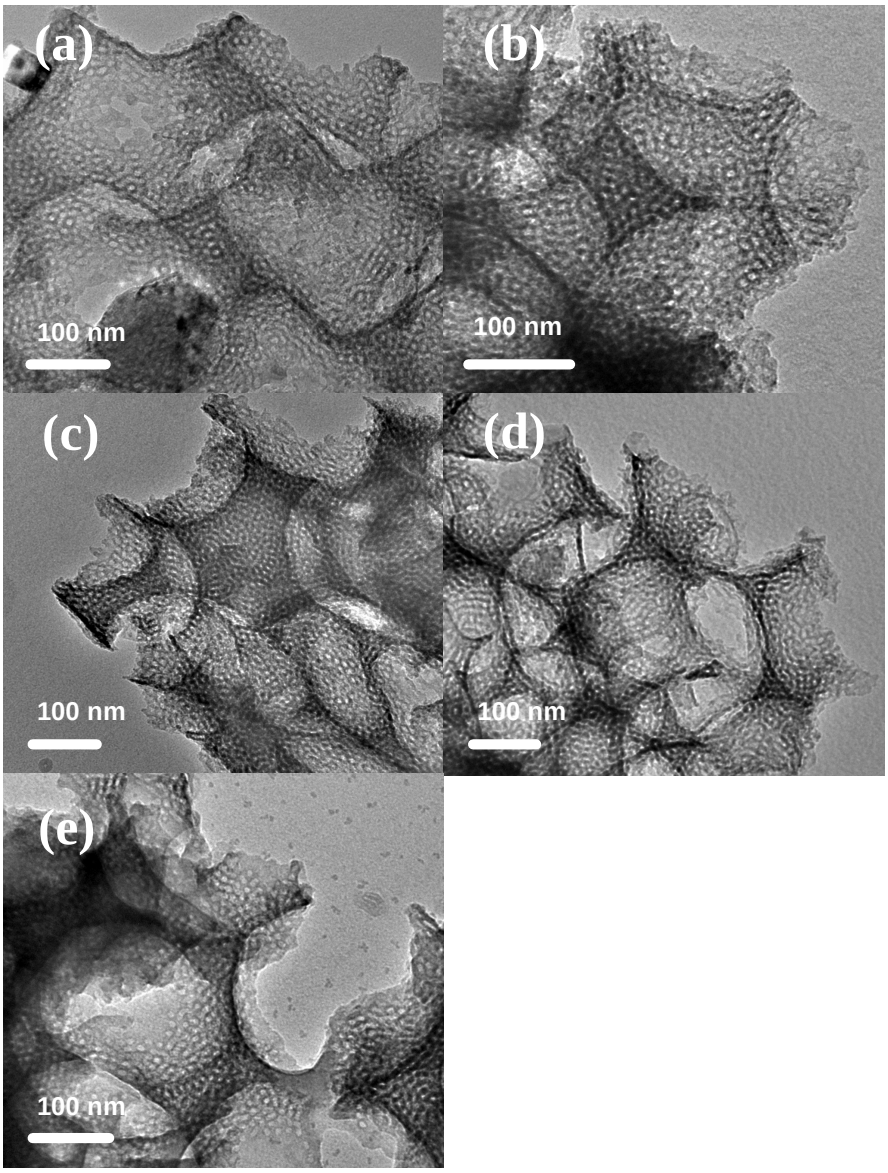

Figure 4.26: TEM images of meso/macro silica materials fabricated from a sol containing 2.5 g F127, 5 g TEOS, 3 g 0.5M HCl and (a) – 3 g ethanol (Eth^1) , (b) – 6g ethanol (Eth^2) (c) – 9 g ethanol (Eth^3), (d) – 12 g ethanol (Eth^4) and (e) – 15 g ethanol (Eth^5). Materials were templated around a colloidal crystal comprising 346 nm PMMA spheres.

All five samples were homogeneously mesoporous regardless of the quantity of ethanol that was used in the preparation. This indicates the ethanol does not play affect the mesophase formation and suggests, as already postulated, that the sole function played by the ethanol is to dilute the initial sol-gel mixture prior to it's preferential evaporation.

Macrostructure

All five samples were also observed in a SEM and a typical SEM micrograph of each sample is shown below in Figure 4.27.

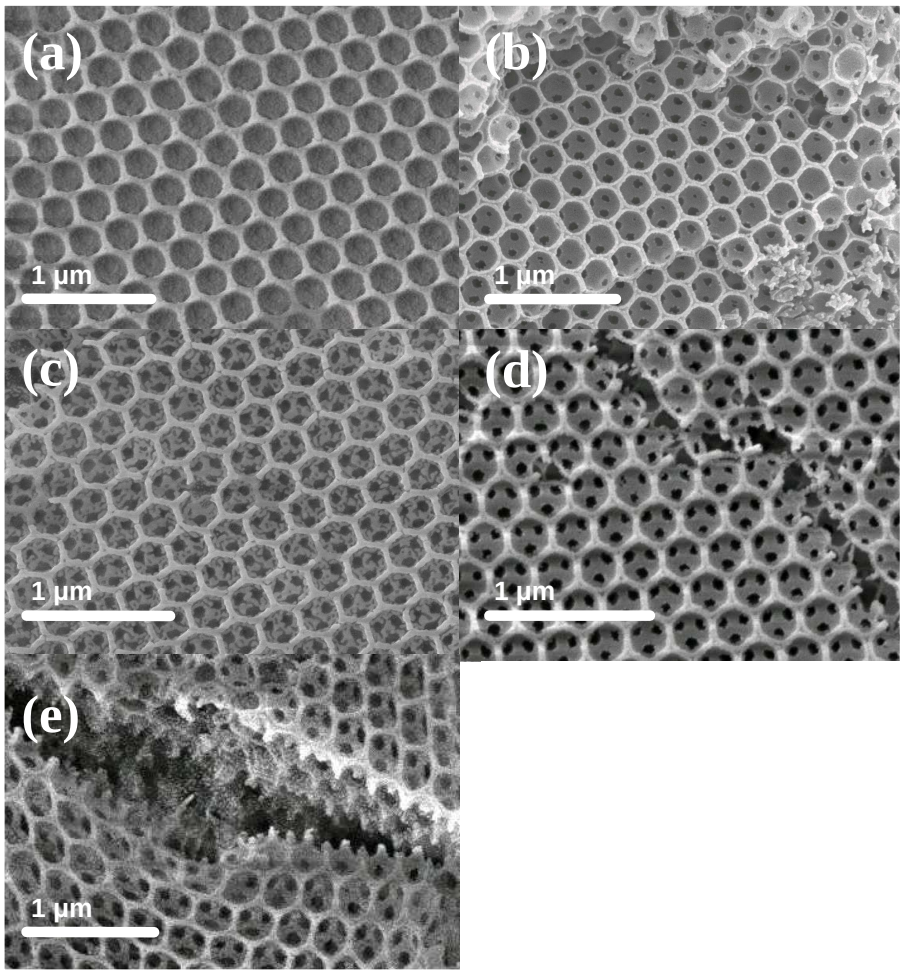

Figure 4.27: SEM images of meso/macro silica materials fabricated from a sol containing 2.5 g F127, 5 g TeOS, 3 g 0.5M HCl and (a) – 3 g ethanol (Eth^1), (b) – 6g ethanol (Eth^2) (c) – 9 g ethanol (Eth^3), (d) – 12 g ethanol (Eth^4) and (e) – 15 g ethanol (Eth^5). Materials were templated around a colloidal crystal comprising 346 nm PMMA spheres.

As shown all five samples had a well-defined macroporous structures. However, it was observed that the preparation with the largest quantity of ethanol yielded a sample that was prone to a much larger degree of tears and distortion than the other four samples. This is likely due to over-dilution of the sol-gel reaction mixture resulting in the deposition of insufficient silica species to satisfactorily fill the voids of the colloidal crystal.

The pore sizes and wall thicknesses of both the macro and meso-structure were measured directly from the SEM and TEM images and the average values are summarised in Table 4.14 below:

		TEM (Mesopore sizes)		**SEM (Macropore sizes)**	
Sample	Pore Size/nm	Wall Thickness/nm	Pore Centre to Pore Centre/nm	Volume shrinkage/%	Wall Thickness/nm
Eth[1]	8.00 ± 0.97	6.13 ± 0.98	297.2 ± 16.3	25.6 ± 11.0	60 .1 ± 8.4
Eth[2]	8.53 ± 0.70	5.81 ± 0.95	288.5 ± 11.0	35.1 ± 6.9	51 .2 ± 5.4
Eth[3]	7.41 ± 0.80	4.75 ± 0.88	278.6 ± 15.2	38.8 ± 9.0	50. 2 ± 7.8
Eth[4]	7.36 ± 1.22	5.38 ± 0.89	275.1 ± 8.7	44.8 ± 4.9	48.4 ± 5.6
Eth[5]	7.46 ± 0.96	4.85 ± 1.19	Heavily distorted macropores		

Table 4.14: Each sol contained 2.5 g F127, 3 g 0.5M HCl and 5 g TeOS and was diluted with the specified quantity of ethanol. All measurements were calculated by image analysis from at least 10 images from each sample. All samples were fabricated around a colloidal crystal comprising monodisperse 346 nm spheres.

The mesopores appear to become smaller when increased quantities of ethanol are added to the initial sol and this also appears to be accompanied by a thinning of the pore walls, however this result is by no means conclusive with large errors arising due to the difficulty in accurately measuring the mesopores.

The macroporous structure does however provide a more convincing pattern as increasing the ethanol concentration results in a reduction in both the pore centre to pore centre distance and the wall thickness until finally we reach a situation where the macroporous structure begins to break down. This is an intuitive result as increasing the dilution of the sol serves to reduce the quantity of silica species which infiltrates into the voids of the colloidal crystal Thus when the template is removed there is more shrinkage as there is simply less material remaining in the voids of the template. When the sol is over-diluted the lack of material compromises the mechanical strength of the macrostructure (Figure 4.27e).

4.4 Conclusions

The formation of hierarchically ordered meso-macro silica materials has been demonstrated using a simple dual templating method. The mechanism involves dip-coating a colloidal crystal into a reaction mixture containing EtOH, TEOS, 0.5M HCl and surfactant. In some cases both the mesopore and macropore systems are highly ordered and interconnected and the final materials have well characterised pore systems and high surface areas.

A critical study of the reaction constituents has shown that the final mesophase can be tuned in terms of both morphology and pore size by judicious selection of surfactant and the subsequent reaction mixture composition. Furthermore, the periodicity of the macropores can be tuned by selecting the appropriately sized PMMA microspheres. As such this technique makes it possible to synthesise a large range of materials with highly ordered hierarchical meso/macro architectures specifically tailored for any particular application.

It is postulated that the mesophase formation occurs in a manner analogous to the evaporation induced self assembly mechanism reported by Brinker et al[27] for the production of mesoporous films. The power of this technique is that it enables the direct fabrication of materials with highly ordered mesopore systems and tight pore size distributions. Furthermore, the technique realises the possible to predictably synthesis materials with desired mesopore sizes and morphologies.

Previously reported methods have been limited in terms of the morphology and ordering of the final mesopore size and structure and have lacked the predictability and versatility of the dip-infiltrated dual templating mechanism developed during the course of this thesis.

4.6 References

(1) Yuan, Z.-Y.; Su, B.-L., Insights into hierarchically meso-macroporous structured materials. *Journal of Materials Chemistry* **2006,** 16, (7), 663-677.

(2) Ho, C.; Yu, J. C.; Wang, X.; Lai, S.; Qiu, Y., Meso- and macro-porous Pd/CexZr1-xO2 as novel oxidation catalysts. *Journal of Materials Chemistry* **2005,** 15, (22), 2193-2201.

(3) Liu, S.; Kong, L.; Yan, X.; Li, Q.; He, A., Synthesis of hierarchically structured MCM-41 with high hydrothermal stability and its application in environmental catalysis. *Studies in Surface Science and Catalysis* **2005,** 156, (Nanoporous Materials IV), 379-384.

(4) Lebeau, B.; Fowler, C. E.; Mann, S.; Farcet, C.; Charleux, B.; Sanchez, C., Synthesis of hierarchically ordered dye-functionalized mesoporous silica with macroporous architecture by dual templating. *Journal of Materials Chemistry* **2000,** 10, (9), 2105-2108.

(5) Sen, T.; Tiddy, G. J. T.; Casci, J. L.; Anderson, M. W., One-pot synthesis of hierarchically ordered porous-silica materials with three orders of length scale. *Angewandte Chemie, International Edition* **2003,** 42, (38), 4649-4653.

(6) Sen, T.; Tiddy Gordon, J. T.; Casci John, L.; Anderson Michael, W., One-pot synthesis of hierarchically ordered porous-silica materials with three orders of length scale. *Angewandte Chemie (International ed. in English)* **2003,** 42, (38), 4649-53.

(7) Yang, P.; Deng, T.; Zhao, D.; Feng, P.; Pine, D.; Chmelka, B. F.; Whitesides, G. M.; Stucky, G. D., Hierarchically ordered oxides. *Science (Washington, D. C.)* **1998,** 282, (5397), 2244-2247.

(8) Shin, Y.; Liu, J.; Wang, L.-Q.; Nie, Z.; Samuels, W. D.; Fryxell, G. E.; Exarhos, G. J., Ordered hierarchical porous materials: towards tunable size- and shape-selective microcavities in nanoporous channels. *Angewandte Chemie, International Edition* **2000,** 39, (15), 2702-2707.

(9) Huang, L.; Wang, Z.; Wang, H.; Sun, J.; Li, Q.; Zhao, D.; Yan, Y., Hierarchical porous structures by using zeolite nanocrystals as building blocks. *Microporous and Mesoporous Materials* **2001,** 48, (1-3), 73-78.

(10) Kuang, D.; Brezesinski, T.; Smarsly, B., Hierarchical Porous Silica Materials with a Trimodal Pore System Using Surfactant Templates. *Journal of the American Chemical Society* **2004,** 126, (34), 10534-10535.

(11) Maekawa, H.; Esquena, J.; Bishop, S.; Solans, C.; Chmelka, B. F., Meso/macroporous inorganic oxide monoliths from polymer foams. *Advanced Materials (Weinheim, Germany)* **2003,** 15, (7-8), 591-596.

(12) Carn, F.; Colin, A.; Achard, M.-F.; Deleuze, H.; Sellier, E.; Birot, M.; Backov, R., Inorganic monoliths hierarchically textured via concentrated direct emulsion and micellar templates. *Journal of Materials Chemistry* **2004,** 14, (9), 1370-1376.

(13) Grosso, D.; Cagnol, F.; Soler-Illia, G. J. D. A. A.; Crepaldi, E. L.; Amenitsch, H.; Brunet-Bruneau, A.; Bourgeois, A.; Sanchez, C., Fundamentals of mesostructuring through evaporation-induced self-assembly. *Advanced Functional Materials* **2004,** 14, (4), 309-322.

(14) Crepaldi, E. L.; de, A. A. S.-I. G. J.; Grosso, D.; Albouy, P. A.; Sanchez, C., Design and post-functionalisation of ordered mesoporous zirconia thin films. *Chemical communications (Cambridge, England)* **2001**, (17), 1582-3.

(15) Fan, H.; Brinker, J., Evaporation-induced self-assembly to functional nanostructures. *Studies in Surface Science and Catalysis* **2004,** 148, (Mesoporous Crystals and Related Nano-Structured Materials), 213-240.

(16) Brinker, C. J., Evaporation-induced self-assembly. Functional nanostructures made easy. *MRS Bulletin* **2004,** 29, (9), 631-640.

(17) Coleman, N. R. B.; Attard, G. S., Ordered mesoporous silicas prepared from both micellar solutions and liquid crystal phases. *Microporous and Mesoporous Materials* **2001,** 44-45, 73-80.

(18) Zhao, D.; Huo, Q.; Feng, J.; Chmelka, B. F.; Stucky, G. D., Nonionic triblock and star diblock copolymer and oligomeric surfactant syntheses of highly ordered, hydrothermally stable, mesoporous silica structures. *Journal of the American Chemical Society* **1998,** 120, (24), 6024-6036.

(19) El-Safty, S. A.; Hanaoka, T., Monolithic nanostructured silicate family templated by lyotropic liquid-crystalline nonionic surfactant mesophases. *Chemistry of Materials* **2003,** 15, (15), 2892-2902.

(20) Attard, G. S.; Glyde, J. C.; Goltner, C. G., Liquid-crystalline phases as templates for the synthesis of mesoporous silica. *Nature (London)* **1995,** 378, (6555), 366-8.

(21) Boonamnuayvitaya, V.; Tayamanon, C.; Sae-Ung, S.; Tanthapanichakoon, W., Synthesis and characterization of porous media produced by a sol-gel method. *Chemical Engineering Science* **2006,** 61, (5), 1686-1691.

(22) Lu, Y.; Ganguli, R.; Drewien, C. A.; Anderson, M. T.; Brinker, C. J.; Gong, W.; Guo, Y.; Soyez, H.; Dunn, B.; Huang, M. H.; Zink, J. I., Continuous formation of supported cubic and hexagonal mesoporous films by sol-gel dip-coating. *Nature (London)* **1997,** 389, (6649), 364-368.

(23) Grosso, D.; Balkenende, A. R.; Albouy, P. A.; Lavergne, M.; Mazerolles, L.; Babonneau, F., Highly oriented 3D-hexagonal silica thin films produced with cetyltrimethylammonium bromide. *Journal of Materials Chemistry* **2000,** 10, (9), 2085-2089.

(24) Zhao, D.; Feng, J.; Huo, Q.; Melosh, N.; Frederickson, G. H.; Chmelka, B. F.; Stucky, G. D., Triblock copolymer syntheses of mesoporous silica with periodic 50 to 300 angstrom pores. *Science (Washington, D. C.)* **1998,** 279, (5350), 548-552.

(25) Zhao, D. Y.; Yang, P. D.; Melosh, N.; Feng, Y. L.; Chmelka, B. F.; Stucky, G., Continuous mesoporous silica films with highly ordered large pore structures. *Advanced Materials (Weinheim, Germany)* **1998,** 10, (16), 1380-1385.

(26) Wanka, G.; Hoffmann, H.; Ulbricht, W., Phase Diagrams and Aggregation Behavior of Poly(oxyethylene)-Poly(oxypropylene)-Poly(oxyethylene) Triblock Copolymers in Aqueous Solutions. *Macromolecules* **1994,** 27, (15), 4145-9.

(27) Brinker, C. J.; Lu, Y.; Sellinger, A.; Fan, H., Evaporation-induced self-assembly. Nanostructures made easy. *Advanced Materials (Weinheim, Germany)* **1999,** 11, (7), 579-585.

(28) Coleman, N., Direct liquid crystal templating of mesoporous silica and platinum. *PhD Thesis. University of Southampton*, **2001.**

Chapter 5

Contents page

HIERARCHICALLY ORDERED MESO/MACRO NON SILCIA MATERIALS

CHAPTER 5 – Hierarchically ordered meso/macro non silica materials

5.1 Introduction

To date, the majority of studies detailing nanoporous materials concern silica and silica based materials. The reason for this bias is twofold. Firstly, the pioneering work in nanoporous materials can be traced back to zeolitic work. Secondly, the chemistry of the silicon precursors is much simpler and better understood than that of their transition metal counterparts[1]. In contrast to silica sol-gel chemistry, transition metal precursors tend to be more reactive, present different oxidation states and co-ordination and also tend to crystallise when heated. Therefore, the coupling of transition metal sol-gel chemistry with the template directed approach tends to present a more complex proposition.

Despite these difficulties, a number of research groups have investigated synthetic pathways to non-silica nanoporous materials [2, 3] and this is driven by their potential in a diverse number of fields such as catalysis, separation, optics and smart coatings. For many of these applications an hierarchically ordered meso-macro structure would be advantageous as it would combine the large open pore network of a macroporous materials with the inherently high surface area of a mesoporous material.

A number of synthetic strategies have been reported to synthesis both mesoporous and macroporous non-silica materials and in many cases these strategies are analogous to strategies used to synthesise nanoporous silica materials through template directed approaches. There are even a few publications detailing routes towards non-silica hierarchical meso-macro materials[4, 5]. These techniques commonly follow a dual templating technique using a supramolecular template for the mesophase and a macrotemplate such as a colloidal crystal[6], emulsion[7] or bio-template for the macrostructure.

Using these techniques non-silica meso-macro materials such as TiO_2, ZrO_2 and CeO_2 have been prepared. To date, however, at best only one of the pore systems is ordered, limiting the interconnectivity of the materials and their effectiveness in a number of applications.

The previous Chapter described a versatile route to the formation of hierarchically ordered meso/macro silica materials. This Chapter describes how those ideas and techniques were extended and applied to the production of hierarchically ordered non-silica materials, including TiO_2 and ZrO_2. Attempts were also made to fabricate hierarchically ordered platinum using a similar synthetic strategy.

5.2 Experimental

The experimental details presented below give a brief overview of the synthetic procedures adopted during the course of this chapter. Section one gives the procedure adopted to fabricate the colloidal crystal templates, section two and three detail the procedure used for preparing the dipping mixtures whilst the fourth section gives the procedure used to fabricate the meso/macro material. Finally the fifth section describes the different characterisation methods that were used in this chapter.

5.2.1 Assembly of the colloidal templates

The colloidal crystal templates were assembled by a simple sedimentation method as described below. Microscope slides were precleaned by sequential sonication in water, acetone, isopropyl alcohol and chloroform before a Teflon ring (Internal diameter - 10 mm, Ext. dia. - 20 mm, thickness - 10 mm) was attached by double sided tape. 0.3 ml of the monodisperse suspension of PMMA spheres diluted with water to 1-wt % was confined within the Teflon ring. The water was then allowed to evaporate at room temperature over about 2-3 days. After all the water had evaporated the Teflon ring was removed exposing a circular iridescent packed array of polystyrene spheres on the substrate. This approach formed uniform films of 40 μm thickness.
For the preparation of samples for analysis in the Gemini surface area analyser a large scale up was required. In this case a larger Teflon ring (Internal diameter ~ 100 mm, ext. dia. 10 mm, thickness 10 mm) and was adhered to a large glass plate. 7 ml of the 1 wt % monodisperse PMMA sphere solution was confined within the ring and was then allowed to evaporate at room temperature over 2-3 days. This process gave rise to samples that were only partly iridescent reflecting the poor ordering of the colloidal crystal.

5.2.2 Preparation of TiO_2 and ZrO_2 reaction mixtures

All three dipping solutions were prepared in the same general manner. Initially surfactant (Pluronic F127, BASF) was dissolved in ethanol by gentle heating prior to the drop-wise addition of the appropriate metal alkoxide ($TiCl_4$, $ZrCl_4$) on ice. This solution was then stirred whilst water was added dropwise. This solution was then left stirring at room temperature for 3 days.

5.2.3 Preparation of Pt reaction mixture

Initially surfactant (Pluronic F127, BASF) was dissolved in ethanol by gentle heating prior to the addition hexachloroplatinic acid. This solution was then stirred whilst water was added drop-wise. This solution was then left stirring at room temperature for 3 days.

5.2.4 Fabrication of meso/macro films by dip coating

The crystalline template adhered to the glass substrate was immersed vertically into the sol, at a rate of 150 mm min^{-1}, before immediately withdrawing at 50 mm min^{-1}. Due to capillary forces the sol infiltrates the interstitial voids of the template. The sample was dried at room temperature for 24 hours allowing gelation of the sol. Finally the template was removed by heating the sample to 350 °C in air at a rate of 0.9 °C min^{-1}. This temperature was maintained for 600 minutes before slowly cooling over 16 hours.

5.2.5 Characterisation

An analytical scanning electron microscope (JSM-6500F) was used to characterise the materials. The TiO_2 and ZrO_2 materials were non-conductive and as such were coated with a thin layer of gold (ca ~ 20 nm) prior to topographical observation in the SEM. The samples were also analysed in a transmission electron microscope (JEOL 3010) allowing the direct observation of the materials mesostructure. The samples were prepared as outlined in the experimental section on page 56.
A Nitrogen absorption/desorption isotherm was also collected for the titania samples using a Gemini 2375 BET surface area analyser.

4.4 Results

Attempts were made to fabricate hierarchically ordered meso/macro titania, zirconia and platinum materials. The methodology in all cases involved the dip infiltration of a colloidal crystal comprising monodisperse PMMA spheres with a reaction mixture composed of water, metal precursor (Ti, Zr or Pt), surfactant and ethanol. It is assumed that initially the reaction mixture completely fills the interstitial voids of the colloidal crystal via capillary action. Subsequently preferential ethanol evaporation drives the formation of a mesophase. A metal framework is then formed around both the surfactant mesophase and colloidal crystal framework. Finally, heat treatment removes both the colloidal crystal template and the surfactant molecules yielding a macroporous framework with mesoporous pore walls.

Initially work focussed on the fabrication of hierarchically ordered meso/macro titania using a variety of dipping mixtures. Before extending the range of materials further with attempts to synthesise meso/macro zirconia and platinum.

4.3.2 Hierarchically ordered meso/macro Titania

Titania has been intensively investigated on account of its unique electronical and optical properties[8, 9]. Combining these properties with a hierarchically ordered meso/macro structure could provide novel materials that might be exploited in a diverse range of applications such as catalysis, photonic crystals, photoconductors, as electrodes in a lithium battery or in photovoltaics[10-13].

Titanium dioxide is the most widely used photocatalyst because of its strong redox power and high photo-corrosion resistance and it is this application that has fuelled a great deal of the work done in the field of nanoporous titania. Non-porous photo-catalysts tend to suffer from limited light penetration resulting in poor photo-activity. To this end a meso/macro photo-catalyst would provide the benefits of higher surface area combined with superior light penetration because the macroporous channels could serve as light-transfer paths for the distribution of photon energy onto the large surface of inner photo-active mesoporous frameworks. As a result, the light utilisation efficiency of heterogeneous photo-catalytic systems, such as photo-oxidation reactors or solar cells,

could be enhanced. In addition, the hierarchical structure-in-structure arrangement of mesopore and macropore is important in molecule traffic control and in the resistance of the photo-catalyst to poisoning by inert deposits. Such structure not only provides a readily accessible pore-wall system but also optimises the transport of matter.

A number of different strategies have been employed to synthesis mesoporous titania. The most popular method is based upon a sol-gel liquid crystal templating technique as pioneered by mobil and co-workers[14, 15]. This approach has also been combined with colloidal crystal templating[4] to incorporate macroporous structures into the mesoporous materials and hence synthesising bimodal meso-macro titania materials. Whilst this article stated that bimodal titania could be synthesised via the route outlined in the article no proof of a successful preparation was offered. This technique was also complex involving a large number of steps to produce the final material.

Bimodal titania has also been prepared without the use of a macrotemplate[16]. The technique involved hydrolysing a titanium alkoxide in the presence of a single surfactant and resulted in materials consisting of a network of disordered rod-like macroporous channels which had wormhole type mesoporosity.

For many applications however, it is desirable to have a material in which both the meso and macro pore regimes are well ordered. The ability to tailor the pore size and morphology is also desirable as it would make it possible to tune the materials effectiveness and properties for a particular application. Finally, a strategy that is straightforward is desirable for any commercial application.

In the following section a simple dip infiltration dual templating method is used to synthesise hierarchically ordered meso/macro titania. Both F127 and Brij 56 are investigated as potential structure directing agents for the mesophase whilst colloidal crystals are used to impart the macropore structure.

a. Meso/macro Titania prepared using F127

Introduction

In the initial attempts to synthesise meso-macro titania, F127 was used as the structure directing agent for the mesophase whilst a colloidal crystal template was used as the template for the macrophase. The methodology involved prefabricating a colloidal crystal template, comprising monodisperse 346 nm PMMA spheres, onto a glass slide prior to dip coating into a reaction mixture containing ethanol, acid, water, $TiCl_4$ and surfactant.

F127 was considered an appropriate choice of surfactant for this application for a number of reasons. Firstly, there are numerous reports in the literature in which F127 has been used to produce mesoporous titania[17, 18]. Secondly, F127 has very simple phase behaviour with a large range of compositions and temperature at which the cubic micellar phase is formed (For reference the binary phase diagram of F127 is shown in chapter 4, page 139.). Finally, F127 is a large surfactant that leads to structures with relatively large pores and thick pore walls. As such, structures templated around these larger surfactants should be more robust than those formed from smaller surfactant species.

Three samples were using reaction mixtures with different compositions. The specific composition of each reaction mixture is shown in table 5.1.

Sample ref	EtOH/g	H_2O/g	$TiCl_4$/g	F127/g
TiC-F127a	18.43	1.8	1.93	0.67
TiC-F127b	18.43	1.8	0.8	1.2
TiC-F127c	18.43	1.8	1.93	1.2

Table 5.1: Table summarising the composition of the reaction mixtures used to synthesise meso macro titania from F127.

Mesostructure

All three samples were observed in a TEM and typical micrographs are shown below in figure 5.1.

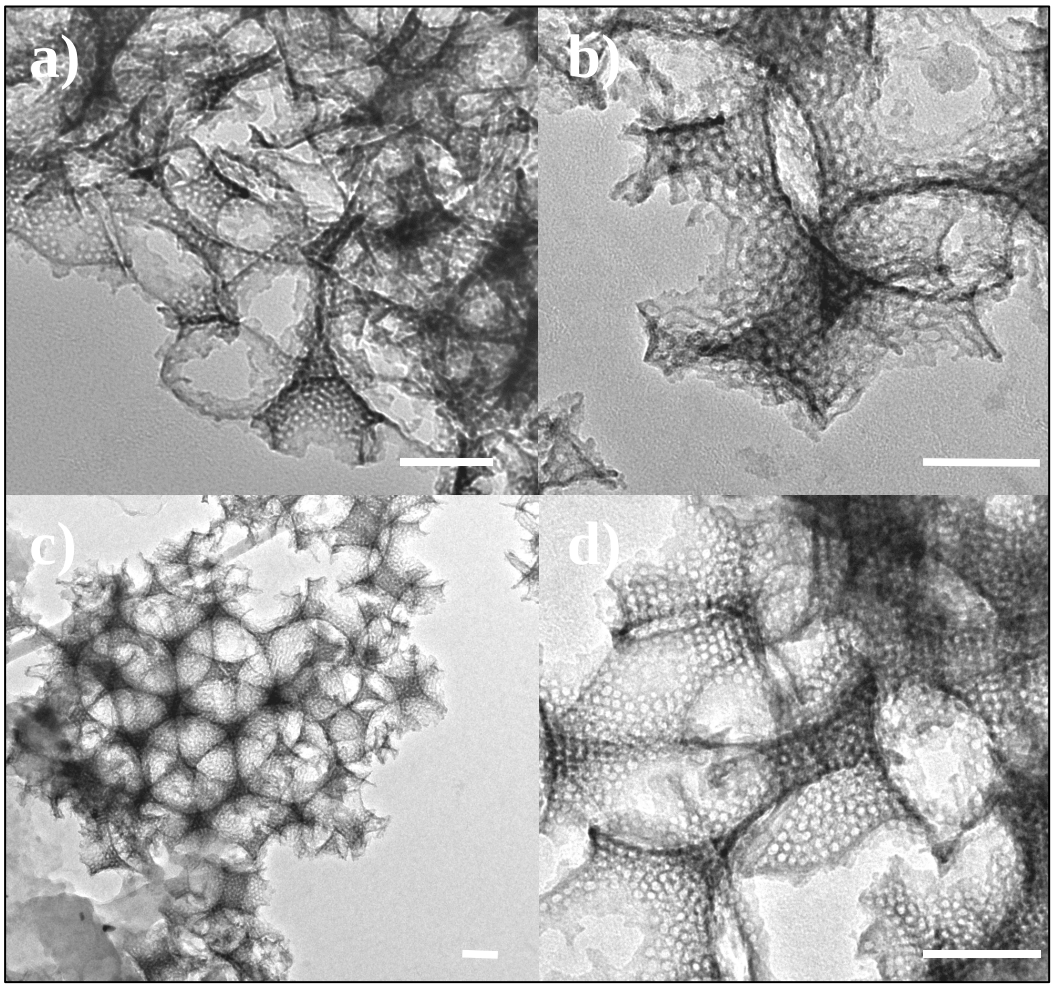

Figure 5.1: TEM images of a meso/macro titania material fabricated from a sol containing 18.43 g EtOH, 1.8g H_2O and (a) 1.93 g $TiCl_4$, 0.67 g F127, (b & c) 0.8 g TiCl4, 1.2 g F127 and (d) 1.93 g $TiCl_4$, 1.2 g F127. Samples were fabricated from a colloidal crystal template comprising 346 nm PMMA spheres. Scale bars represent 100 nm.

In all three samples both the macro and mesoporous structure can be clearly identified in the TEM images. Furthermore, the uniformity of the pore structure on both the meso and macroscale is clearly evident. This represents a significant improvement on previously reported synthetic strategies which have failed to generate ordered pore structures on either length scale.

The three preparations also allow two direct comparisons to be made regarding the effect alterations to the sol's composition has on the final material. Firstly, sample C was fabricated from a reaction mixture with twice the amount of surfactant to sample A. This change in composition resulted in a marked difference to the resultant mesostructure of the two samples. Sample A had several regions which had no meso-porosity whilst sample C had homogenously mesoporous pore walls throughout the sample. This observation is likely a result of insufficient surfactant in the reaction mixture.

Secondly, comparing samples B to sample C shows the effect of a two-fold increase in the quantity of $TiCl_4$ in the reaction mixture. This however made no clear difference to the samples mesostructure.

These two observations indicate that whilst the concentration of surfactant is of critical importance to the final material, the concentration of $TiCl_4$ has a less marked effect. These observations are tenuous however as only a small portion of compositional phase space has been examined making it difficult to distinguish any distinct trends.

Pore sizes

The mesopore size and wall thickness was measured from several TEM images and the averages are presented below in Table 5.2:

Sample ref	Mesopore size/nm	Wall thickness/nm
5.1a	5.46 ± 0.44	3.75 ± 0.76
5.1b	7.55 ± 0.64	3.99 ± 0.95
5.1c	6.77 ± 0.60	3.42 ± 0.87

Table 5.2: Table summarising the average mesopore size and wall thickness for meso/macro titania samples prepared from F127, $TiCl_4$, EtOH and H_2O.

The mesopore wall thickness was consistent for all three samples with an average of 3.72 ± 0.86 nm. Within the experimental errors this is in line with the wall thickness of the meso/macro silica analogues which was measured at 4.57 ± 0.76.

The samples showed considerable variation in mesopore size however and it was notable using a lower quantity of F127 appeared to result in a material with smaller pores. This could be due to the partial collapse of some of the mesopores.

The average mesopore size of samples 2 and 3 was 7.2 ± 0.62 nm, which is consistent with previously reported values for mesoporous titania and is again, within experimental errors, is in line with those evaluated earlier for the meso/macro silica analogues (7.1 ± 1.2 nm).

Macrostructure

All three samples were also analysed using a SEM. All three samples had similar macrostructures as typified by the image shown in figure 5.2. This indicates that small variations in the composition of the reaction mixture do not have a detrimental effect on the resultant macrostructure.

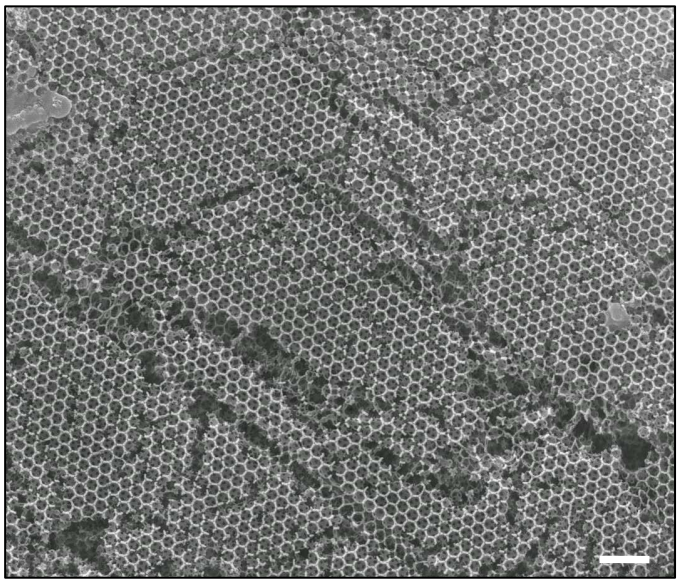

Figure 5.2: SEM image of a meso/macro titania material fabricated from a sol containing 18.43 g EtOH, 1.8g H_2O and 1.93 g $TiCl_4$, 1.2 g F127. Sample was fabricated from a colloidal crystal template comprising 346 nm PMMA spheres. Scale bar represents 1 μm.

Although the samples were all well ordered the titania materials did encompass a greater number of dislocations and tears than the meso/macro silica analogues described in Chapter 4. As already stated the main cause of these defects is thermal shock and shrinkage during calcination which results in the materials tearing to accommodate the reduction in volume.

The average macropore size was also measured from a number of SEM images. The average measured value was 248.2 ± 7.9 nm representing a volume shrinkage of 63 %. This is far in excess of what was observed for the silica analogues (46.5 %) and indicates that the titania analogues are prone to a greater degree of shrinkage upon template removal. This large volume shrinkage accounts for the large number of tears encompassed in the macropore structure.

Surface area analysis

One of the meso/macro titania samples (Sample TiC-F127c) was also analysed by nitrogen adsorption to allow the accurate determination of both the BET surface area and the total pore volume of the material.

For comparison, both a mesoporous and a macroporous titania sample were also synthesised using analogous techniques. Whilst the meso/macro sample was fabricated by dipping a colloidal crystal; into a sol containing surfactant, ethanol, $TiCl_4$ and water, the mesoporous titania was fabricated by dipping a cleaned slide into the same reaction mixture. Finally, the macroporous titania sample was fabricated by dipping a colloidal crystal template into a reaction mixture containing ethanol, $TiCl_4$ and water.

The preparations are summarised below in Table 5.3.

Nanoporosity	Colloidal crystal	F127 /g	H_2O /g	Ethanol /g	$TiCl_4$ /g
Mesoporous	No	12	18	180	19.3
Macroporous	Yes	0	18	180	19.3
Meso/macro	Yes	12	18	180	19.3

Table 5.3: Table summarising the composition of the reaction mixtures used to synthesise meso macro titania from F127.

The BET surface area and total pore volume was recorded for all three samples and these values are presented below in table 5.4.

Sample	Surface area m^2/g	Pore volume cm^3/g
Mesoporous	87.0	0.16
Macroporous	36.8	0.15
Meso/macro	84.3	0.17

Table 5.4: The pore volume and surface area of titania samples with varying levels of porosity.

Both the mesoporous and meso/macroporous samples had a surface area of around 85 $m^2\ g^{-1}$ which is on the lower end of the reported surface areas for mesoporous titania samples. The lower surface area suggests the mesoporosity is either not homogenous or not well interconnected and indicates that the sol-gel reaction mixture is not at the optimum composition for producing high quality mesoporous materials. Furthermore, the fact that both the mesoporous and the meso-macroporous films are of the same order indicates the presence of the macrostructure has no negative effect on the formation of the mesostructure.

As expected the macroporous sample had a considerably lower surface area than the two mesoporous samples highlighting the potential benefit of incorporating a mesoporous sub-structure into a macroporous framework.

b. Meso/macro Titania prepared using Brij 56

Introduction

As with the silica analogues it was hoped that incorporating different surfactants into the reaction mixture would enable access to a wide range of mesopore sizes and morphologies. As such, Brij 56 was substituted into the reaction mixture as the structure-directing agent.

The preparation was analogous to that described in the previous section to synthesis meso/macro silica and again three fabrications were undertaken. In all cases the concentration of $TiCl_4$, ethanol, and water remained constant whilst the concentration of surfactant was incrementally increased.

The composition of the sol-gel reaction mixture of each reaction mixture is shown below in Table 5.5.

Sample ref	EtOH/g	H_2O/g	$TiCl_4$/g	Brij 56/g
TiC-56a	12	2	2	0.7
TiC-56b	12	2	2	1.4
TiC56-c	12	2	2	2.1

Table 5.5: Table summarising the composition of the reaction mixtures used to synthesise meso/macro titania from Brij 56.

Mesostructure

Each sample was first observed in a TEM and a typical micrograph from each sample is shown below in Figure 5.3.

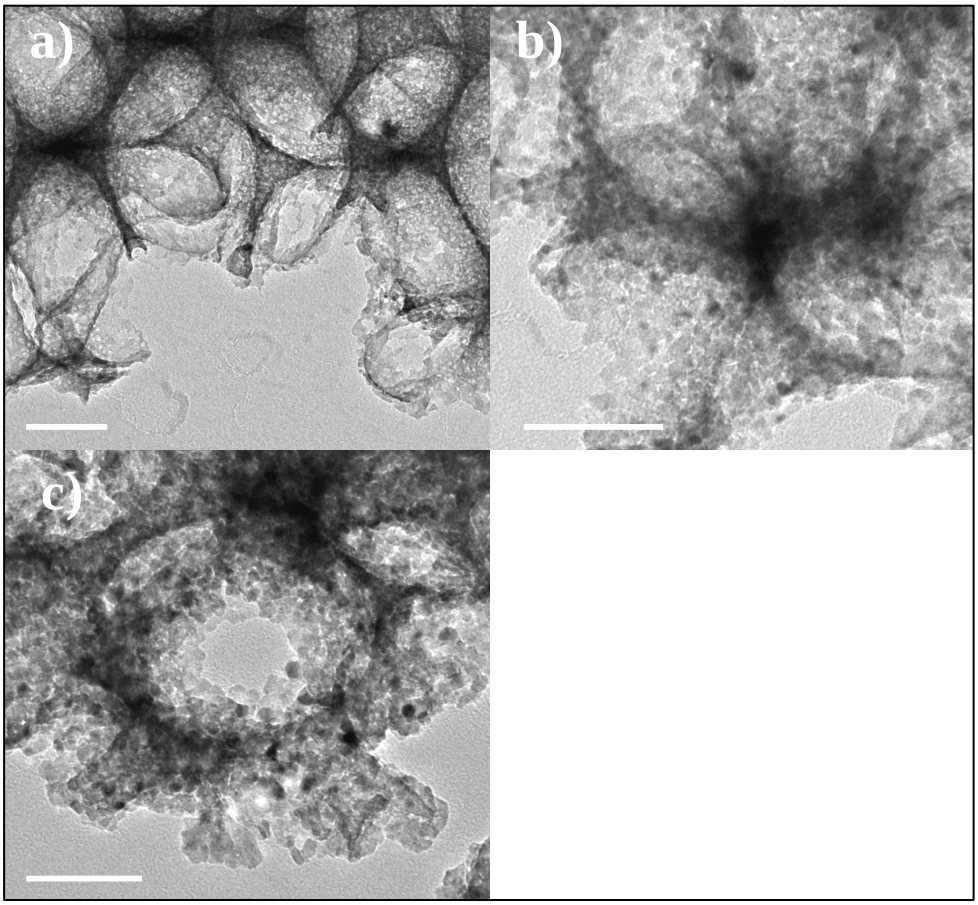

Figure 5.3: A series of TEM images of titania materials fabricated by dip coating a colloidal crystal template in a sol containing 2 g $TiCl_4$, 2 g H_2O, 12 g EtOH and (a) – 0.7 g Brij 56 (TiC-56a), (b) – 1.4 g Brij 56 (TiC-56b) and (c) – 2.1 g Brij 56 (TiC-56c). Materials were templated around a colloidal crystal comprising 346 nm PMMA spheres. Scale bars represents 100 nm.

All three samples were very similar in terms of both their meso and macro structure. In all cases the macrostructure was apparent in the TEM micrograph's, whilst there was no homogenous mesoporosity. It was observed that sample TiC-56a, which was fabricated from a solution containing the least amount of surfactant, had a few very small regions with a wormhole type mesoporosity whilst no mesoporous regions were observed in the other two samples.

It was notable however that the macropore walls encompassed a mesoscale texture. This texture could be caused by mesopore collapse upon calcination due to the thermal instability and subsequent poor mechanical strength of the titania materials. This meso texturing was not observed for the materials synthesised using F127 and assuming the texture arises from mesopore collapse this result can be explained in terms of the decrease in the mesopore wall thickness that would arise from using Brij 56 as the template. Typically mesopore walls from a fabrication using Brij 56 as the structure directing agent are about half the thickness of those formed when F127 is used. This decrease in wall thickness would make the mesostructure more prone to collapse, lacking the mechanical strength required to withstand the thermal treatment during template removal.

4.3.3 Hierarchically ordered meso/macro Zirconia

Preparative methods for nanoporous zirconia have also received attention due to increasing interest in its use in the field of catalysis, and applications such as catalytic supports, chemical sensors, structural ceramics and adsorbents[10, 19-21]

As already discussed many of these applications would benefit from a hierarchically ordered bimodal meso-macroporous structure. However successful preparative methods for such a nanoporous zirconia material are limited.

Su et al detailed a one-pot synthesis of hierarchically ordered zirconia using a single surfactant templating method[5, 24]. These materials encompass parallel arrays of macropores with the macroporous framework encompassing mesopores in a disordered wormhole array. Maekawa et al[25] reported a successful route to meso macro zirconia which combined a moulded polystyrene foam to form the macroporous scaffold with a

block copolymer to form the mesopores. This structure had mesoporous pore walls within a highly disordered macroporous framework.

The following work extends the dual templating technique developed during this thesis to the formation of hierarchically ordered meso-macro zirconia materials. Representing the first successful dual templating route to hierarchically ordered meso-macro zirconia.

Introduction

Hierarchically ordered meso/macro zirconia was prepared using a dual templating method directly analogous to the successful synthetic pathway used to fabricate meso/macro titania.

F127 was used as the structure-directing agent for the mesophase whilst a colloidal crystal template comprising 346 nm PMMA spheres was used for the macrophase. The composition of the reaction mixture into which the colloidal crystal template was dipped was also maintained in line with that used for the titania sample however $ZrCl_4$ was substituted in place of $TiCl_4$ as the metal precursor.

Two different reaction mixtures were tried differing only in the quantity of $ZrCl_4$ that was incorporated into the initial solution. The composition of these two reaction mixtures is shown below in Table 5.6.

Sample ref	EtOH/g	H_2O/g	$ZrCl_4$/g	F127/g
TiC-Zr1	12	1.8	2	0.67
TiC-Zr2	12	1.8	2	1.2

Table 5.6: Table summarising the composition of the reaction mixtures used to synthesise meso macro zirconia from F127.

Mesostructure

Both the samples were observed in a TEM and a typical micrograph of each sample is presented below in figure 5.4.

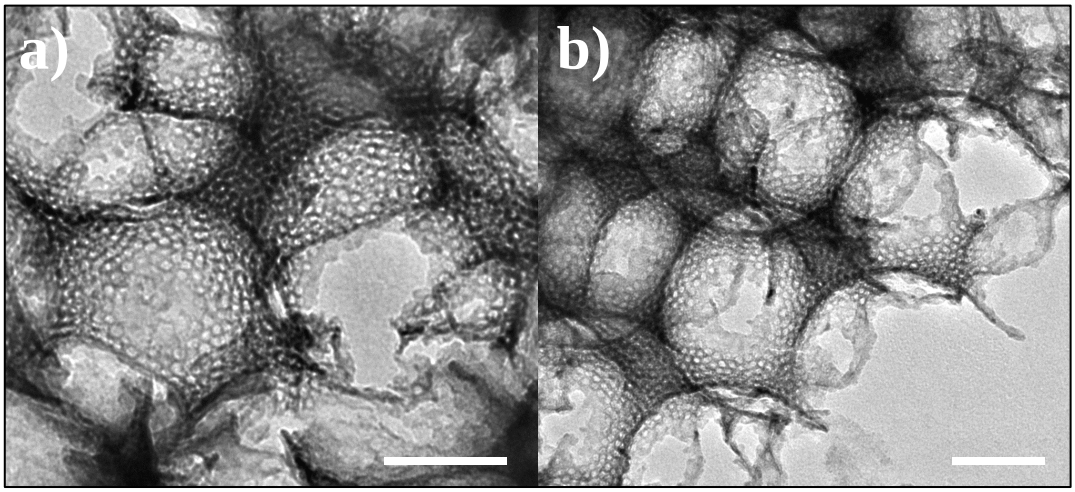

Figure 5.4: TEM images of meso/macro zirconia materials fabricated from a sol containing 2 g $ZrCl_4$, 1.8 g H_2O, 12 g EtOH and (a) – 0.67 g F127 (TiC-Zr1), (b) – 1.2 g F127 (TiC-Zr2). Scale bar represents 100 nm.

Both samples have very clear and well defined homogenous mesoporous sub-structures throughout the entire sample. Furthermore, there was no apparent difference between the two preparative methods again indicating that the concentration of the initial metal precursor has little effect on the final mesostructure. Once again the macroporous framework can be clearly seen in the TEM prepared sample. To the best of our knowledge this fabrication represents the first successful synthesis of a hierarchically ordered meso/macro zirconia material.

Both the size of the mesopores the wall thickness were measured directly from the TEM images and the average values are summarised below in table 5.7.

Sample ref	Mesopore size/nm	Wall thickness/nm
5.2a	6.36 ± 0.78	3.20 ± 0.88
5.2b	7.57 ± 0.80	3.52 ± 0.88

Table 5.7: Table summarising the average mesopore size and wall thickness for meso/macro zirconia samples prepared from F127, $ZrCl_4$, EtOH and H_2O.

Within the experimental errors associated with the image analysis the mesopore size and wall thickness are consistent between the two samples. The average mesopore size is 7.0 ± 0.79 which is consistent with previously reported results for mesoporous materials that were fabricated by templating around F127 aggregates. This value is also consitent with the values reported previously for the titania and silica analogues.

Macrostructure

The macrostructure of the both the materials was also characterised using a SEM and some typical images of both the samples are shown below in Figure 5.5:

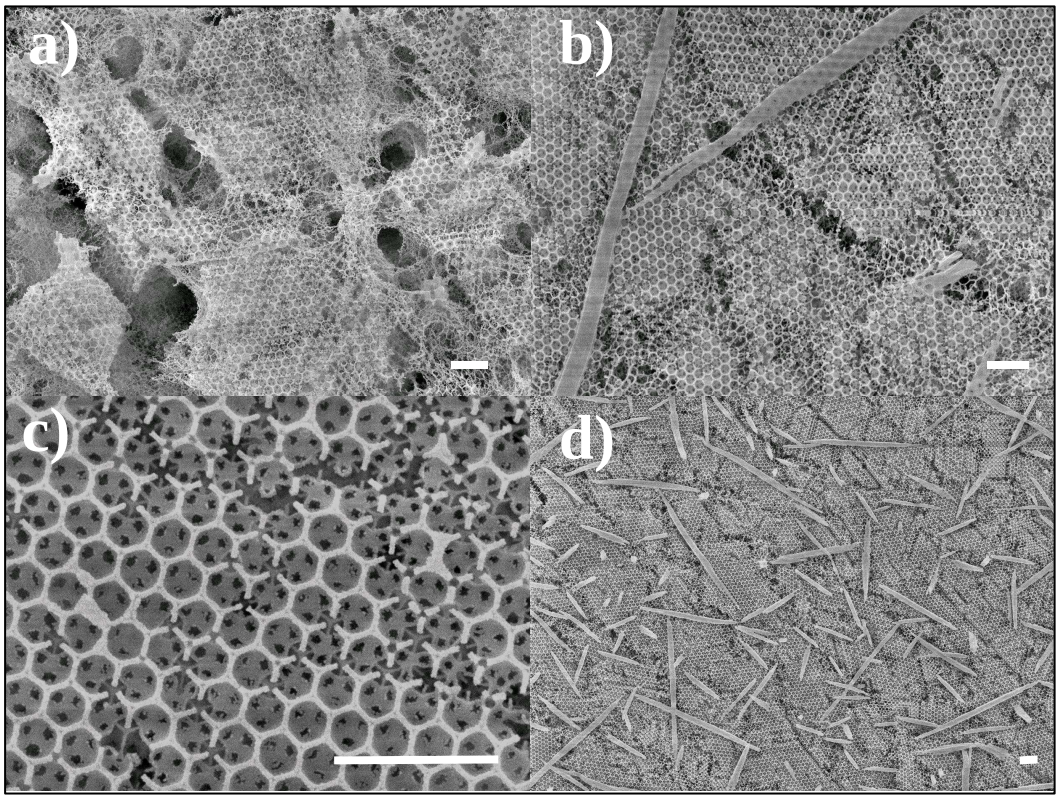

Figure 5.5: SEM images of meso/macro zirconia materials fabricated from a sol containing 2 g $ZrCl_4$, 1.8 g H_2O, 12 g EtOH and (a & b) – 0.67 g F127, (c & d) – 1.2 g F127. Scale bars represents 1 μm.

In both cases the macroporous structure of the original colloidal crystal was reflected in the final material. The number of defects present in the macroporous structure was again greater than that seen for the silica analogues. The level of macropore degradation is well highlighted by Figure 5.5a, which shows some very severe rents and tears over the sample's surface. There were also a number of dislocations present in the top layer of the macroporous material as highlighted in figure 5.5c.

Another interesting feature of the zirconia analogues was the presence of large rod like structures on the surface of the samples. These structures were up to 10 microns in length and about 1 micron wide and are most likely tetragonal zirconia that has crystallised out during the synthesis.

Both the macropore centre to centre distance and wall thickness' were measured directly from the SEM images allowing the calculation of the volume shrinkage and this data is a summarised in table 5.8 below.

Sample ref	Macropore centre to centre/nm	Volume shrinkage/%	Wall thickness/nm
5.2a	252.4 ± 11.6	61	46.2 ± 9.2
5.2b	256.7 ± 9.4	59	41.9 ± 6.8

Table 5.8: Table summarising the average macropore size and wall thickness for meso/macro zirconia samples prepared from F127, $ZrCl_4$, EtOH and H_2O.

Both samples had consistent macropore periodicity and wall thickness. The average macropore centre to centre distance was 254.6 ± 10.5 nm, which corresponds to a volume shrinkage of 60 %. This large volume shrinkage is in line with the titania analogues and can again be used to attribute for the greater number of imperfections in the macroporous structure when compared to the silica analogues.

4.3.4 Hierarchically ordered meso/macro Platinum

A great deal of work has been done on preparations of mesoporous platinum[2, 26]. In most cases the preparation centre on using surfactant aggregates as templates. Most commonly using electrochemical deposition to template around the supramolecular template[2, 26, 27]. Mesoporous platinum has also been successfully synthesised by the reduction of hexachloroplatinic acid (HCPA) in the aqueous phase's of a liquid crystal phase[2, 28].

Similarly macroporous platinum has also been commonly prepared by templating around a colloidal crystal template. Again most routes rely on infiltrating the voids of the colloidal crystal with a platinum precursor solution prior followed by the electrochemical reduction to form platinum metal particles around the colloidal crystal template[29, 30].

Macroporous platinum was prepared by immersing a colloidal crystal templating into a solution containing HCPA and water. The sample was then dried prior to passing a stream of hydrogen gas over the sample to reduce the HCPA. Finally the template is removed by calcination to leave well ordered macroporous platinum particles.

More recently a meso/macro platinum film was successfully prepared by Yamauchi and Kuroda[31]. The synthetic method involved fabricating a colloidal crystal template on a gold coated silicon substrate. This colloidal crystal template was then immersed into a mixture containing HCPA, $C_{16}EO_8$, water and ethanol. After preferential evaporation of the ethanol drives the formation of micelles in the voids of the macropore template the HCPA is reduced to platinum via electrochemical means. The technique is similar in many ways to the techniques used throughout this work with the electrochemical approach enabling the tight control over the film thickness however the mesopore structure was not very well defined. Furthermore, this technique greatly limits the quantity of material that can be produced.

In the following section attempts were made to synthesise platinum particles with a hierarchically ordered meso-macro pore structure. The procedure was similar to that adopted by Yamauchi except the colloidal crystal template was dipped into the reaction mixture in an attempt to promote the production of more ordered and predictable

mesostructures. The final reduction of the HCPA to platinum was then achieved by passing a stream of hydrogen over the sample.

Introduction

Attempts to synthesise hierarchically ordered meso-macro platinum followed a preparative method similar to that used previously in the chapter to synthesise meso/macro ZrO_2 and TiO_2. The methodology involved dipping a colloidal crystal template into a solution containing HCPA, F127, H_2O and ethanol. The sample was then left to dry for 24 hours prior to passing a stream of hydrogen over the sample for a further 24 hours.
Here the intent is that initially the solution infiltrates the voids of the colloidal crystal, preferential evaporation of ethanol drives the formation of micelles in the voids of the colloidal crystal. Finally, hydrogen is used to reduce the HCPA resulting in a platinum network around both the micelles and the colloidal crystal. Subsequent calcination then removes the colloidal crystal template.

The exact composition of the dipping mixture is shown below in table 5.9.

Sample ref	EtOH/g	HCPA/g	H_2O/g	F127/g
5.4a	12	2	3	2

Table 5.9: Table summarising the composition of the reaction mixture used to synthesise meso macro platinum from F127.

Mesostructure

The sample was first analysed in a TEM and some selected images are shown below in Figure 5.6.

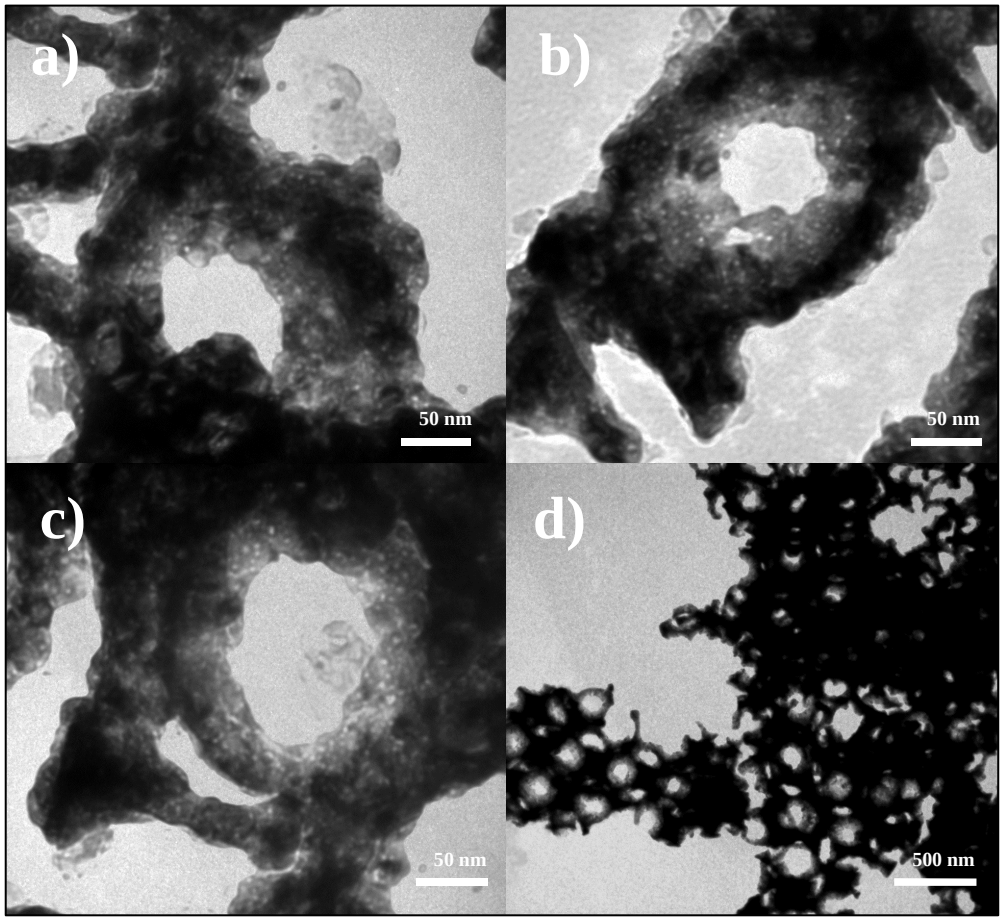

Figure 5.6: A number of TEM images of a crystalline platinum material that was fabricated by dipping a colloidal crystal template into a sol containing 2 g HCPA, 3 g H_2O, 12 g EtOH and 2 g F127. After dipping and drying the sample was passed under a stream of hydrogen for 24 hours. Colloidal crystal template was fabricated from 346 nm PMMA spheres.

The samples did not exhibit a homogenous mesoporous sub-structure as shown by the titania and zirconia samples. However there does appear to be some evidence of mesoporosity in the images, with small light spots visible towards the edges of the material (Figure 5.6a-c). These pores are in the region of 2-3 nm in size, which is much smaller than we would expect from mesopores formed from templating around F127 micelles. Furthermore, they are clearly not arranged in an ordered fashion. It is therefore likely these lighter regions are the result of diffraction occurring to the high-energy electron beam in the TEM. These diffractive effects show that the platinum is crystalline.

It is also worth noting that the material was really rather dense making it very difficult to get any clear information from the TEM micrographs. TEM requires thin samples, which allow the electron beam to transmit through the specimen. In the case of the metal oxide or silica analogues this can easily be achieved by grinding and sonicating the samples to produce small fragments. In the case of the platinum derivative however, this technique simply failed to breakdown the sample, and as such, the subsequent TEM micrographs fail to give us any useful information about the sub-structure.

Macrostructure

The platinum samples were subsequently analysed in a SEM and some images of the sample are shown below in Figure 5.7. Prior to observation in the SEM the sample was cleaved from the glass substrate allowing the direct observation of the sample without the necessity to coat the specimen with a conductive gold layer.

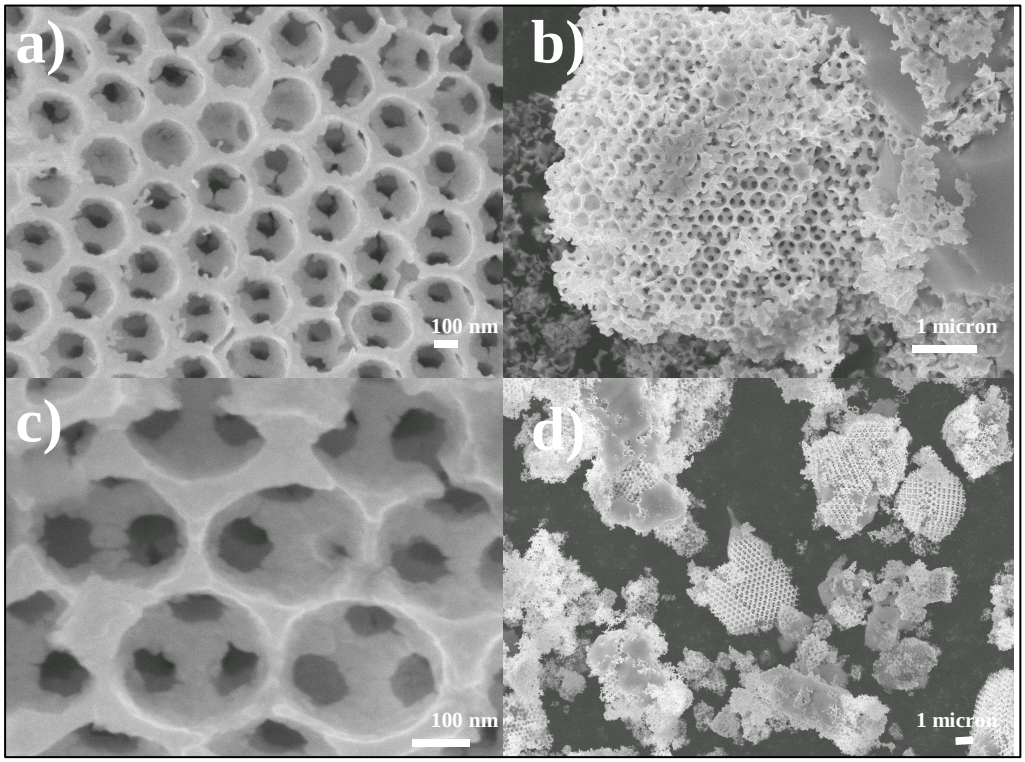

Figure 5.7: A number of SEM images of a crystalline platinum material that was fabricated by dipping a colloidal crystal template into a sol containing 2 g HCPA, 3 g H_2O, 12 g EtOH and 2 g F127. After dipping and drying the sample was passed under a stream of hydrogen for 24 hours. Colloidal crystal template was fabricated from 346 nm PMMA spheres.

The samples clearly have a well-defined macroporous structure showing that the reaction solution has effectively infiltrated the voids of the colloidal crystal template.

The pore sizes were measured from the SEM images and found to be 308.9 ± 13.5 nm representing a volume shrinkage of 28.8 % which occurs as a result of volume shrinkage of HCPA to metal during the hydrogen reduction. The wall size was also measured from the SEM images and found to be 49.1 ± 18.6 nm. Furthermore, the samples do not have spandrels, suggesting that the templating proceeds by the nucleation of small regions of platinum which subsequently grow around the colloidal crystal template.

In summary, whilst this technique has yielded materials with well defined macroporous structures it is unclear as to if there has been a mesoporous substructure incorporated into this framework. The fact that the reduction of the solution occurs in the voids of the colloidal crystal is however encouraging and it is likely that if the correct dipping mixture is used the possibility of fabricating meso-macro platinum by these means could be demonstrated.

4.5 Conclusions

Meso/macro titania and zirconia were both successfully synthesised using a dual templating method. The technique allows the formation of ordered mesopores within an ordered macroporous framework. As yet the technique was limited to a single mesopore size and pore morphology however it is believed this technique could be extended to utilise a whole range of block copolymer surfactants.

Meso macro platinum was synthesised with partial success with a clear macroporous structure the mesoporous structure however could not be confirmed. It does however represent the first reported chemical route to the formation of macroporous platinum.

4.6 References

(1) de Soler-Illia, G. J.; Sanchez, C.; Lebeau, B.; Patarin, J., Chemical Strategies To Design Textured Materials: from Microporous and Mesoporous Oxides to Nanonetworks and Hierarchical Structures. *Chemical Reviews (Washington, DC, United States)* **2002,** 102, (11), 4093-4138.

(2) Attard, G. S.; Bartlett, P. N.; Coleman, N. R. B.; Elliott, J. M.; Owen, J. R.; Wang, J. H., Mesoporous platinum films from lyotropic liquid crystalline phases. *Science (Washington, D. C.)* **1997,** 278, (5339), 838-840.

(3) Huo, Q.; Margolese, D. I.; Ciesla, U.; Feng, P.; Gier, T. E.; Sieger, P.; Leon, R.; Petroff, P. M.; Schueth, F.; Stucky, G. D., Generalized synthesis of periodic surfactant/inorganic composite materials. *Nature (London, United Kingdom)* **1994,** 368, (6469), 317-21.

(4) Yang, P.; Deng, T.; Zhao, D.; Feng, P.; Pine, D.; Chmelka, B. F.; Whitesides, G. M.; Stucky, G. D., Hierarchically ordered oxides. *Science (Washington, D. C.)* **1998,** 282, (5397), 2244-2247.

(5) Yuan, Z.-Y.; Ren, T.-Z.; Vantomme, A.; Su, B.-L., Facile and Generalized Preparation of Hierarchically Mesoporous-Macroporous Binary Metal Oxide Materials. *Chemistry of Materials* **2004,** 16, (24), 5096-5106.

(6) Velev, O. D.; Jede, T. A.; Lobo, R. F.; Lenhoff, A. M., Porous silica via colloidal crystallization. *Nature (London)* **1997,** 389, (6650), 447-448.

(7) Imhof, A.; Pine, D. J., Ordered macroporous materials by emulsion templating. *Nature (London)* **1997,** 389, (6654), 948-951.

(8) Asahi, R.; Taga, Y.; Mannstadt, W.; Freeman, A. J., Electronic and optical properties of anatase TiO2. *Physical Review B: Condensed Matter and Materials Physics* **2000,** 61, (11), 7459-7465.

(9) Mo, S.-D.; Ching, W. Y., Electronic and optical properties of three phases of titanium dioxide: rutile, anatase, and brookite. *Physical Review B: Condensed Matter* **1995,** 51, (19), 13023-32.

(10) Tidahy, H. L.; Siffert, S.; Lamonier, J. F.; Zhilinskaya, E. A.; Aboukais, A.; Yuan, Z. Y.; Vantomme, A.; Su, B. L.; Canet, X.; De Weireld, G.; Frere, M.; N'Guyen, T. B.; Giraudon, J. M.; Leclercq, G., New Pd/hierarchical macro-mesoporous ZrO2, TiO2 and ZrO2-TiO2 catalysts for VOCs total oxidation. *Applied Catalysis, A: General* **2006,** 310, 61-69.

(11) Ho, W.; Yu, J. C.; Lee, S., Synthesis of hierarchical nanoporous F-doped TiO2 spheres with visible light photocatalytic activity. *Chemical Communications (Cambridge, United Kingdom)* **2006**, (10), 1115-1117.

(12) Wang, X.; Yu, J. C.; Ho, C.; Hou, Y.; Fu, X., Photocatalytic Activity of a Hierarchically Macro/Mesoporous Titania. *Langmuir* **2005,** 21, (6), 2552-2559.

(13) Fuertes, M. C.; Soler-Illia, G. J. A. A., Processing of Macroporous Titania Thin Films: From Multiscale Functional Porosity to Nanocrystalline Macroporous TiO2. *Chemistry of Materials* **2006,** 18, (8), 2109-2117.

(14) Kresge, C. T.; Leonowicz, M. E.; Roth, W. J.; Vartuli, J. C.; Beck, J. S., Ordered mesoporous molecular sieves synthesized by a liquid-crystal template mechanism. *Nature (London, United Kingdom)* **1992,** 359, (6397), 710-12.

(15) Beck, J. S.; Vartuli, J. C.; Roth, W. J.; Leonowicz, M. E.; Kresge, C. T.; Schmitt, K. D.; Chu, C. T. W.; Olson, D. H.; Sheppard, E. W.; et al., A new family of mesoporous molecular sieves prepared with liquid crystal templates. *Journal of the American Chemical Society* **1992,** 114, (27), 10834-43.

(16) Blin, J.-L.; Leonard, A.; Yuan, Z.-Y.; Gigot, L.; Vantomme, A.; Cheetham, A. K.; Su, B.-L., Hierarchically mesoporous/macroporous metal oxides templated from polyethylene oxide surfactant assemblies. *Angewandte Chemie, International Edition* **2003,** 42, (25), 2872-2875.

(17) Grosso, D.; Soler-Illia, G. J. d. A. A.; Babonneau, F.; Sanchez, C.; Albouy, P.-A.; Brunet-Bruneau, A.; Balkenende, A. R., Highly organized mesoporous titania thin films showing mono-oriented 2D hexagonal channels. *Advanced Materials (Weinheim, Germany)* **2001,** 13, (14), 1085-1090.

(18) Bosc, F.; Ayral, A.; Albouy, P.-A.; Datas, L.; Guizard, C., Mesostructure of Anatase Thin Films Prepared by Mesophase Templating. *Chemistry of Materials* **2004,** 16, (11), 2208-2214.

(19) Huang, Y.; Sachtler, W. M. H., Mesoporous sulfated zirconia: Preparation and applications as acid catalyst and metal catalyst support. *Book of Abstracts, 214th ACS National Meeting, Las Vegas, NV, September 7-11* **1997**, CATL-025.

(20) Idakiev, V.; Tabakova, T.; Naydenov, A.; Yuan, Z. Y.; Su, B. L., Gold catalysts supported on mesoporous zirconia for low-temperature water-gas shift reaction. *Applied Catalysis, B: Environmental* **2006,** 63, (3-4), 178-186.

(21) Schroden, R. C.; Al-Daous, M.; Sokolov, S.; Melde, B. J.; Lytle, J. C.; Stein, A.; Carbajo, M. C.; Fernandez, J. T.; Rodriguez, E. E., Hybrid macroporous materials for heavy metal ion adsorption. *Journal of Materials Chemistry* **2002,** 12, (11), 3261-3267.

(22) Al-Daous, M. A.; Stein, A., Preparation and Catalytic Evaluation of Macroporous Crystalline Sulfated Zirconium Dioxide Templated with Colloidal Crystals. *Chemistry of Materials* **2003,** 15, (13), 2638-2645.

(23) Chen, H.-r.; Shi, J.-l.; Li, L.; Ruan, M.-l.; Yan, D.-s., A study of novel composite mesoporous zirconia catalyst materials. *Journal of Chemical Engineering of Japan* **2003,** 36, (10), 1212-1215.

(24) Yuan, Z.-Y.; Vantomme, A.; Leonard, A.; Su, B.-L., Surfactant-assisted synthesis of unprecedented hierarchical meso-macrostructured zirconia. *Chemical Communications (Cambridge, United Kingdom)* **2003**, (13), 1558-1559.

(25) Maekawa, H.; Esquena, J.; Bishop, S.; Solans, C.; Chmelka, B. F., Meso/macroporous inorganic oxide monoliths from polymer foams. *Advanced Materials (Weinheim, Germany)* **2003,** 15, (7-8), 591-596.

(26) Attard, G. S.; Coleman, N. R. B.; Elliott, J. M., Preparation of mesoporous metals from preformed surfactant assemblies. *Studies in Surface Science and Catalysis* **1998,** 117, (Mesoporous Molecular Sieves 1998), 89-94.

(27) Elliott, J. M.; Attard, G. S.; Bartlett, P. N.; Coleman, N. R. B.; Merckel, D. A. S.; Owen, J. R., Nanostructured platinum (HI-ePt) films. Effects of electrodeposition conditions on film properties. *Chemistry of Materials* **1999,** 11, (12), 3602-3609.

(28) Attard, G. S.; Leclerc, S. A. A.; Maniguet, S.; Russell, A. E.; Nandhakumar, I.; Bartlett, P. N., Mesoporous Pt/Ru Alloy from the Hexagonal Lyotropic Liquid Crystalline Phase of a Nonionic Surfactant. *Chemistry of Materials* **2001,** 13, (5), 1444-1446.

(29) Bartlett, P. N.; Birkin, P. R.; Ghanem, M. A., Electrochemical deposition of macroporous platinum, palladium and cobalt films using polystyrene latex sphere templates. *Chemical Communications (Cambridge)* **2000**, (17), 1671-1672.

(30) Bartlett, P. N.; Baumberg, J. J.; Birkin, P. R.; Ghanem, M. A.; Netti, M. C., Highly Ordered Macroporous Gold and Platinum Films Formed by Electrochemical Deposition through Templates Assembled from Submicron Diameter Monodisperse Polystyrene Spheres. *Chemistry of Materials* **2002,** 14, (5), 2199-2208.

(31) Yamauchi, Y.; Kuroda, K., Fabrication of a Pt film with a well-defined hierarchical pore system via \"solvent-evaporation-mediated direct physical casting\". *Electrochemistry Communications* **2006,** 8, (10), 1677-1682.

CHAPTER 6 – Conclusions

6.1 3D macroporous metal silicate materials

During the course of this thesis several synthetic strategies have been developed enabling the fabrication of nanoporous oxides with a variety of nanoporous structures, a range of periodicities and varied chemistry.

Initially research focussed on producing macroporous materials using sol-gel chemistry to template around pre formed colloidal crystal templates. As a functional material, silica is of limited interest; however by incorporating a heterometal into the silica framework it is possible to produce materials with more interesting properties.

This is by no means trivial as achieving high heteroatom loadings in silica, in addition to maintaining homogenous materials with atomic scale mixing is a synthetic challenge. The problem arises from the incompatibility between the hydrolysis rates of metal alkoxides to those of silicon. The faster hydrolysing metal alkoxide species favour self condensation instead of reaction with the silicon alkoxide, resulting in precipitation of metal rich compounds. Two strategies can be employed to solve this problem and they are either by complexation of the metal species in order to reduce the active sites for hydrolysis or by prehydrolysis of the silicon alkoxide making heterogenous condensation more likely. Of these two strategies complexation adds another level of complexity to the synthetic strategy and commonly results in films with poor mechanical and thermal stability. The mixed oxide films are often further subject to heterometal leaching at high temperatures. Prior to the work presented here macroporous silica films with high (> 20%) loadings of aluminium, titanium or tin had not been reported.

During the course of the thesis a facile silicon alkoxide prehydrolysis technique that allows the direct formation of highly ordered mixed metal oxide macroporous materials comprising Ti/Si, Al/Si, and Sn/Si. In the case of the titano and aluminsilicates ordered macroporous Al:Si and Ti:Si materials with atomic ratios ranging from 1:10 to 1:2 and 10:1 to 1:1 were successfully fabricated. The sample with a very high heterometal loading represent the highest heterometal loading ever observed in a nanoporous alumino or titano silicate material. The final composition of the material was evidenced by EDX on the final materials and this showed that the M:Si ratio in the final material was in

line with the known M:Si ratio in the initial sol. This proves that no metal leaching or phase separation occurs in the sol-gel mixture prior to templating.

The macroporous structure was directly observed and characterised by scanning electron microscopy and the macroporous structure of both the aluminosilicate and titanosilicate macroporous metal oxides are defect free over large areas (2500 μm^2) with defects limited to approximately 1 per 150 spheres. In all cases the structures were found to shrink by about 20% which is in line with sol-gel processes. The air spheres were primarily arranged in a close packed array reflecting the close packed ordering of the initial colloidal crystal template.

Whilst all the titanosilicate and aluminoslicate materials had well ordered macroporous structures in the case of the tin silicate materials increasing the heterometal loading led to a deterioration of the macroporous structure. This was attributed to phase separation reducing the mechanical stability of the macroporous framework. As such, ordered macroporous tin silicates with high heterometal loading were not successfully synthesised.

Atomic scale mixing of the heterometal into the silica framework is highly desirable as only when the mixing is on the atomic scale will the final material have different physical characteristics. As such, the homogeneity was subsequently verified using MAS-NMR and iR and whilst these techniques can comprehensive conclude that the materials are atomically homogenous they provided compelling evidence pointing towards atomic scale homogeneity. Furthermore, as the heterometal content in the tin silicate materials was increased we observed a structural degradation which was attributed to phase separation. In the vase of the alumino and titano silicates the structure was consistent regardless of the heterometal loading which further support atomic scale homogeneity.

In terms of the Titanosilicate materials an EXAFS study on the as synthesised materials would provide a clearer picture regarding the atomic scale homogeneity as the average titanium coordination state could be elucidated. If the titanium was incorporated into the silica structure we would expect the titanium to be in a coordination state of four. If on the other hand the titanium was separating into titania rich regions the coordination state in this case would be six.

Reflectance spectra was collected on the titanosilicate materials and showed that the macroporous titanosilicate materials showed a steady increase in refractive index as the titanium loading was increased (From 1.2 -1.5, with Ti:Si 1:10 and 1:1 respectively).

This tunability of the refractive index is particular interesting for optical applications and was pertinent in this work as one of the primary motivations for the work was the possibility to use these materials as special effect pigments on account of the bright diffractive effects which are observed in these materials on account of Bragg diffraction. To this end the ability to modulate the refractive index of the materials enables the enhancement the optical properties.

Another interesting area for these materials is catalysis and as such the thermal stability of these materials was also examined by subjecting samples to various extreme temperatures and then characterising the structure by SEM and XRD. It was found that both the titanosilicate and aluminosilicate porous networks were stable to temperature extremes of 900 ^{o}C and 1000 ^{o}C respectively prior to crystalline phase separation and pore collapse. Consequently, the mixed macroporous oxides are ideal for high temperature catalytic applications with large molecular weight compounds.

6.2 Hierarchically ordered meso/macro silica

The second area investigated during the research was the synthesis and characterisation of hierarchical porous materials. This is a very new field of research but has become the focus of many research groups on account of their potential for technological applications. In particular for applications as catalysts or sensors these materials hold considerable promise as they combine the high surface area of mesoporous materials with the large framework structure of macroporous materials, thereby increasing the mass transfer of reactants to the active sites whilst minimising pore blocking.

The work in this thesis reports a simple dual templating dip infiltration method that enables the production of highly ordered well defined macroporous materials with ordered mesoporous pore walls using a number of different surfactants. The final materials have very high surface areas and large pore volumes.

The method involved dipping a colloidal crystal template comprising pmma spheres into a solution which contained EtOH, 0.5M HCl, surfactant and TEOS. Subsequent drying and calcination resulted in a hierarchical nanoporous material with a well defined macroporous structure which further had mesoporous pore walls. Both the mesopore and macropore systems are interconnected and the final materials have well characterised pore systems and high surface areas.

A critical study of the reaction constituents showed that the final mesophase can be altered in terms of both morphology and pore size by judicious selection of surfactant and the subsequent ratio of 0.5M HCl, TEOS and surfactant. It was also shown that the ethanol's role in the synthesis was not structure directing but to produce a free flowing homogenous solution. It is postulated that the mesophase formation occurs in a manner analogous to the evaporation induced self assembly (EISA) mechanism reported by Brinker et al for the production of mesoporous films. The power of this technique is that it enables the direct fabrication of materials with highly ordered mesopore systems and tight pore size distributions. Furthermore, the technique realises the possible to predictably synthesis materials with desired mesopore sizes and morphologies.

Using both Brij 56 and Brij 78 as the surfactant it was shown that a final ternary diagram can be develops which relates the relative concentration of surfactant, TeOS and 0.5M HCl to the final mesophase. As such, the ternary diagram can then be used to predict what mesophase will form in much the same was as a phase diagram would be used for a binary water surfactant system.

It was also subsequently shown that other polymeric surfactants (F127 and P123) and even the ionic surfactant CTAB could be successfully incorporated into the sol-gel solution to synthesise meso macro materials. The choice of surfactant had a critical impact on both the mesopore structure and pore size. By changing the surfactant pore sizes ranging from 1.8 nm up to 7 nm were formed.

Furthermore, the periodicity of the macropores was dependant on the size of the PMMA microspheres. As such this technique makes it possible to synthesise a large range of materials with highly ordered hierarchical meso/macro architectures specifically tailored for any particular application.

The macroporous structure was evident in all the materials and was independent of which surfactant was used in the templating mixture. The macroporous materials typically encompassed a large number of tears and distortions which occurred due to shrinkage of the sol-gel matrix upon drying and calcination.

The samples were also characterised by Nitrogen sorption and were found to have high surface areas (Up to 550 m^{-2} g^{-1}). The Nitrogen sorption isotherm collected from meso-macroporous materials synthesised using F127 exhibited a clear hysteresis loop which evidences the narrow pore size distribution in these materials. The hysteresis loop itself was of type H2 which is evidence that the mesopores are spherical and highly mono-disperse. Further BJH analysis of the desorption branch of the isotherm gave a sharp peak at 6.7 nm again reinforcing the tight mesopore size distribution in this material. Hysteresis loops were not observed when brij or CTAB surfactants were used as the structure directing agent and this is because the resultant mesopores are below the size range that exhibits hysteresis loops.

The study would further be complimented with SAXS data on the as synthesised materials which would give a clearer picture regarding the mesopore structure. In the thesis the mesopore morphology was observed by TEM which only allows one to conclude that the mesopores are ordered or disordered.

Despite this it is clear that this technique represents a huge advancement in terms of preparative methods for meso-macro materials, detailing an extremely simple technique which is also highly versatile. The primary benefit in terms of the silica materials was the ability to tailor the mesopore size via the incorporation of various surfactants into the reaction mixture and still obtain a mesoporous substructure within a well order macroporous framework.

6.3 Hierarchically ordered meso/macro non-silica materials

The natural progression of the work on meso-macro silica materials was to take these principles and techniques and apply them to the synthesis of non silica materials. Meso-macro silica has limited potential for both catalytic or sensor applications so the preparation of non silica meso-macro materials represents a significant advancement.

Initial attempts to synthesise both meso/macro titania and zirconia using dual templating methods analogous to those developed for meso-macro silica were successful. In this case the dipping solution contained MCl_4 (Where M = Zr or Ti), EtOH, F127 and 0.5 M HCl). Once again a preformed colloidal crystal template was used to form the macrostructure whilst a surfactant was used to form the meso structure. The resultant materials all had well defined macroporous structures with mesoporous pore walls. The mesopores were measured at around 7 nm.

The synthesis of meso-macro titania and zirconia increases the diversity of materials that can be synthesised using this simple dual templating method and further highlights the versatility of the technique developed throughout this work. It is also postulated that this technique could be extended further to incorporate a wide array of mesopore morphologies and a vast array of chemistries by using different precursors.

The synthesis of Titania was not as versatile as the synthesis of silica however as attempts to synthesise meso-macro titania using Brij 56 as the surfactant were unsuccessful. The macropore walls did have a mesoporous texture which was attributed to mesopore wall collapse upon template removal. The Brij 56 surfactant would yield a mesoporous structure with thinner pore walls than the F127 surfactant which would result the mesostructure having less mechanical stability.

Finally, the synthetic strategies used throughout this thesis were adapted and applied to the production of meso-macro platinum. In this case a solution containing surfactant, Hexachloro-platinic acid, EtOH and 0.5 M HCl was used as a dipping solution for a colloidal crystal template. This was then placed under a hydrogen atmosphere for two weeks to reduce the HCPA to platinum before calcination removed the microspheres. In this case the materials were examined using both SEM and TEM.

The sample had well defined macroporous structures from templating around the colloidal crystal. Further to this the appearance of a small number of mesopores were observed on the TEM micrographs. On account of the density of the platinum samples the evidence for mesoporosity was not conclusive and these light spots could also be attributed to diffraction of the electron beam. The macroporosity was clearly evidenced and this preparative method does represent one of the only reports of macroporous platinum fabricated via wet chemical routes.

In summary, the work completed during the course of this thesis represents significant advancements in the field of nanoporous materials. Initially techniques to increase the heterometal loading of titania and aluminium in macroporous metal silicate materials were developed which make it possible to achieve higher heterometal loadings than have previously been reported (Ti:Si, Al:Si of 1:1 and 1:2 respectively). Secondly, synthetic strategies to fabricate meso-macro silica, titania and zirconia were developed. These strategies were shown to produce well order meso-macro materials which could be tuned by altering the chemical structure of the surfactant and the ratio of the initial sol gel constituents. The work represents the simplest and most versatile route to the fabrication of meso-macro materials currently reported.